VTT PUBLICATIONS 390

Prediction of microsegregation and pitting corrosion resistance of austenitic stainless steel welds by modelling

Martti Vilpas

VTT Manufacturing Technology

Dissertation for the degree of Doctor of Science in Technology to be presented with due permission for public examination and debate in Auditorium K216 at Helsinki University of Technology (Espoo, Finland) on the 22th of June, 1999 at 12 o'clock noon.

TECHNICAL RESEARCH CENTRE OF FINLAND
ESPOO 1999

ISBN 951–38–5383–7 (soft back ed.)
ISSN 1235–0621 (soft back ed.)

951–38–5384–5 (URL: http://www.inf.vtt.fi/pdf/)
1455–0849 (URL: http://www.inf.vtt.fi/pdf/)

JULKAISIJA – UTGIVARE – PUBLISHER

Valtion teknillinen tutkimuskeskus (VTT), Vuorimiehentie 5, PL 2000, 02044 VTT
puh. vaihde (09) 4561, faksi (09) 456 4374

Statens tekniska forskningscentral (VTT), Bergsmansvägen 5, PB 2000, 02044 VTT
tel. växel (09) 4561, fax (09) 456 4374

Technical Research Centre of Finland (VTT), Vuorimiehentie 5, P.O.Box 2000, FIN–02044 VTT, Finland
phone international + 358 9 4561, fax + 358 9 456 4374

VTT Valmistustekniikka, Voimalaitosten materiaalitekniikka,
Kemistintie 3, PL 1704, 02044 VTT
puh. vaihde (09) 4561, faksi (09) 456 7002

VTT Tillverkningsteknik, Material och strukturell integritet,
Kemistvägen 3, PB 1704, 02044 VTT
tel. växel (09) 4561, fax (09) 456 7002

VTT Manufacturing Technology, Materials and Structural Integrity,
Kemistintie 3, P.O.Box 1704, FIN–02044 VTT, Finland
phone international + 358 9 4561, fax + 358 9 456 7002

Technical editing Maini Manninen

Libella Painopalvelu Oy, Espoo 1999

Vilpas, Martti, Prediction of microsegregation and pitting corrosion resistance of austenitic stainless steel welds by modelling. Espoo 1999. Technical Research Centre of Finland, VTT Publications 390. 139 p. + app. 27 p.

Keywords austenitic stainless steel, welding, surface remelting, solidification, microsegregation, corrosion resistance, modelling, prediction, pitting corrosion

Abstract

The present study focuses on the ability of several computer models to accurately predict the solidification, microsegregation and pitting corrosion resistance of austenitic stainless steel weld metals. Emphasis was given to modelling the effect of welding speed on solute redistribution and ultimately to the prediction of weld pitting corrosion resistance. Calculations were experimentally verified by applying autogenous GTA- and laser processes over the welding speed range of 0.1 to 5 m/min for several austenitic stainless steel grades.

Analytical and computer aided models were applied and linked together for modelling the solidification behaviour of welds. The combined use of macroscopic and microscopic modelling is a unique feature of this work. This procedure made it possible to demonstrate the effect of weld pool shape and the resulting solidification parameters on microsegregation and pitting corrosion resistance. Microscopic models were also used separately to study the role of welding speed and solidification mode in the development of microsegregation and pitting corrosion resistance.

These investigations demonstrate that the macroscopic model can be implemented to predict solidification parameters that agree well with experimentally measured values. The linked macro-micro modelling was also able to accurately predict segregation profiles and CPT-temperatures obtained from experiments. The macro-micro simulations clearly showed the major roles of weld composition and welding speed in determining segregation and pitting corrosion resistance while the effect of weld shape variations remained negligible.

The microscopic dendrite tip and interdendritic models were applied to welds with good agreement with measured segregation profiles. Simulations predicted that weld inhomogeneity can be substantially decreased with increasing welding speed resulting in a corresponding improvement in the weld pitting corrosion resistance. In the case of primary austenitic solidification, the dendrite cores were predicted to be the weakest link with respect to weld pitting corrosion resistance. In primary ferritic solidification, the second phase austenite in the vicinity of δ/γ interfaces was predicted to show lowest pitting corrosion resistance.

Solidification parameters used in the modelling were verified by cooling rate and dendrite arm spacing measurements as well as by analytical calculations. Experimental investigations using electron probe microanalyses (EPMA, CMA), electron microscopy (SEM, FEG-STEM), microstructural investigations and pitting corrosion tests were used in assessing the calculated microsegregation and CPT-temperatures and showed a reasonably good compatibility with the results of modelling.

Preface

The majority of the work presented in this thesis was accomplished at VTT Manufacturing Technology as a part of a research project “Optimisation of weld properties by solidification modelling” during the years 1995 - 1997. The project was financed by the Technology Development Center of Finland (Tekes), Outokumpu Polarit Oy, Ahlstrom Machinery Oy and VTT Manufacturing Technology. A part of the study was implemented during a technical visit to Japan that was contributed by Japan-Scandinavia Sasakawa Foundation and VTT. I would like to thank all these parties for their economical and technical support.

Professor Hannu Hänninen at Helsinki University of Technology and Professor Risto Karppi at VTT Manufacturing Technology, the supervisor and instructor of this thesis, respectively, deserve my sincere gratitude for their valuable discussions, good advise and encouragement.

I would like to express my sincere thanks also to the pre-examiners of this thesis, Professor Veli Kujanpää at Lappeenranta University of Technology and General Manager Niilo Suutala at Outokumpu Polarit Oy for their constructive criticism and valuable comments.

I am deeply indebted to Research Director Heikki Kleemola, Research Manager Rauno Rintamaa and Group Manager Heli Talja at VTT Manufacturing Technology for providing me opportunities and resources that were needed to make this effort possible.

Professor Kazutoshi Nishimoto at Osaka University deserves my special thanks for his technical advises and for the possibility to implement a part of the study as a visiting researcher at Osaka University in spring and summer 1997. During the technical visit to Japan a part of the modelling work and experiments were implemented also at Nippon Steel Co. For this possibility and fruitful co-operation I would like to express my sincere thanks to Dr. Nobutaka Yurioka, Dr. Masao Fuji, Dr. Toshihiko Koseki and Dr. Hiroshige Inoue.

The macroscopic simulations were carried out by means of a computerised model developed by Pennsylvania State University. For the possibility to use the model, I am thankful to professor Tarasankar DebRoy. Concerning technical support in modelling, I am very much indebted to my colleague Mr. Hannu Martikainen from VTT Manufacturing Technology. I am also very grateful to Dr. Jyrki Miettinen at Helsinki University of Technology for collaboration in part of microscopic modelling.

The experimental investigations including delivery of test materials, pitting corrosion tests, and part of the metallography were conducted in close collaboration with Mr. Antero Kyröläinen and his co-workers at Outokumpu

Polarit Oy to whom I express my special thanks. Concerning line scan analyses and part of the microscopy of the test welds I would like to thank also Mr. Olli Nousiainen at University of Oulu. Mr. Tapio Saukkonen at Helsinki University of Technology is acknowledged for his contribution in a part of scanning electron microscopy studies. Concerning the nitrogen analyses I am grateful to Mrs. Connie Westman from the Swedish Institute of Metals Research in Stockholm.

The experiments at VTT Manufacturing Technology were carried out jointly with Mr. Esko Kallinen (welding), Mr. Jouni Alhainen (weld cooling measurements), Mrs. Anja Norring (metallography) and Mr. Pertti Nenonen (electron microscopy) to whom I am very grateful for fruitful collaboration. I would like to thank also Mrs. Åsa Åvall for help in editing of the manuscript and Mr. Tuomo Hokkanen for preparing the drawings. Dr. Gary Marquis deserves sincere thanks for revising the English text. To these and all other colleagues working for this effort I would like to express my most sincere gratitude.

Finally, I would like to express my warmest thanks to my family, dear wife Pirjo, and two sons Mika and Juha for love, patience, encouragement and understanding which were all needed to finalise this effort.

Contents

List of symbols and acronyms

Latin alphabet

a_o	interatomic distance
c	specific heat
d_1	dendrite primary arm spacing
d_2	dendrite secondary arm spacing
$d\gamma/dT$	temperature gradient of surface tension
f_{bm}	volume fraction of base metal
f_{weld}	volume fraction of weld metal
f_s	fraction of solidified metal
k	equilibrium partition coefficient
k’	velocity dependent partition coefficient
m	slope of liquidus line
r_t	dendrite tip radius
t_f	local solidification time
$t_{12/8}$	cooling time between 1200°C and 800°C
v	welding speed
v_{max}	maximum flow rate
A	fully austenitic solidification
F	fully ferritic solidification
C_o	initial composition
C_L	pile-up composition
C_S	dendrite tip composition
C_{CORE}	dendrite core composition
C_{ID}	interdendritic composition
C(local/av)	ratio of local and average composition
C(min/av)	ratio of minimum and average composition
C(max/av)	ratio of maximum and average composition
D	diffusion coefficient
D_L	diffusion coefficient of solute in liquid state
D_S	diffusion coefficient of solute in solid state
G	temperature gradient
N_{bm}	nitrogen content of base metal
N_{meas}	measured nitrogen content
N_{weld}	nitrogen content of weld metal
P	partition ratio, Peclet number
Q	heat input
R	solidification rate
R_{hkl}	solidification rate to crystallographic direction < hkl >
S	segregation ratio
T	temperature
T_L	liquidus temperature
T_S	solidus temperature

ΔT	temperature interval between liquidus and solidus, undercooling

Greek alphabet

χ	chi-phase
δ	ferrite
δ_i	solute trapping distance
ϕ	angle between welding direction and grain growth direction
γ	austenite
η	thermal efficiency
λ	thermal conductivity
μ	chemical potential
ρ	density
σ	sigma phase
Γ	Gibbs-Thomson parameter
θ	angle between welding direction and normal to the solidification front
ψ	angle between crystallographic grain growth direction and normal to the solidification front
Ω	back-diffusion parameter
Ω_i	solutal supersaturation of solute i

Special notations

AF	primary austenitic solidification
FA	primary ferritic solidification
CMA	computer aided microprobe analysis
CPT	critical pitting temperature
Cr_{eq}	chromium equivalent
EPMA	electron probe microanalysis
FEG-STEM	scanning-transmission electron microscope equipped with field emission gun
MA	massive austenite
Ni_{eq}	nickel equivalent
Cr_{eq} / Ni_{eq}	ratio of chromium equivalent and nickel equivalent
PRE	pitting resistance equivalent
PRE(local/av)	ratio of local and average PRE
PRE(min/av)	ratio of minimum and average PRE
PRE(max/min)	ratio of maximum and minimum PRE
TIP-ID	combined dendrite tip and interdendritic modelling
ID	interdendritic modelling
Iv(P)	Ivantsov's function for growth of a paraboloid dendrite tip
NSC-model	interdendritic solidificaton model of Nippon Steel Co.

Original features

In this thesis various modelling techniques are applied to link weld solidification behaviour to weld metal properties, especially to pitting corrosion resistance of austenitic stainless steel welds. The main objective was to demonstrate the effect of solidification parameters, i.e., solidification rate, temperature gradient and cooling rate on solute redistribution and the resulting pitting corrosion resistance of the welds studied applying computer aided modelling.

The following features of this thesis are believed to be original:

1) Macroscopic and microscopic modelling is coupled in order to achieve better understanding on the links between weld pool behaviour and solidification parameters, solute redistribution and pitting corrosion resistance of austenitic stainless steel welds. The applicability of the macro-micro model is supported by reasonably good compatibility with experimental measurements of weld penetration shape, solidification parameters, microsegregation and critical pitting corrosion temperature.

2) Dendrite tip and interdendritic models are applied as a function of weld solidification rate to predict critical pitting temperature (CPT) of GTA- and laser welds of primary austenitic welds. Good agreement with calculations and experiments supports the validity of these simulations.

3) The values of solidification parameters, i.e. cooling rate, solidification rate and temperature gradient are assessed as a function of welding speed using thermocouple and dendrite arm spacing measurements as well as analytical calculations. The agreement between different measurement methods, calculations and reference data supported the present study by providing a reliable basis for modelling.

4) Transmission electron microscopy (FEG-STEM) with a high resolution capability is applied to demonstrate the effect of increasing welding speed and solidification rate on the magnitude of microsegregation of welds. The measurements agree with the results obtained by electron probe microanalyses (EPMA) and confirm the beneficial effect of increasing solidification rate on weld microsegregation.

5) The segregation behaviour of nitrogen that takes place during weld solidification and cooling is validated via modelling and experimental measurements. This gives new information that can be applied in critical evaluation of the role of nitrogen in pitting corrosion resistance of segregated welds.

1. Introduction

1.1 Problem description

Solidification of weld plays an important role in controlling the quality and mechanical properties of welded joints. The solidification behaviour controls the extent of segregation and distribution of inclusions and also contributes to the formation of weld defects such as porosity and hot cracking. After solidification also the weld grain size is large reflecting inferior mechanical properties compared to base metal. Consequently, the weld metal, sometimes referred to a “miniature casting”, is often a critical factor with respect to the structural integrity of welded components. To avoid and minimise these mismatch problems the understanding of solidification and subsequent transformation of the weld metal is of essential importance.

To understand the correlations between weld solidification, microstructure and properties there exists a need to link the basic solidification parameters such as solidification rate, temperature gradient and cooling rate with the microstructural characteristics of the weld metal. These correlations are illustrated in Fig. 1.1 that schematically demonstrates the formation of solidification structure of a weld produced by a moving heat source. The solidification of a weld pool starts epitaxially from the base metal crystals and proceeds towards the weld centerline. The solidification rate, the temperature gradient and the cooling rate vary considerably through the solidifying weld pool. Due to these constant changes in solidification parameters also the morphology of solidified weld changes from the fusion line towards the weld centerline.

Arising from constant change of the solidification parameters, the resulting microstructure of welds becomes complicated. The complexity is further increased by solid state transformations taking place after subsequent weld solidification. A classical example is the solidification of austenitic stainless steel welds which, depending on composition, can have as many as five different solidification modes and, further, as many as eleven different solid state morphologies of ferrite and austenite (Elmer 1988). As a result, the mechanical and corrosion behaviour as well as cracking susceptibility of welds can vary in a wide range.

In the recent years modelling of weld pool behaviour has became a powerful tool for better understanding of the weld phenomena. With computational modelling significant progress has been made in evaluating how the physical processes prevailing in the weld pool influence the weld pool development and phase transformations. Macroscopic scale modelling of fluid flow and heat transfer in the weld pool has been extensively studied in order to understand the effect of these parameters on pool size and shape. Further, computational modelling of the welding process can provide detailed information on weld cooling rates, temperature gradients, microstructural development and residual stress distribution in the welded structures (David et al. 1994, DebRoy & David 1995).

The present investigation focuses on the solidification and microsegregation of austenitic stainless steel welds predicted using numerical modelling. A number of mathematical and computer aided models of weld phenomena are applied to demonstrate the role of heat and fluid flow, solidification mode and solute redistribution on weld geometry, microstructure and segregation behaviour. The main emphasis is laid on the effect of welding speed and consequent solidification rate and morphology on weld pitting corrosion behaviour.

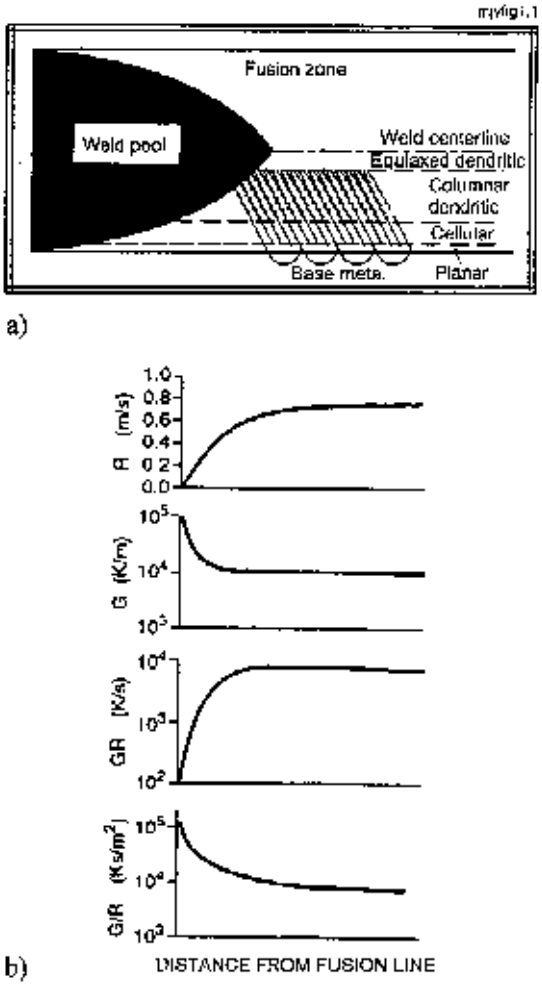

Fig. 1.1. Schematic illustration of weld microstructure across the fusion zone (a) and corresponding schematic variation of R solidification rate, G temperature gradient, GR cooling rate and ratio of G/R as a function of position (b) (David & Vitek 1989, Kurz 1995).

1.2 Weld pool behaviour

Weld pool characteristics depend on interactions between the heat source and the base metal, heat and fluid flow, thermophysical and chemical properties of the material and allied boundary conditions. Understanding the physics and chemistry of the weld pool is of great practical importance to control the effects of solidification phenomena on weld cracking as well as mechanical and corrosion properties.

1.2.1 Heat and fluid flow and weld geometry

On the macroscopic scale the weld pool undergoes vigorous circulation driven by different forces acting on the fused metal. These forces have a direct impact on the size and shape of the weld pool, which, in turn, have an effect on local cooling rates and the kinetics of phase transformations during solidification and even in the solid state. The forces affecting weld pool convection can be classified according to Fig. 1.2 as follows (Heiple & Roper 1982, Matsunawa et al. 1987, Mills & Keene 1990, Choo et al. 1992, DebRoy & David 1995):

- Surface tension force, which is generated due to local variations in pool temperature and composition resulting in Marangoni flow in the pool. Flow rates as high as 0.5 to 1 m/s have been measured or calculated to prevail in weld pools due to Marangoni flow. In conventional low current arc welding, surface tension forces and their directions have been demonstrated to dominate the development of pool shape and penetration.

- Electromagnetic force developing as a consequence of the interaction between the current path in the pool and the magnetic field it generates. The importance of the electromagnetic component increases with the magnitude of the welding current.

- Buoyancy force originating from the spatial variation of liquid metal density which depends mainly on temperature variations and to a minor extent also on local compositional variations. The magnitude of the buoyancy force remains relatively weak in welding causing flow of 0.01 to 0.03 m/s in the pool.

- Plasma drag effect which is based on the aerodynamic force caused by the flow of plasma in the weld pool surface. The effect of the plasma drag force becomes more important with increasing arc length.

During arc welding the above mentioned forces operate simultaneously in the weld pool having a direct effect on flow velocity, temperature fields and the resulting pool shape. Depending on the relative magnitude of each force, large variations in fluid flow, weld pool shape and penetration can be obtained. For instance, in high current arc welding, such as submerged arc process, the electro-magnetic force dominates and largely dictates the weld pool shape and formation of deep penetration. In low-current arc welding, such as gas tungsten arc process,

the electromagnetic induced convection is weaker and the role of other force components becomes more dominant. In this case the surface tension forces have been demonstrated to dictate weld pool geometry and penetration. The role of surface tension force largely depends on the direction and magnitude of the surface tension temperature gradient ($d\gamma/dT$) which can result in inward or outward directed fluid flow. In the case of positive $d\gamma/dT$ - which is the case with higher amounts of surface active elements such as sulphur and oxygen - inward flow and deeper penetration is generated. With negative $d\gamma/dT$, arising from low amounts of surface active elements, outward flow takes place leading to shallow penetration. In practical welding the variation of surface tension forces from cast to cast can cause difficulties to reach required penetration. This easily leads to either insufficient or excessive penetration with the same welding parameters (Leinonen 1987, Mills & Keene 1990, Burgardt & Campbell 1992).

In laser welding no electromagnetic force exists and the weld pool flow is controlled by the three other force components. At the weld surface region the surface tension and plasma drag forces result in strong pool flow and good mixing. In the bulk of the weld pool, mixing of laser welds may, however, remain weaker. Arising from high temperature gradients present in the laser weld pool, the fluid flow caused by the buoyancy force is stronger than in arc welding which partly increases pool flow in the bulk weld pool (Kou & Wang 1986).

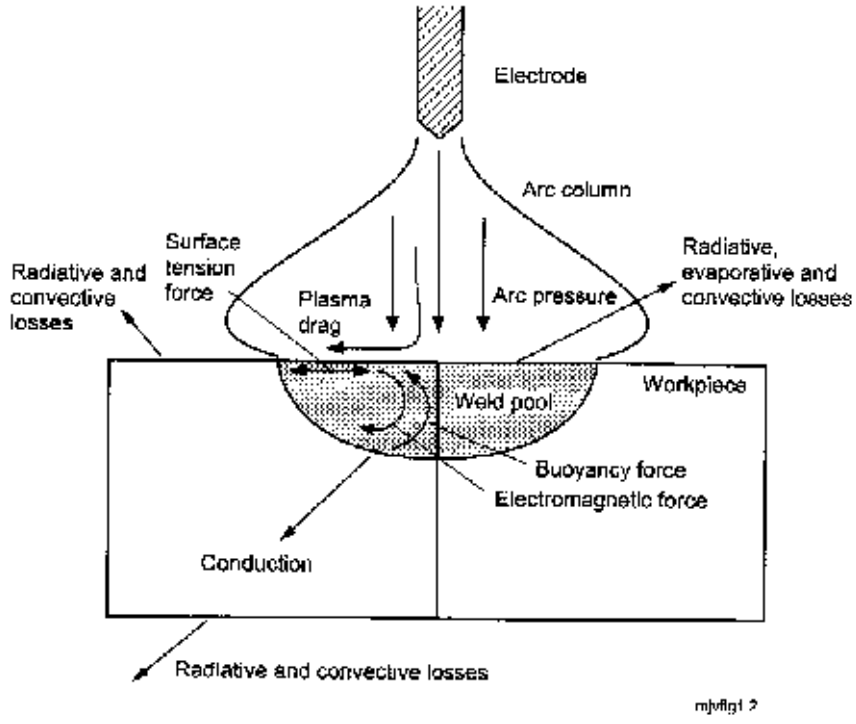

Fig. 1.2. Schematic representation on weld pool phenomena in arc welding (Choo et al. 1992, Winkler et al. 1997).

1.2.2 Weld pool solidification

In solidification of a weld pool the base metal acts as a substrate from which the growth of the solid phase can occur. Thus, the solidification starts by epitaxial nucleation from partially melted base metal crystals. This means that the solidification starts in the same orientation as the base metal crystals in the vicinity of the fusion boundary. In fcc and bcc metals solidification proceeds most easily in one of the <100> directions (Kurz & Fisher 1992). Since the solidification is controlled by the heat flow conditions present in welds the <100> grains growing parallel to the maximum temperature gradient will displace other less favourable growth directions. This phenomenon is called competitive growth (Kou & Lee 1982, Rappaz et al. 1989).

According to David & Vitek (1989) the growth rate of a dendrite growing to crystallographic direction <hkl> can be related to the weld travel speed according to the equation:

$$R_{hkl} = |v| \frac{\cos\theta}{\cos\psi}, \tag{1}$$

where θ refers to the angle between the normal of the solidification front and the welding direction. Correspondingly, ψ refers to angle between the normal of the solidification front and crystallographic growth direction <hkl>. In single crystals this equation has been successfully applied for better understanding the solidification phenomenon for different crystallographic orientations (Rappaz et al. 1990, David et al. 1995).

In polycrystalline materials <100> type growth can take place in any direction dictated by epitaxial nucleation from the base metal crystals. In this case a grain growth selection process takes place so that the grains having one of their <100> directions close to the solidification front normal direction, i.e., minimum angle ψ, becomes favourable. Consequently, grain growth with minimum undercooling becomes possible and dendrites growing parallel to the solidification front normal can overtake grain growth in other orientations. According to the two dimensional analysis presented by Kou & Lee (1982) the solidification rate can be related to the welding speed by the following equation:

$$R = \frac{v\cos\theta}{\cos(\theta - \phi)}, \tag{2}$$

where angle θ is defined as above and angle $(\theta-\phi)$ refers to the deviation from the normal of the solidification front, c.f. Fig. 1.3. In the normal direction, the angle $(\theta-\phi)$ becomes zero and the solidification rate is: $R = v\cos\theta$. With increasing angle $(\theta-\phi)$ the local solidification rate is forced to increase in order to keep the solidification front aligned to the direction of maximum temperature gradient. With the value $(\theta-\phi) = 45°$ the maximum solidification rate $R = \sqrt{2}\, v\cos\theta$ is reached. With the values of angle $(\theta-\phi)$ in excess of 45° the growth process becomes unstable and tends to select another more favourable <100> direction

(Kou & Lee 1982, Grong 1997). Depending on growth direction the local solidification rate of a weld can, thus, vary in a wide range. Due to competitive growth fusion welds of bcc and fcc metals will also develop a sharp <100> texture in the columnar grain region as documented also for ingots and castings (Flemings 1974, Grong 1997).

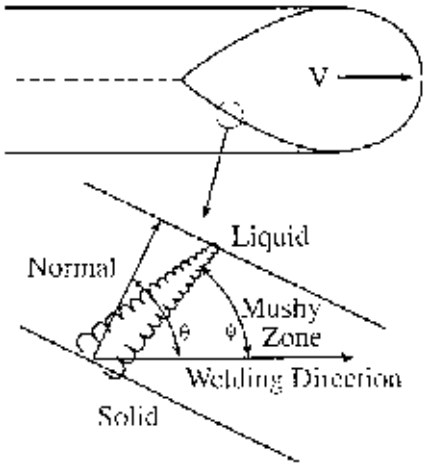

Fig. 1.3. Schematic representation on relationships between dendrite tip growth direction and velocity with respect to solidification front and temperature gradient (Kou & Lee 1982).

Temperature gradient G is another important factor having an effect on solidification conditions and the resulting microstructures. As illustrated by Fig. 1.1 both temperature gradient G and solidification rate R will vary considerably during solidification of a weld pool. It is generally accepted that the ratio of temperature gradient and solidification rate, G/R, correlates with the resulting solidification morphology. The composition of the solidifying weld pool is another important factor in this respect (David & Vitek 1989, Kurz & Fisher 1992, Brooks 1995). In the beginning of solidification the G/R ratio is at its maximum and the solidification starts with planar morphology, c.f. Fig. 1.4. Constant decrease of the G/R ratio results in rapid transition from planar to cellular morphology as soon as the following interface stability criterion is met (Flemings 1974, David & Vitek 1989):

$$\frac{G}{R} < -\frac{mC_0(1-k)}{kD_L} = \frac{\Delta T}{D_L} \qquad (3)$$

In equation (3) m is the slope of liquidus line, C_o composition of melt, k equilibrium partition ratio, D_L diffusion coefficient of solute in liquid and ΔT temperature interval between liquidus and solidus at composition C_o.

As solidification proceeds there is a further tendency for cellular morphology to change to cellular-dendritic and even to equiaxed dendritic morphology towards the weld centerline, c.f. Fig. 1.4. It is apparent from equation (3) that an increase in alloy content C_o and a decrease in partition ratio k will increase the magnitude of constitutional supercooling and, thus, the tendency to favour the formation of dendritic morphologies instead of cellular one.

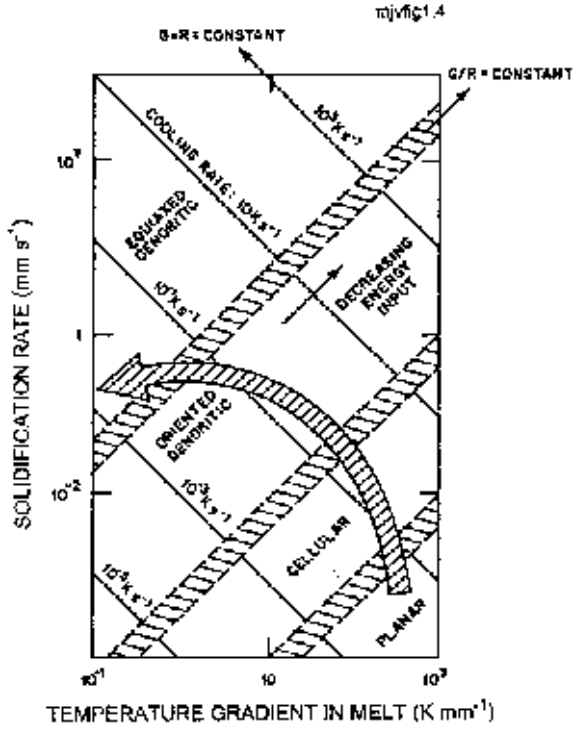

Fig. 1.4. Schematic illustration of weld microstructure across the fusion zone as a function of temperature gradient and solidification rate. The G/R constant lines correlate with the solidification morphology and the GR constant lines dictate the scale of the solidification substructure (David & Vitek 1989).

The product of temperature gradient and solidification rate, i.e., the cooling rate GR, on the other hand, dictates the scale of solidification microstructures, higher values leading to finer structures measured in terms of primary or secondary dendrite arm spacing. The functional dependence of the primary arm spacing d_1 and secondary arm spacing d_2 on G and R can be derived from the solidification theory (Flemings 1974, Hunt 1979, David & Vitek 1989):

$$d_1 = a_1(G^2R)^{-1/4} \tag{4}$$

$$d_2 = a_2(GR)^{-n} \tag{5}$$

where n = 1/3…1/2 and a_1 and a_2 are coefficients whose values depend on the alloy system. A direct correlation between d_2 and GR exists and the secondary spacing can, thus, be directly used in cooling rate estimation. In addition to the previous theoretical dependencies, several empirical correlations between primary and secondary spacing and measured cooling rates have been developed (Katayama & Matsunawa 1984, Nakao et al. 1988, Zacharia et al. 1989a).

Typical values measured or calculated for cooling rates and average temperature gradients of the weld pool are gathered in Table 1.1. The cooling rate as well as the temperature gradient depend largely on the applied welding process and parameters. With decreasing weld heat input both solidification parameters increase. As a result the weld microstructure and properties are expected to vary in a wide range.

Table 1.1.Typical values for cooling rates and temperature gradients during weld pool solidification.

Cooling rate	**GR (K/s)**	**Ref.**
Ingot and continuous casting	0.01 - 100	Flemings (1974)
Arc welding	$10 - 10^3$	Grong (1997)
EB and laser welding	$10^3 - 10^6$	David & Vitek (1989), Sahm & Schubert (1979), Grong (1997)
EB and laser surface melting	$10^5 - 10^7$	Elmer (1988)
Pulsed laser (200 W)	$1\text{-}9 \cdot 10^5$	Zacharia et al. (1989a),
Pulsed laser (120 W)	$0.1 - 2.3 \cdot 10^6$	David & Vitek (1989)

Temperature gradient	**G (K/mm)**	**Ref.**
Arc welding	40 - 300	David & Vitek (1989)
EB welding	$10^2 - 10^5$	Sahm & Schubert (1979)
EB and laser surface remelting	$10^4 - 10^6$	Elmer (1988), Zacharia et al. (1989a)

1.3 Solidification and cooling of austenitic stainless steel welds

1.3.1 Microstructural prediction

The solidification of stainless steels and welds has been intensively studied and the resulting microstructures classified by several authors (Takalo et al. 1979, Suutala et al. 1979, 1980, Brooks & Thompson 1991, Katayama et al. 1985, Elmer 1988). Consequently, the solidification of austenitic stainless steels is relatively well understood although the terminology differs between authors. According to Suutala & Moisio (1980) the solidification can be divided to four main modes as follows (Fig. 1.5):

- Single phase austenitic solidification (A-mode), in which the melt solidifies completely to austenite with no further transformation to ferrite.

- Primary austenitic solidification (AF-mode), where austenite is the leading phase during solidification and δ-ferrite is formed from the rest of the melt between austenite dendrites as a result of microsegregation.

- Primary ferritic solidification (FA-mode), ferrite being the leading phase and austenite is formed between the ferrite dendrites through peritectic or eutectic reaction between liquid, ferrite and austenite. When austenite is formed it grows into the ferrite resulting in a drastic decrease in the volume fraction of ferrite. In the final phase of solidification small amounts of secondary ferrite can form interdendritically as a result of microsegregation.

- Single phase ferritic solidification (F-mode), where ferrite is the only phase in solidification. After solidification austenite nucleates preferentially at ferrite grain boundaries growing into ferrite by the Widmanstätten mechanism.

After solidification and solid state transformations several different microstructural morphologies can be detected in the weld metal. These can be classified as follows (Takalo et al. 1976, Brooks & Thompson 1991, Katayama et al. 1985, Elmer 1988):

- A-mode welds consisting of austenite dendrites and/or cells, depending on solidification conditions.

- AF-mode welds showing austenite with interdendritic and/or intercellular ferrite in the last solidified regions.

- FA-mode welds with austenite and vermicular or skeletal ferrite are present at dendrite cores. In these welds secondary ferrite can sometimes be detected at the interdendritic regions. By increasing the amount of ferritizing elements (Fig. 1.5) vermicular ferrite is replaced by lathy or lacy type ferrite growing as parallel plates into the austenite.

- F-mode welds including ferrite plus Widmanstätten or lathy or acicular austenite. In high cooling rate welds the microstructure can include ferrite and austenite produced by massive transformation. With high Cr_{eq} / Ni_{eq} ratios, the weld microstructure can be fully ferritic.

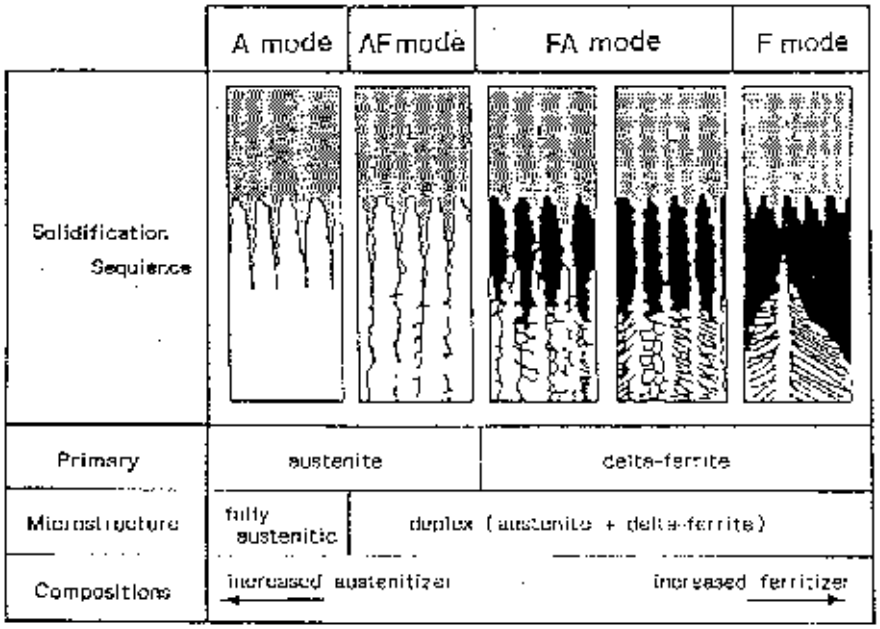

Fig. 1.5. Solidification modes of austenitic stainless steel welds after Suutala & Moisio (1980).

The solidification mode and resulting microstructure depend on the weld chemical composition, especially on the ratio of "ferritizing" and "austenitizing" elements. For AISI 300-series steels Suutala (1981) found the best correlations between the analysis and the corresponding solidification mode when using Hammar & Svensson's (1979) equivalents:

$$Cr_{eq} = Cr + 1.37Mo + 1.5Si + 2Nb + 3Ti \quad (6)$$

$$Ni_{eq} = Ni + 0.31Mn + 22C + 14.2N + Cu \quad (7)$$

By using these equivalents the solidification mode of austenitic stainless steels can be predicted with reasonable accuracy when conventional arc welds are concerned. Based on the equivalents a solidification development map shown in Fig. 1.6 has been developed and it has been successfully applied for predicting weld microstructures of conventional arc welds (Kujanpää 1984, Kujanpää et al. 1987).

In high energy density welding the microstructures do, however, deviate from the prediction of Fig. 1.6. Also the well-known Schaeffler, DeLong and WRC diagrams fail in predicting the ferrite content of electron and laser beam welds (David et al. 1987). Correspondingly, Lippold (1985) reported increased susceptibility of electron beam welds to solidification cracking due to primary austenitic solidification at crack sensitive weld centerline regions in steels which, according to conventional prediction models, should solidify in primary ferritic mode.

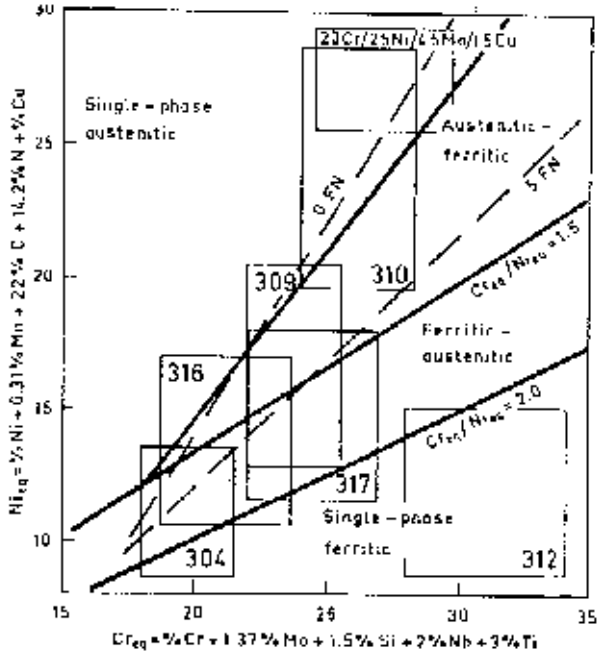

Fig. 1.6. Solidification diagram for the prediction of solidification mode in conventional arc welding of austenitic stainless steels (Kujanpää 1984).

Subsequent studies on high energy density welds demonstrated that the AF/FA demarcation line tends to shift to higher Cr_{eq}/Ni_{eq} ratios with increasing solidification and cooling rates. The studies of Katayama & Matsunawa (1984) indicate that the FA/F demarcation line correspondingly shifts towards lower Cr_{eq}/Ni_{eq} ratios. Further investigations have attempted to develop microstructural maps for solidification and cooling of high energy density welds (David et al. 1987, Nakao et al. 1988, Elmer 1988). The most recent paper on the subject, proposed by Lippold (1994), includes a 3rd dimension, solidification rate, see Fig. 1.7. The diagram clearly shows the tendency of the demarcation lines to approach each other with increasing solidification rate. For solidification rates in excess of about 10–30 mm/s, two-phase solidification will be replaced by single phase solidification, i.e. either to austenite or to ferrite. In these high cooling rate welds a further transformation of ferrite to austenite via massive transformation becomes

possible as reported earlier by Suutala et al. (1981), Elmer (1988), Nakao et al. (1988) and Brooks & Thompson (1991).

The effect of enhanced solidification and cooling of high energy density welds on the room temperature microstructures can be revealed from modified Schaeffler diagram, see Fig. 1.8. A significant decrease in the width of the duplex region can be noticed with increasing weld cooling rate. Corresponding results are reported also by Katayama & Matsunawa (1984) and Nakao et al. (1988).

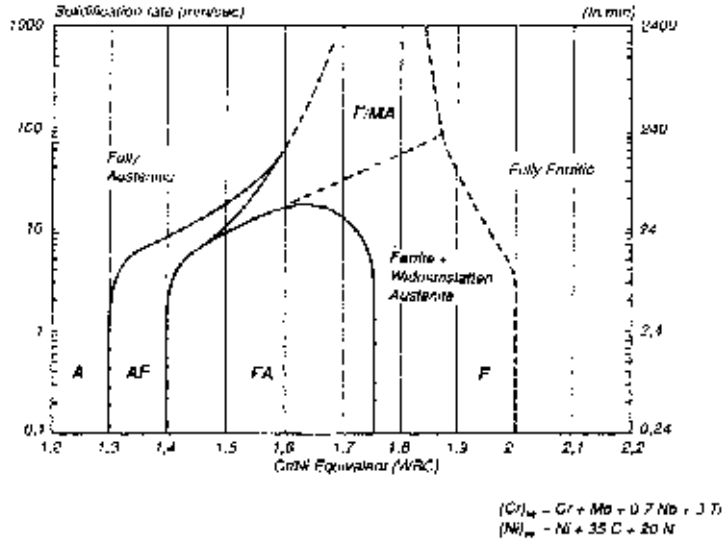

Fig. 1.7. Preliminary microstructural map for austenitic stainless steel welds as a function of solidification rate (Lippold 1994). The designations A, AF, FA and F refer to the solidification mode explained in text. MA refers to transformation of ferrite to austenite through massive transformation.

Microstructural changes shown in Figs 1.7 and 1.8 have been explained using the following factors:

- With increasing solidification rate and dendrite tip undercooling, the growth of primary austenite dendrites or cells becomes kinetically favourable (Suutala 1981, 1983, David et al. 1987, Brooks & Thompson 1991, Bobadilla et al. 1996).
- The formation of second phase ferrite in AF-mode and second phase austenite in FA-mode is suppressed because the primary solidifying phase incorporates more solute than it does closer to equilibrium conditions (Elmer et al. 1989).
- In FA-welds solid state transformation from ferrite to austenite is suppressed because of high cooling rate and retarded diffusion (David et al. 1987, Katayama & Matsunawa 1984).

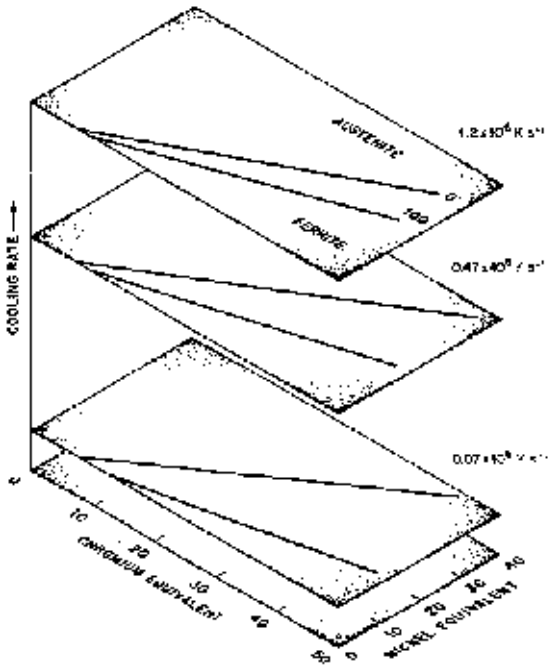

Fig. 1.8. The effect of weld cooling rate on the duplex-region of the Schaeffler diagram (David et al. 1987).

Arising from the previous factors the δ-ferrite content of high energy density welds can considerably deviate from conventional arc welds. As shown by Fig. 1.8 the difference from conventional welds increases with weld cooling rate. At the highest cooling rates a great number of welds having duplex microstructures in arc welding are replaced by single phase austenitic or single phase ferritic microstructures in high energy density welding. The results of Katayama & Matsunawa (1984) propose that in welds predicted to have less than 8% ferrite according to Schaeffler diagram will transform to fully austenitic with cooling rates of as high as 200000 K/s. On the other hand, arc welds predicted to have more than 30% ferrite may become fully ferritic with these very high cooling rates. In these welds massive transformation to austenite may, however, abruptly decrease the ferrite content (Elmer 1988, Nakao et al. 1988, Lippold 1994, Brooks & Thompson 1991, Inoue et al. 1995).

1.3.2 Solute redistribution

Solute redistribution during solidification and subsequent solid state transformation have substantial effects on weld properties, corrosion behaviour and cracking sensitivity. In austenitic stainless steels the magnitude of microsegregation and partitioning of alloying elements is known to depend mainly on solidification mode and weld composition and secondly on cooling and solidification rates typical of castings and arc welds (Fredriksson 1976, Suutala & Moisio 1980, Kujanpää et al. 1987, Gooch 1996).

Cieslak et al. (1982) have demonstrated the effect of weld solidification mode on microsegregation of Cr and Ni, see Fig. 1.9. They noticed that during fully austenitic solidification both Cr and Ni segregate in the same phase towards the interdendritic region (Fig. 1.9a). On the contrary, in fully ferritic solidification Cr and Ni segregate in opposite phases, the former to dendrite cores and the latter to interdendritic regions (Fig. 1.9b). In both primary austenitic and primary ferritic solidification the formation of second phase, i.e. ferrite (Fig. 1.9c) or austenite (Fig. 1.9d) in the residual melt changes the direction of segregation opposite.

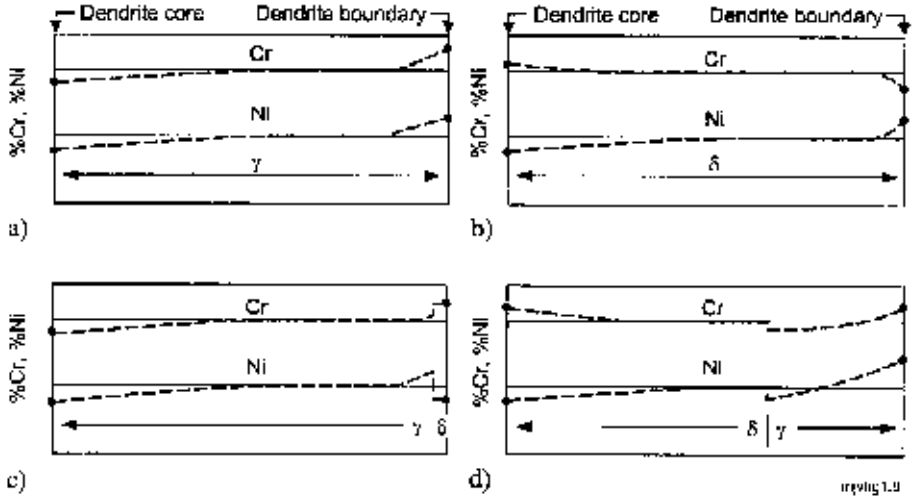

Fig. 1.9. Solidification of austenitic weld metal. Complete solidification to austenite (a), complete solidification to ferrite (b), primary solidification to austenite with precipitation of δ-ferrite in residual melt (c), primary solidification to δ-ferrite with solidification to second phase austenite in the residual melt (d) (Cieslak et al. 1982).

The segregation behaviour of all main alloying elements present in austenitic stainless steel welds are further reviewed in Fig. 1.10 which shows the effect of Cr_{eq}/Ni_{eq} ratio on the magnitude and direction of microsegregation. It can be seen that in primary austenitic solidification ($Cr_{eq}/Ni_{eq} < 1.5$) the segregation ratio $S = C_{id}/C_{core}$ is well above 1 indicating interdendritic segregation for all alloying elements studied. The segregation of Ni remains, however, reasonably weak. The melt at the interdendritic regions is, thus, enriched especially in Cr and Mo and can form interdendritic ferrite. Correspondingly, the concentration of Cr and, especially Mo, at the dendrite cores becomes lower than in the bulk composition.

In primary ferritic solidification ($Cr_{eq}/Ni_{eq} > 1.5$) the value of segregation ratio for all other elements except for Ni is lower than in primary austenitic mode. This means that the segregation tendency of Cr and Mo decreases and that of Ni increases with respect to primary austenitic solidification. Due to segregation, the residual melt may solidify as austenite which changes the segregation profiles as shown in Fig. 1.9d. In the very final stage of solidification the last melt droplets

can once again solidify as ferrite, known as secondary ferrite. Due to high segregations of Cr and Mo, secondary ferrite is known to be susceptible to the formation of intermetallic phases such as σ or χ (Suutala 1980, Suutala et al. 1980).

When comparing the segregation behaviour for different solidification modes it has been demonstrated that microsegregation is stronger in welds having primary austenitic solidification (Arata et al. 1976, Suutala & Moisio 1980, Katayama et al. 1985, Kujanpää et al. 1987). This arises from larger solidification temperature range during primary austenitic solidification. The inhomogeneity is affected also by considerably slower diffusion of alloying elements in austenite than in ferrite. Therefore, the segregation profiles developed in austenitic solidification are not homogenised during cooling to the same extent as in ferritic solidification (Fredriksson 1972, 1976, Brooks & Thompson, 1991, Campbell 1991).

The inhomogeneity of austenitic stainless steel welds is affected not only by microsegregation but also by the partitioning of alloying elements between ferrite and austenite during solid state transformation of δ-ferrite to austenite. This has an effect on the final degree of inhomogeneity especially in primary ferritic solidification. It is noticed that the solid state transformation results in an enrichment of δ-ferrite in “ferritizers” Cr and Mo and enrichment of austenite in “austenitizer” Ni, see Fig. 1.10b. Consequently, partitioning changes the segregation profile produced by solidification in welds where δ/γ transformation takes place. The role of partitioning is particularly dominant in welds that solidify in primary or fully ferritic modes and show extensive transformation in the solid state. In fully or primary austenitic welds the microsegregation pattern produced by solidification remains to a larger extent in the microstructure (Brooks & Thompson 1991).

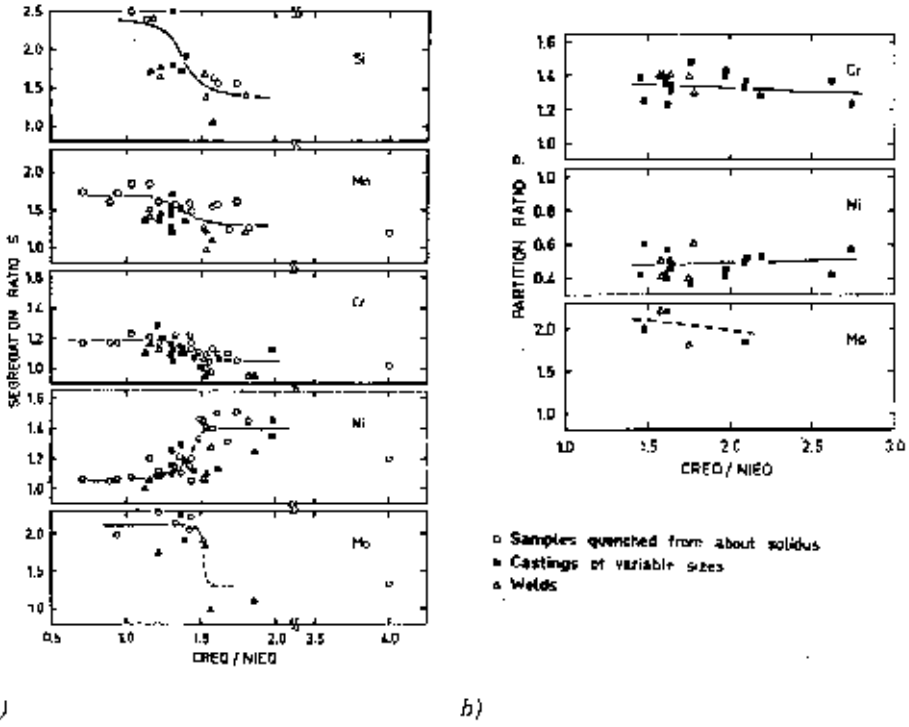

Fig. 1.10. The effect of weld composition on the segregation ratio $S = C_{id} / C_{core}$ (a) and partition ratio $P = C_{\delta}/C_{\gamma}$ (b) (Suutala & Moisio 1980).

1.3.3 Effects on corrosion resistance

The majority of corrosion failures of stainless steels and their welds is caused by localised attack called pitting or crevice corrosion. Attack of this kind occurs mainly in neutral-to-acid solutions containing chloride ions. Corrosion starts from a local breakdown of the passive film on the stainless steel surface succeeded by reasonably quick pit growth below corrosion products and constructional crevices.

Mechanism of pitting corrosion

The mechanism of pitting corrosion is divided to two phases: initiation and propagation. In the initiation phase local microscopic irregularities on the passive surface layer play an important role. Grain boundaries, inclusions (sulphides, oxides, nitrides etc.) and local segregation of alloying elements can act as irregularities which initiate pitting corrosion (Szklarska-Smialovska 1960). The role of sulphur and sulphides in the initiation process has been shown to be clearly detrimental (Eklund 1974, Manning et al. 1980a, Sedriks 1983). The initiating effect of more complex inclusions has also been demonstrated (Kyröläinen 1984, Dowling 1995). In stainless steels the initiation of pits at inclusions has been

explained to arise from lower nobility of inclusions with respect to the surrounding matrix (Wranglen 1974). In this way stainless steel below the protective surface layer becomes exposed which makes pit growth possible. The mechanism of pitting corrosion can, thus, be considered as crevice corrosion in microscale.

Pit growth is an autocatalytic process which means that the corrosion reactions within a pit produce conditions that are both stimulating and necessary for the continuing activity of the pit. Pit growth is associated with hydrolysis of the dissolved metal ions which results in lower pH in the pit than in the surrounding environment. The increased concentration of M^{n+} ions within the pit results in a migration of Cl^- ions to maintain neutrality. The metal chloride (M^+Cl^-) is, further, hydrolysed by water to metal hydroxide and free acid according to the following reaction:

$$M^+Cl^- + H_2O \rightarrow MOH + H^+Cl^- \quad (8)$$

The generation of acid further lowers the pH values at the bottom of the pit while the pH of the bulk solution remains neutral. The metal dissolution at the bottom of the pit is balanced by the cathodic reaction on the unattacked metal surface where the electrons liberated by the anodic reaction are consumed (Jones 1992).

Effect of composition

The effect of alloying elements on pitting corrosion has been intensively studied. It has been clearly demonstrated that the main alloying elements of stainless steels Cr, Ni, Mo and N improve the pitting corrosion resistance. The effect of manganese has, however, been found detrimental, due to formation of sulphides. Impurities and alloying elements like S, Se, Te, Ti, Nb, Ce also have an adverse effect on pitting corrosion resistance (Sedriks 1979, Mitrovic-Scepanovic & Brigham 1996).

The role of main alloying elements on pitting corrosion resistance can be summarised into an empirical compositional parameter, called previously ”efficiency sum” and currently ”pitting resistance equivalent” (PRE), which is given in the form:

$$PRE = \%Cr + \mathbf{a}*\%Mo + \mathbf{b}*\%N \quad (9)$$

For evaluation of the critical pitting corrosion temperature (CPT) in 10% $FeCl_3$ solution, the value for coefficient **a** is normally close to 3, most often 3.3 (Brandis & Kiesheyer 1984, Rockel et al. 1991, Heubner & Rockel 1986). Reported values for coefficient **b** deviate in various studies but values between 13 - 30 have been suggested (Rondelli et al. 1995, Rockel et al. 1991, Renner et al. 1986, Suutala & Kurkela 1984).

Pitting corrosion of welds

The inhomogeneity of welds makes them more susceptible to localised corrosion than the corresponding base metals. Pitting corrosion attacks and propagates easiest to regions where Cr and Mo contents are locally depleted due to microsegregation and partitioning, the precipitation of carbides and the formation of intermetallic phases.

The solidification mode is one of the key factors having an effect on pit initiation and growth. In fully austenitic solidification the dendrite cores are observed to be the most critical sites for initiation and growth. This arises from microsegregation of Mo and Cr to interdendritic regions with the result that the dendrite cores are depleted of these elements (Garner 1977, 1982, 1983, Ogawa et al. 1982, Marshall & Gooch 1993). In case of primary austenitic (AF) solidification pits have been observed to nucleate at the phase boundaries of austenite and interdendritic ferrite and to propagate along the austenitic dendrite cores. In a similar manner welds showing primary ferritic (FA) solidification exhibit pit initiation at the δ/γ phase boundaries where pit propagation to austenite takes place leaving ferrite network unaffected (Grekula et al. 1984, Cieslak et al. 1981). The role of δ/γ interfaces has been demonstrated to be clearly detrimental. This has been reasoned to arise from segregation of impurities (Manning et al. 1980a, b). Fenn et al. (1985) and Fenn & Newton (1986) have demonstrated that the pit initiation at the δ/γ-phase boundaries is associated with local depletion of Cr and Mo at the γ-side, arising from precipitation of carbides at the interface.

As a result of the inhomogeneity caused by the factors described above the CPT-temperatures measured for welds always fall below those of the base metals, see Fig. 1.11. It is noticeable that the slope of the CPT - PRE curves is different for base metals and welds. The measurements show a significant amount of scatter, which is due mainly from differences in alloying, ferrite content, impurity level and differences in welding procedure, especially in heat input. Higher heat input is reported to have an adverse effect since it leads to coarser dendrite structure, more pronounced microsegregation and, hence, to lower CPT-temperature (Garner 1982). In nitrogen alloyed steels welding may also cause excessive nitrogen loss from the weld pool which will reduce pitting corrosion resistance in the weld metal. This can be partly eliminated by using nitrogen addition in the shielding gas (Ogawa et al. 1982, Leinonen et al. 1991, Ginn 1992, Liljas et al. 1992). The nitrogen uptake into the weld metal depends, however, strongly on the welding parameters and weld dimensions. In the recent work of Hertzman & Wessman (1998) it has been demonstrated by modelling and experiments that the use of high welding speed and small weld volume result in a more efficient nitrogen pick-up.

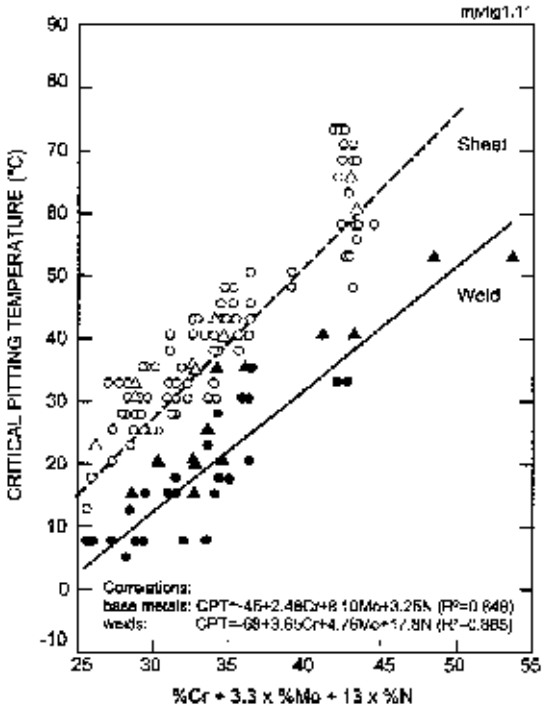

Fig. 1.11. CPT-temperatures of base metals and autogenous GTA-welds for austenitic stainless steels as a function of PRE-index according to Suutala & Kurkela (1984).

1.4 Modelling of weld solidification

Numerical modelling and simulation techniques have increasingly been used in understanding the solidification phenomena of welds. The use of computational modelling makes it possible to evaluate how the physical processes present in the weld pool influence pool development as well as on weld solidification morphology and weld microstructure. Depending on the phenomena investigated, numerical simulation can be carried out either on macroscopic or microscopic scales which are reviewed separately in the following sections.

1.4.1 Macroscopic modelling

In weld pool simulation, computational modelling has been used mainly in evaluating the role of physical processes typical of welding on pool development as well as on the macrostructures of welds. Much of the research work has been attempted to gain understanding of how fluid flow and heat transfer affect weld pool convection and, further, on shape and size of a weld pool (Kou & Wang 1986, Zacharia et al. 1995, Mundra et al. 1996).

The macroscopic calculations are based on conservation of mass, momentum and energy by applying finite difference (FDM) or finite element (FEM) codes. The application of these modelling tools has made it possible to demonstrate the effects of surface tension, electromagnetic buoyancy and plasma drag forces (Fig. 1.2) on heat flow, weld pool formation and on final shape of a fusion weld. A typical example is shown in Fig. 1.12 which demonstrates the calculated fluid flow pattern in a stainless steel weld pool.

Due to the complexity of the flow phenomena an accurate simulation of a weld pool is demanding and requires a substantial amount of computation time. Consequently, one has to judge the extent of simplifications that can be tolerated for a particular application. The choice between two- or three-dimensional simulations is one possibility to simplify calculations. The use of steady state instead of transient calculations, flat weld-pool instead of free-deformable surface and laminar instead of turbulent fluid flow will also considerably decrease the computation time. These simplifications, on the other hand, result in deviations and insufficient data with respect to experimental measurements (DebRoy & David 1995).

Macroscopic modelling of fusion welds has been first reported by Kou & Wang (1986) by using two-dimensional calculations for 6061 aluminium alloy welds. They used a moving GTAW heat source where the x-y-z coordinate system was fixed with the electrode. The pool convection included the calculated effect of electromagnetic, buoyancy and surface tension forces assuming a laminar fluid flow. The calculations showed the dominating effect of the surface tension forces on weld pool flow formation in agreement with experimental measurements of Burgardt & Campbell (1992). The validity of the model was supported by good agreement with experimentally observed fusion boundaries. Corresponding simulations for austenitic stainless steel welds were carried out by Zacharia et al. (1989b, c). They studied the development of a weld pool of stationary GTA and laser welds of type 304 stainless steel using sulphur levels of 90 and 240 ppm. With development of their model the beneficial effect of sulphur on weld penetration could be demonstrated showing good correlation with experiments. Pitscheneder et al. (1996) have made further simulations for laser spot welds with varying sulphur content (20 vs. 150 ppm) and laser beam power (1.9, 3.85 and 5.2 kW). They showed that the sulphur content increases weld penetration provided that the heat transfer of the weld pool takes place by convection. With the lowest laser beam power used, the heat transfer occurred mainly by conduction which resulted in nearly similar pool shapes both with low and high sulphur contents.

Further development of computer and programming capabilities has made three-dimensional simulations of a weld pool possible. Mundra et al. (1996) presented their computational analysis for the detailed prediction of heat transfer and fluid flow with a moving heat source. The computations were carried out in a coordinate system attached to the moving heat source. A control-volume based computation was used in this analysis. The calculation facility has been applied in the prediction of velocity and temperature fields, size and shape of fusion zone and cooling rates at different weld locations. By further linking the calculated

cooling curves to time-temperature-transformation (TTT) diagrams the prediction of weld microstructures of low-alloyed steels became possible (Mundra et al. 1997a, Yang & DebRoy 1998). In the recent work of Hong et al. (1998) the same model has been further applied in simulation of nucleation, growth and circulation of oxide particles during weld pool convection. Recently the model has been used also in predicting spatial distribution of hydrogen concentration in the weld metal during gas metal arc welding of mild steels (Mundra et al. 1997b).

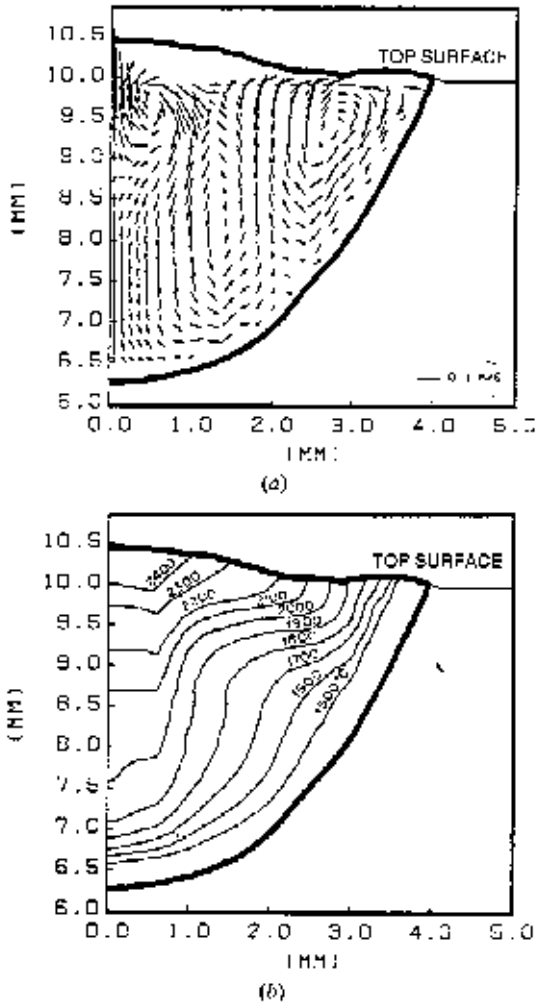

Fig. 1.12. Calculated fluid-flow pattern (a) and temperature field (b) in a stationary arc weld of a stainless steel weld pool 25 seconds after the initiation of the arc. The flow is driven by combined effect of surface tension, electromagnetic and buoyancy forces resulting in the case studied in a multiple vortex flow (Zacharia et al. 1991).

1.4.2 Microscopic modelling

In the microscopic approach to solidification modelling, solute redistribution and the resulting microsegregation are calculated on the scale of advancing dendrites based on analytical models. The solute redistribution phenomena can be considered either in the direction of the advancing dendrites, called dendrite tip modelling or within the interdendritic regions, designated to interdendritic or mushy zone modelling (David et al. 1994).

Dendrite tip modelling

The calculations of dendritic or cellular solidification is usually based on two-phase alloy systems for which well-known binary constitution diagrams can be applied as background data. In these cases the growth of a dendrite tip can be modelled with the theory of constrained dendritic growth where the temperature isotherms are moving in the direction of the imposed heat flux. Under these conditions sharp dendrites or cells can grow more quickly than does a flat interface which arises from the more efficient solute redistribution in the surrounding liquid, see Fig. 1.13. It has been demonstrated that the shape of a dendrite tip is closely represented by paraboloid (Kurz et al. 1986). For this type of growth the solutal composition (C_L) in front of an advancing dendrite tip can be expressed as follows (Kurz & Fisher 1992):

$$C_L = \frac{C_0}{1-(1-k)Iv(P)} \tag{10}$$

where k is the equilibrium partition coefficient, C_0 initial liquid composition and Iv(P) Ivantsov's function to a paraboloid dendrite tip:

$$Iv(P) = P \bullet \exp(P)E_1(P) \tag{11}$$

In equation (11) $E_1(P)$ is the exponential integral and P solutal Peclet number that can be determined as follows:

$$E_1(P) \cong -0.577 - \ln(P) + 4P/(P+4) \tag{12}$$

$$P = \frac{r_t R}{2D_L} \tag{13}$$

In equation (13) R refers to dendrite tip velocity, i.e., solidification rate and D_L to the liquid diffusion coefficient.

The dependence between the dendrite tip radius r_t and solidification rate R can be, further, expressed with the following equation:

$$r_t = 2\pi \sqrt{\frac{\Gamma}{\frac{-mR(1-k)C_0}{D[1-(1-k)Iv(P)]} - G}} \tag{14}$$

In the previous equations Γ is the Gibbs-Thomson parameter, m is the liquidus slope and G refers to the mean temperature gradient at the solid liquid interface.

Knowing the solidification rate R and the temperature gradient G, one can solve the dendrite tip radius from equation (14). Subsequently, the Peclet number, the exponential integral and the Ivantsov's function can be solved from equations (11 - 13). Finally, the pile-up composition C_L can be solved from equation (10) and the composition of the solid at the dendrite tip C_s is obtained from the partition ratio k using the relation $C_s = k\ C_L$. The undercooling in front of the dendrite tip can be solved as follows:

$$\Delta T = T_L - T = m(C_0 - C_L) + \frac{2\Gamma}{r_t} \tag{15}$$

In simulation of high solidification rate processes, the above mentioned calculation routine needs a correction with respect to the partition coefficient. This arises from the fact that the equilibrium at the solid/liquid interface is not always maintained with high solidification rates. This happens when the solidification rate begins to approach the diffusion velocity of alloying elements due to which partitioning at the interface becomes inhibited and the partition coefficient k starts to approach unity. This is corrected in the calculations by velocity dependent partition coefficient k´ defined by Aziz (1982):

$$k' = \frac{k + \left(\delta_i R / D\right)}{1 + \left(\delta_i R / D\right)} \tag{16}$$

where k refers to equilibrium partition coefficient, R is the solidification rate, D is the solute diffusion coefficient in the solid-liquid interface and δ_i is the solute trapping distance. δ_i is usually approximated by the interatomic distance, which is between 0.5 and 5 nm for metals (Kurz & Fisher 1992).

Further development of dendrite tip calculations for ternary Fe-15%Ni-15%Cr alloy has been executed by Rappaz et al. (1990). The calculation of ternary alloys is, however, complicated and, therefore, certain simplifying assumptions are made to return the analysis to binary or pseudobinary alloy systems. For example, Elmer (1988) applied pseudobinary constitution diagrams that were in accordance with the solidification paths of the Fe-Cr-Ni alloys studied. Nakao et al. (1993) and Nakao & Nishimoto (1993) carried out calculations in binary Fe-X system, where X refers to alloying element such as Cr or Mo. The parameters needed in the calculations (liquidus slope, interfacial tension, the latent heat and the partition coefficient) were chosen from ternary equilibrium. They used this approach in evaluating the corrosion resistance of laser surface remelted zones. In their calculations the compositional enrichment of the dendrite cores with increasing

the solidification rate could be clearly demonstrated. A fairly good fit between simulations and experiments was observed.

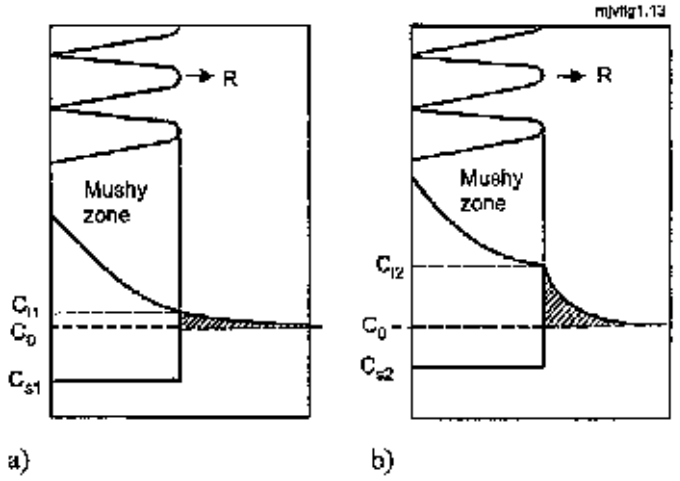

Fig. 1.13. Solute pile-up formed at a slow (a) and high (b) solidification rate (Miettinen 1992).

Miettinen (1992) has further studied the theory of constrained dendrite tip growth by developing a thermodynamic solution model. In the present version of this model, designated CDGMS[1], the stability of the leading phase of solidification can be determined for multicomponent steels by using chemical potential equality equations to determine the thermodynamic equilibrium at the phase interfaces. Deviations from local equilibrium are taken into account by including interface friction, capillarity and solute drag effects typical of high solidification rates. The CDGMS-model is applicable in solidification modelling of stainless steel alloys where the demarcation between primary austenitic and primary ferritic solidification can be demonstrated as a function of solidification rate.

Interdendritic solidification modelling

The interdendritic segregation of a binary alloy is calculated in a volume element solidifying normal to the direction of a dendrite or cell tip. In the case of cellular solidification the volume element shown in Fig. 1.14a is generally applied. Solute redistribution is calculated in one direction, i.e., normal to the growing dendrites. For cellular-dendritic or dendritic morphology the calculations in two dimensions are carried out according to Fig. 1.14b. For both cases the solute redistribution behaviour is usually based on an assumption of compositional equilibrium at the solid-liquid interface during solidification. For simplicity the models also

[1] CDGMS: Solidification analysis package for constrained dendritic growth of multicomponent steels (Miettinen 1998).

generally assume complete mixing in the liquid and no mass flow into or out of the volume cell that is defined for calculations.

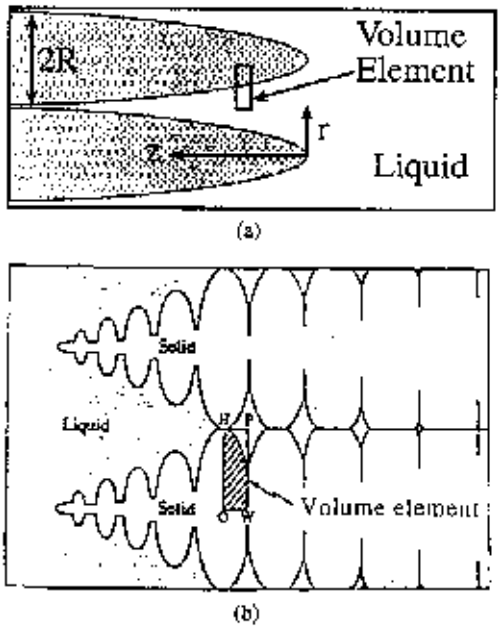

Fig. 1.14. Schematic representation on calculation of solute redistribution in a volume element defined for intercellular (a) and interdendritic (b) solidification (Brooks & Baskes 1986, Matsuda et al. 1991).

Depending on the amount of compositional changes caused by diffusion in a solid, different assumptions for the solute redistribution have been applied in modelling. The basic equation, designated as the Scheil equation or non-equilibrium lever rule (Scheil 1942) assumes no diffusion in the solid and complete diffusion and convection in liquid, is given by the following formula:

$$C_s = kC_0(1-f_s)^{k-1} \tag{17}$$

where k refers to the equilibrium partition coefficient, C_0 to the initial alloy composition and f_s to the fraction of solidified metal. Since the model does not allow homogenising diffusion in the solid state, it leads to an error in cases of high diffusion rates of alloying elements after solidification. The Scheil equation can still be used with reasonable accuracy when back diffusion in solid is slow, as in the case in primary austenitic solidification of stainless steels and Ni-base alloys (Fredriksson 1976, DuPont 1996). In more accurate calculations the effect of homogenising back diffusion in the solid phase is usually taken into account by various improvements to the Scheil equation (Brody & Flemings 1966, Clyne & Kurz 1981). Brody and Flemings have modified the equation as follows:

$$C_s = kC_0\left[1-\frac{f_s}{1+\alpha k}\right]^{k-1} \qquad (18)$$

In this equation $\alpha = D_s t_f / (d/2)^2$ where D_s is the diffusion coefficient of the solid state, t_f is the local solidification time and d/2 is the length of a volume element, i.e., half of the dendrite primary spacing. Introducing solid state diffusion, equation (18), gives a more accurate prediction to the composition of the solid. With a significant amount of solid state diffusion the Brody & Flemings model becomes inaccurate. A further development has been carried out by Clyne & Kurz (1981) by taking into account the magnitude of back diffusion as follows:

$$C_S = kC_0\left[1-f_S(1-2\Omega k)\right]^{(k-1)/1-2\Omega k)} \qquad (19)$$

where Ω refers to a back diffusion parameter describing the magnitude of diffusion and, thus, homogenisation rate in the solidified dendrite cores:

$$\Omega = \alpha\left[1-\exp\left(-\frac{1}{\alpha}\right)\right]-½\exp-\frac{1}{2\alpha} \qquad (20)$$

The back diffusion parameter can have values between 0 to 0.5. With Ω = 0 no back diffusion exists and equation (19) reduces to the Scheil equation and with Ω = 0.5 the equilibrium lever rule is obtained.

Further development of the solute redistribution theory has been carried out by Sarreal & Abbaschian (1986) by introducing the effect of dendrite tip undercooling and eutectic temperature depression to the solidification analysis of Al-Si alloys. Ohnaka (1986) has proposed solidification models for plate and columnar dendrites by assuming complete mixing in the liquid and parabolic dendrite growth. Kobayashi (1988) has developed exact analytical solutions for plate and columnar dendritic models. All of these models give predictions to the solute redistribution that are intermediate with respect to Scheil equation and the equilibrium lever rule.

The above stated models were originally developed for analysis of binary alloys. Their applications to ternary and even more complicated alloy systems is, thus, questionable, especially without experimental verification. Miettinen (1992) and Koseki et al. (1994) have approached the problem by developing more sophisticated models that take into account thermodynamic equilibrium in multicomponent alloy systems. The models are based on assumptions of thermodynamic equilibriums at the solid/liquid and ferrite/austenite interfaces and complete solute mixing in the liquid. Kinetic calculations are performed by the finite difference method (FDM) combined with thermodynamic calculations using a thermodynamic database such as Thermocalc™ by Koseki et al. (1994) and a thermophysical database by Miettinen (1992, 1995a, b, c). As a result from linking the calculations to these databases, both models have demonstrated reasonably accurate predictions for solute redistribution of multicomponent alloys, provided

that solidification is close to equilibrium. The interdendritic solidification model (IDS) of Miettinen (1992) has been successfully applied in continuous casting and the model of Koseki et al. (1994) in GTA-welding.

1.5 Objectives of the investigation

The development of macroscopic and microscopic models to achieve better understanding in weld pool phenomena and welding metallurgy has been intensive in the 80's and especially in the 90's. Most of the developed models concentrate on either macroscopic or microscopic weld phenomena without considering any wide-ranging linking between each other. This type of linking would, however, give useful information on the effects of welding parameters and solidification conditions to weld microstructures and properties. A typical example is the modelling of weld pool phenomena and resulting pitting corrosion resistance. This has not been widely studied before. The aim of this thesis is to address to this need.

In the present investigation various modelling techniques are applied in order to link weld solidification behaviour to weld metal properties, especially to pitting corrosion resistance in welding of austenitic stainless steels. The main objective is to demonstrate the effect of solidification parameters, i.e., solidification rate, temperature gradient and cooling rate on solute redistribution and the resulting pitting corrosion resistance of austenitic stainless steel welds by applying computer aided modelling.

Objectives of this thesis can be divided into subtasks as shown in Fig. 1.15. The first task of the study is to apply macroscale modelling for predicting the weld shape and the solidification parameters prevailing in the solidifying weld pool. In the next step, this data is coupled to microscale modelling for calculating solute redistribution of the welds using dendrite tip and interdendritic solidification modelling. The solute redistribution data is then used in evaluation of the pitting corrosion resistance of welds.

In addition to the coupled macro-micro modelling a number of microscopic solidification models are used separately for comparison and to demonstrate the effect of welding speed on weld microsegregation and pitting corrosion resistance.

For verification of the calculations, experimental investigations consisting of welding tests, measurement and calculation of solidification parameters, microstructural investigations, measurement of microsegregation and pitting corrosion tests are performed.

The industrial benefits expected from the results include the optimisation of weld metal microstructures for high corrosion resistance with reduced need for extensive laboratory work. The results are also expected to reduce the need of post-weld heat treatments and associated costs to improve weld metal corrosion properties. The study, further, provides information on avoidance of hot cracking in welding with high welding speeds where the change in solidification mode may

cause an increase in cracking susceptibility. Development of steels and welding procedures in terms of better corrosion and cracking resistance is also expected as an industrial benefit.

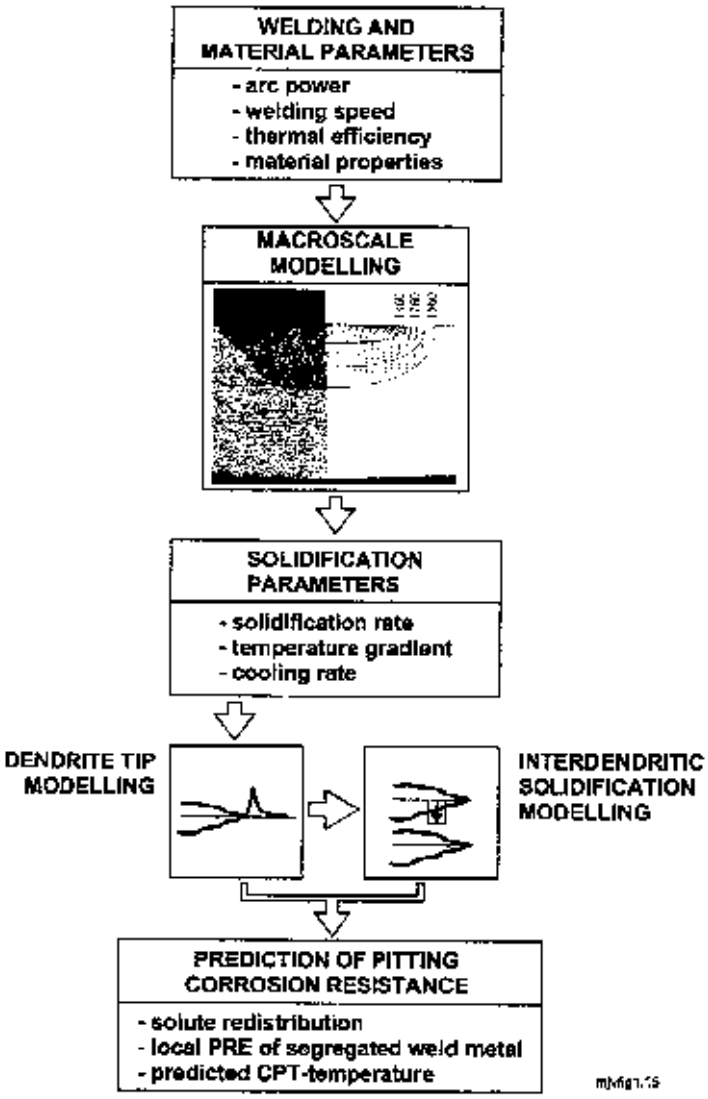

Fig. 1.15. Objectives and tasks of the investigation.

2. Experimental and analytical procedures

The experimental part of the investigation included welding tests of the steels studied, identification of weld microstructures, measurements of segregation profiles and pitting corrosion tests. This data was used as background and verification data for the applied models.

2.1 Materials and welding experiments

For conducting the welding experiments laboratory heats of AISI 301, 304, 316 and 6% Mo-alloyed austenitic stainless steel grades were manufactured by Outokumpu Polarit Oy using their vacuum induction furnace. After casting at 1530°C the billets having thickness of 50 mm were machined to 48 mm, annealed 1 h at 1250°C and hot rolled to thickness of 5.5 mm. After rolling the plates were annealed for 5 min at 1100°C, air cooled, pickled, washed and mechanically cut to test samples 250 mm in length and 100 mm in width.

The compositions of the steels are given in Table 2.1. Analyses of the steels studied were adjusted so that the Cr_{eq}/Ni_{eq} ratio of Hammar & Svensson (1979) ranged from 1.05 to 2.07. Accordingly, using the designations of Table 2.1, the solidification mode of conventional arc welds of the steels is supposed to be fully austenitic for 6Mo/3 grade, primary austenitic for 6Mo/1, 6Mo/2, 304/2 and 316/3 grades, primary ferritic for 304/1, 316/1 and 316/2 grades and fully ferritic for 301 grade (Fig. 1.6).

The welding experiments were carried out by GTAW- and CO_2-laser processes. The GTAW-tests were conducted autogenously, i.e., without filler wire using mechanised welding. The test plates were attached to a fixture and welded using a constant welding current of 150 A. The arc length was adjusted to 2 mm which resulted in arc voltage of 10 ± 1 V, that was documented for each welding tests from the voltage meter of the power source. The welding tests were carried out in two phases: (1) applying a systematic variation of welding speed between 100 and 800 mm/min (Table 2.2a) and (2) using a constant welding speed with variable nitrogen alloyed shielding gases (Table 2.2b). The purpose of the tests in phase (2) was to demonstrate the effect of nitrogen alloying on weld pitting corrosion resistance and to compare the efficiency of nitrogen alloying to that of high-speed welding. In most welding experiments the cooling curves were documented by immersing Pt/Rh thermocouples into the weld pool during welding and by documenting the cooling cycle by a datalogger.

The laser welding experiments were carried out by the CO_2-laser unit of Lappeenranta University of Technology (Rofin-Sinar RS6000, nominal power 6 kW). The welding speed was systematically varied from 1000 to 5000 mm/min with constant power of 3.2 kW at the specimen surface, see Table 2.3. The welds were produced using melt-in technique with a partial penetration into the base plates. The purpose of the tests was systematically to increase the solidification and cooling rates of the melt-in welds studied. All the welding parameters

including focus distance, nozzle dimensions as well as shielding and plasma gases are given in Table 2.3.

Table 2.1. Compositions of the studied steels.

Steel type	**UNS S30100**	**UNS S30400**		**UNS S31600**			**UNS S31254**		
Designation[1]	**301**	**304/1**	**304/2**	**316/1**	**316/2**	**316/3**	**6Mo/1**	**6Mo/2**	**6Mo/3**
C	0.039	0.027	0.036	0.023	0.024	0.024	0.008	0.013	0.010
Si	0.45	0.49	0.48	0.50	0.51	0.49	0.35	0.38	0.32
Mn	1.45	1.53	1.51	1.47	1.47	1.47	0.46	0.49	1.33
P	0.006	0.008	0.004	0.016	0.017	0.018	0.023	0.024	0.014
S	0.006	0.005	0.005	0.004	0.004	0.004	<0.001	<0.001	0.002
Cr	16.9	18.5	18.5	16.9	16.8	16.9	20.1	19.9	20.8
Ni	6.5	8.9	11.4	10.4	11.4	12.9	18.1	21.5	24.4
Mo	<0.01	<0.01	<0.01	2.88	2.85	2.87	6.12	6.20	6.40
Cu	<0.01	<0.01	<0.01	0.13	0.13	0.13	0.81	0.76	0.82
Al	0.024	0.012	0.014	0.024	0.019	0.016	0.013	0.032	0.17
O_2	0.0105	0.0100	0.0080	0.0130	0.0120	0.0070	0.0031	0.0110	-
N_2	0.04	0.048	0.043	0.054	0.052	0.054	0.198	0.184	0.210
Cr_{eq} [2]	17.6	19.2	19.2	21.6	21.5	21.6	29.0	29.0	30.2
Ni_{eq} [3]	8.5	10.6	13.3	12.3	13.3	14.8	22.0	25.3	28.8
Cr_{eq}/Ni_{eq}	2.07	1.81	1.44	1.76	1.62	1.46	1.32	1.14	1.05
PRE [4]	17.5	19.1	19.1	27.1	26.9	27.1	42.9	42.8	44.7

[1] This designation is used later in the text.
[2] Cr_{eq} = Cr + 1.37 Mo + 1.5 Si + 2 Nb + 3 Ti
[3] Ni_{eq} = Ni + 0.31Mn + 22 C + 14.2 N + Cu
[4] PRE = Cr + 3.3 Mo + 13 N

Table 2.2. Welding parameters for GTAW-tests. a) Tests with varying the welding speed. Shielding and root gas: Ar (99.998%). Flow rates 12 l/min for shielding and 6 l/min for root gas. The arc length was 2 mm.

Welding speed (mm/min)	**Current (A)**	**Voltage (V)**	**Arc power (kW)**	**Welding energy (kJ/mm)**
100	150	9.3 - 11.2	1.40 - 1.77	0.82 - 0.97
200				0.44 - 0.50
400				0.20 - 0.23
800				0.11 - 0.12

Table 2.2 continues. b) Tests for steel 6Mo/3 with variable nitrogen content of the shielding gas.

Shielding gas[1]	Current (A)	Voltage (V)	Welding speed (mm/min)	Arc power (kW)	Welding energy (kJ/mm)
Ar Ar + 2.7% N_2 Ar + 5.2% N_2 Ar + 10.5% N_2	210	10.3 - 11.0	200	2.1 - 2.3	0.65 - 0.69

[1] root gas: Ar (99.998%)

Table 2.3. Welding parameters for CO_2-laser welding tests.

Constants Output power 4.0 kW, beam power to specimen 3.2 kW Focus distance 150 mm, beam focused at plate surface Nozzle ∅ 6.5 mm, working distance 10 mm Shielding gas: He 10 l/min Plasma gas: He 30 l/min	
Welding speed (mm/min)	**Welding energy (kJ/mm)**
1000	0.192
1500	0.128
2000	0.096
3000	0.064
4000	0.048
5000	0.038

2.2 Weld nitrogen content

Nitrogen content of some representative welds was determined using a gas-analyser based on thermal conductivity. Two analyses from each weld studied were taken and the results were given as averages of these measurements.

In the low-speed GTA-welds the weld volume was large enough to prepare and analyse all-weld-metal samples taken directly from the test joints. In samples cut from the high-speed welds the volume of the fused metal was, however, too small to extract an all-weld-metal sample. In these cases the nitrogen content was first analysed from samples containing both weld and base metal portions. The nitrogen content of the weld metals was then calculated from the measurements taking into account the volume fractions of weld and base metals. The volume fractions were determined before the analysis by measuring the length of the samples and the dimensions of the weld cross-sections by a light microscope. The weld nitrogen content N_{weld} was then calculated from the following dependency:

$$N_{weld} = (N_{meas} - f_{bm} \bullet N_{bm}) / f_{weld} \quad (21)$$

where N_{meas} is the nitrogen content analysed from each sample, N_{bm} is the base metal nitrogen content and f_{weld} and f_{bm} are the volume fractions of weld and base metal in the sample, respectively.

2.3 Microscopy and microanalyses

2.3.1 Optical microscopy

For microstructural characterisation of the weld metals, cross- and longitudinal sections were cut from the test welds. The samples were ground to 1200 grit, mechanically polished and electrochemically etched (3–5 V, 3–10 s) in a solution of 200 ml methanol and 40 ml HNO_3 at -30°C. The solidification mode and characteristic microstructures of the test welds were then studied by an optical microscope and photographed. After these examinations the dendrite arm spacing of the welds showing primary austenitic solidification was measured from the longitudinal sections. Measurements were taken midway between the weld centerline and the fusion line. The angle (θ) between the welding direction and the direction of solidification was measured from same positions. Grain growth to opposite direction with respect to welding (i.e. negative values of θ) present in some welds was, however, excluded from the analyses. Results were expressed as mean values of ten measurements.

To determine the ferrite contents electrochemical etching in 40 g NaOH - 100 ml H_2O -solution (2.5 V, 2–10 s) was applied for the weld samples. The ferrite content was measured by using an optical image analysator (Kontron IBAS 2.5) with magnifications of 550X or 1100X, depending on fineness of the microstructure. The ferrite contents were expressed as average of ten measurements from each weld metal. For reference, the ferrite contents of the low-speed GTA-welds were measured also by Ferritscope meter[2] that was calibrated according to standard ISO 8249. The ferrite contents were obtained directly in percentages that were automatically converted from ferrite numbers (FN) by the measuring device. Ten Ferritscope measurements were taken from each weld studied.

2.3.2 Microanalysis and electron microscopy

Electron probe microanalysis

For studying the microsegregation of the test welds, microanalyses were made by using an electron probe microanalyser (EPMA) with acceleration voltage of 15 kV and beam diameter of 1 µm. The welds subjected to the analysis were GTA-welds (Table 2.2) with welding speed of 100 mm/min and laser welds (Table 2.3) with

[2] To avoid error caused by decrease in weld cross-section area Ferritscope measurements were conducted only for low-speed GTA-welds (100 mm/min)

1000 and 5000 mm/min. The concentration profiles for Cr, Ni and Mo were determined by the step scanning technique. The length of steps between the measurements was 2 µm and the number of scanning points was 40, i.e., the length of the analysis lines was 80 µm. In every analysed test weld the previous procedure was carried out in three positions at the weld surface macrosection: at the weld centerline, at midway between the weld centerline and fusion line and at the weld metal close to the fusion line.

For reference the magnitude of microsegregation in the 6% Mo alloyed superaustenitic welds was investigated also by a computer aided microprobe analysis method (CMA) in collaboration with Nippon Steel Co. The measurement device was a computer controlled EPMA-microanalyser capable of 2-dimensional analysis measurement. A 350×350 µm square located midway between the weld centerline and fusion line was analysed from the weld metal specimens with an accelerating voltage of 15 kV and beam current of 2 mA. The diameter of the measuring beam was 1 µm. By this means the distribution of Cr, Ni and Mo could be measured from the weld surface sections in two dimensions.

The distribution of N in the 6% Mo alloyed weld metals was further analysed by ARL-SEMQ microsond analyser (EPMA) at the Institute of Metals Research in Stockholm. In these measurements the concentration of N was measured at dendrite cores as well as at interdendritic regions of the 6% Mo alloyed weld metals using specimens welded according to Table 2.2b with pure Ar and Ar plus 10.5% N_2 shielding gases. The spot analysing technique with 10 - 15 successive measurements was used. The analysing time of the spot analysis was 40 s which has been demonstrated to give good stability and counting statistics (Runnsjö 1981). Acceleration voltage of 10 kV, beam current of 150 nA and spot diameter of 1 µm were used in the measurements.

Electron microscopy

Microstructures of the 6% Mo type superaustenitic test welds were first studied by scanning electron microcope applying backscattering electron image technique. The samples for these investigations were prepared by grinding (1200 grit) and mechanically polishing. The purpose of these investigations was to confirm the possible presence of intermetallic phases in the 6% Mo alloyed steel welds before subjecting the specimens to transmission electron microscopy. The amount of intermetallic phases was measured from the backscattering images by an optical image analysator (Kontron IBAS 2.5) connected to the scanning electron microscope. The results were expressed as averages of 5 measurements from each weld studied.

Transmission electron microscopy was used in studying microsegregation and identification of microstructures and phases present in low-speed GTA-welds (welding speed 100 mm/min) and high-speed laser welds (5000 mm/min) of steels 316/1 and 6Mo/1. Samples for this purpose were cut using a diamond saw parallel to the weld surface and thinned by electropolishing using a modified window method at low temperature. These thin foil samples were examined using a Philips

CM 200 FEG-STEM microscope operating at 200 kV. Elemental analyses from different phases were taken applying beam diameter of 5 nm using a Noran Voyager (thin window detector) EDS-analyser.

2.4 Pitting corrosion tests

Pitting corrosion behaviour of steels AISI 301, 304 and 316 and their test welds were investigated by potentiodynamic scan method in an Avesta Cell (Quarfort & Alfonsson 1989). In these tests an area of 1 cm^2, located either across welded joint or in base metal, was subjected to testing. Two samples for each test weld were studied using 3.56% NaCl solution (34 g NaCl + 920 ml H_2O) at 23°C. The weld surface sections were ground to 600 grit. In the measurements the potential was constantly raised using a scan speed of 20 mV/min by recording the current. The breakdown potential E_b (mV) indicating pitting corrosion was documented corresponding to the current density of 10 $\mu A/cm^2$.

Pitting corrosion properties of the test welds were studied also by immersion tests according to standard ASTM G48 in 10% $FeCl_3$ solution (166.1 g $FeCl_3 \bullet 6H_2O$ to 1000 ml H_2O). Test samples were machined from the test joints having a length of 25 mm (parallel to welds) and a width of 50 mm. The welds were located in the middle of the samples. The weld beads were ground to base plate level with emery paper (120 grit) and sharp edges present in the specimens were rounded by grinding.

The $FeCl_3$ tests were started at +5°C using immersion time of 24 h. Subsequent washing of the specimens with water and ethanol was followed by air drying and visual inspection using a stereomicroscope. The temperature of the solution was increased stepwise in 5°C increments and the 24 hour testing cycle was repeated as long as initiation of pits was observed. The appearance of pits either at cross-section or at surface section face of the samples was documented separately. The lowest test temperature with a visible indication of pitting corrosion was documented as a critical pitting temperature (CPT) for these two sample locations.

To reveal typical location of corrosion pits with respect to weld microstructure, a series of immersion tests applying a shorter immersion time (5 h) was carried out. The test temperature was selected slightly above the CPT-temperatures of the welds that were first determined as specified above. After the tests the samples were inspected by a stereomicroscope. The samples were then etched lightly with 30% HCl - 10% HNO_3 - glycerin mixture and the location of the pits with respect to the weld microstructure was surveyed with scanning electron microscope (SEM).

2.5 Modelling

The modelling investigations were carried out in two parts. In the first stage, macroscopic simulations were carried out to predict the weld pool behaviour, fusion zone shape and solidification parameters. The second stage comprised of microscopic modelling that was applied estimating microsegregation and

predicting pitting corrosion resistance of the welds studied. A link between the macroscopic and microscopic simulations was established by using the calculated solidification parameters as input data for microscopic modelling.

2.5.1 Macroscopic simulations

The macroscopic simulations were carried out by the WELD3D program described by Mundra et al. (1996). The program is based on the control-volume method and calculates heat transfer and fluid flow of welds generated by a moving heat source. The simulations were carried out for 3-dimensional steady state flow using a coordinate system attached to the moving electrode. Because of joint symmetry, only one half of the butt weld was modelled. The parameters of the simulations are summarised in Appendix 1.

In the first series of simulations the weld pool shape of autogenous GTA-welds of steel 304/2 were calculated for welding speeds of 100 and 200 mm/min and compared with experiments. The simulations were continued by varying the welding speed and the sulphur content of the simulated weld pools. The object of these variations was to demonstrate the effect of welding speed (100 and 400 mm/min) and sulphur content (20 and 150 ppm) on weld pool shape and solidification parameters at the weld surface.

Appendix 1 (Table A1.2) summarises the boundary conditions for the simulations. Heat distribution from the heat source was assumed to be Gaussian. The thermal efficiency factor of GTA-welding was chosen to $\eta = 0.75$ (Smartt 1990). Material data used in the simulations is shown in Appendix 1 (Table A1.3 and Figs A1.1 - A1.3).

The calculated weld shapes parallel to the cross- and surface sections were compared to those of corresponding welding experiments. The pool shape parallel to the surface section was used in calculation of the solidification parameters prevailing at the weld pool surface. The temperature gradient (G) was first obtained by using the temperature difference of two isotherms located side by side in solid in the close vicinity of the solid-liquid interface. For calculation of the solidification rate (R) the normal of the solidification front was first determined by piecewise linear interpolation. The solidification rate (R) was then calculated by using equation (2), assuming angle $(\theta-\phi)$ equal to zero, i.e., the grain growth takes place normal to the solidification front. The cooling rate (GR) was then obtained as a product of the temperature gradient and solidification rate. Finally, the values of G, R and GR were summarised as a function of distance from the weld centerline.

2.5.2 Microscopic simulations

The aim of the micro-scale modelling was to evaluate the effect of weld solidification parameters on segregation and pitting corrosion resistance of the studied welds. Both dendrite tip and interdendritic solidification models were used in these calculations.

Tip modelling

The segregation of Cr, Ni and Mo in front of an advancing dendrite tip was calculated by the model proposed by Kurz et al. (1986) that was available for the purpose as a PC-program (Nishimoto 1995). In the model the composition at the dendrite tip (C_s) was calculated as a function of weld solidification rate based on the procedure described in Appendix 2. The partition coefficients of Cr, Ni and Mo needed in the calculations were first obtained for the present steels from the Thermocalc™ database. In the computer program the other parameters needed in the calculations (liquidus slope, interfacial tension, latent heat) are based on the ternary Fe-Cr-Ni alloy system.

The calculations were carried out for steels showing primary austenitic solidification. In this case the composition of the dendrite tip closely corresponds to that of the dendrite cores, arising from slow diffusion rates of alloying elements in austenite. The pitting corrosion resistance of the dendrite cores could, thus, be evaluated from the calculated tip compositions.

The input values of the calculations, i.e., solidification rate R and the temperature gradient G, that are needed in solving the dendrite tip radius (Appendix 2) were taken from the results of the macroscopic simulations for different weld locations. In the second stage of the simulations the values of R and G were constantly increased based on the values of these parameters which were obtained from microstructural measurements. The purpose of these simulations was to demonstrate the effect of increasing welding speed on segregation behaviour in the direction of growing dendrites or cells.

The pile-up and dendrite tip compositions were calculated also by the CDGMS-model of Miettinen (1992, 1998), see Appendix 3. Since the model is based on chemical potential equality equations of multicomponent alloys, it could be applied in the simulation of both primary austenitic and primary ferritic solidification modes. Consequently, the primary phase of solidification as a function of solidification rate could be simulated for the steels studied. The calculations were carried out in a similar way as described above, i.e., by constantly increasing the average values of solidification rate and temperature gradient based on experimental measurements from the test welds.

Interdendritic solidification modelling

The solute redistribution of welds showing primary austenitic solidification was simulated in the interdendritic direction by the computer program of Nishimoto (1995). The program is based on the solidification models of Ohnaka (1986), Brody & Flemings (1966) (modified by Clyne & Kurz (1981)) and Giovanola & Kurz (1990), see Appendix 4. The models calculate interdendritic segregation in an element shown in Fig. 1.14a as a function of fraction of solidified metal f_s. Input data for the interdendritic calculations were taken from the dendrite tip model described above (later designated to TIP-ID modelling). For comparison, solute redistribution without linking to the tip model was also applied. In this case the equilibrium partition coefficient determined by Thermocalc^{TM} database was used to calculate the initial solid composition.

The solute redistribution of the GTA-welds was simulated also by the model developed by Nippon Steel Co. (Koseki et al. 1994). The purpose of these simulations was to compare solute redistribution between primary austenitic and ferritic welds including not only solidification but also solid state transformations.
In the NSC-model the computation takes place in a hexagonal cell shown in Appendix 5 (Fig. A5.1). The cell was divided to ten finite segments where solute diffusion across the segments was computed by the finite difference method (FDM). Thermodynamic equilibrium at each interphase was simultaneously updated by the Thermocalc™ database, see Appendix 5 (Fig. A5.2). After solidification the solid state transformations within each FDM-segment were calculated using a Clyne-Kurz type analysis by assuming complete mixing of elements in δ-ferrite and limited back-diffusion of elements in austenite (equations 19 and 20).

3. Results of experimental investigations and modelling

3.1 Solidification parameters

Solidification parameters, i.e., the weld cooling rate, solidification rate and temperature gradient were determined based on thermocouple and microstructural measurements. Cooling rate was evaluated by analytical calculations for the reference data. The main aim of these measurements was to achieve a reliable background data for modelling.

3.1.1 Cooling rate

Results of the thermocouple measurements obtained from the GTA-welds are summarised as a function of welding energy in Figs 3.1 and 3.2. The measured cooling rates (Fig. 3.1) and cooling times between 1200°C and 800°C (Fig. 3.2) are compared to calculated values obtained from analytical heat conduction equations specified in Appendix 6. Results show that the cooling rate at 1425°C decreases from about 2000°C/s to 100-200°C/s as the welding energy increases from about 0.1 kJ/mm (welding speed 800 mm/min) to 1 kJ/mm (welding speed 100 mm/min). Correspondingly, the weld cooling time $t_{12/8}$ increases from about 0.3 s to 10 s. There exists a reasonable compatibility between the measured and calculated cooling rates and cooling times. The effect of thermal efficiency factor, that was varied between 0.5 and 1.0, has also been demonstrated by the calculations. It is noteworthy that the measurements indicate a transition from 3-dimensional to 2-dimensional cooling with decreasing welding energy, i.e., with increasing the welding speed. This is noticed from the trend of the measurements to follow 3D-curves in lower welding energy range and 2D-curves at the highest welding energies used.

The weld cooling rate of the GTA- and laser welds was estimated also from the primary and secondary dendrite/cell arm spacing measurements. This was achieved by first correlating welding speed and spacing, see Fig. 3.3. Results show a reasonable correlation although there exists also scatter among the steels and welds studied. Cooling rates were then calculated from the average spacings obtained from Fig. 3.3 using the empirical relationship of Katayama & Matsunawa (1984)[3], see Fig 3.4. Good compatibility between measurements and calculations can be noticed. The cooling rate values are close to 100 K/s in welds of the lowest travel speed of 100 mm/min and increase close to 10 000 K/s when increasing the welding speed up to 5000 mm/min.

[3] Primary spacing $d_1 = 80(GR)^{-0.33}$, secondary spacing $d_2 = 25(GR)^{-0.28}$.

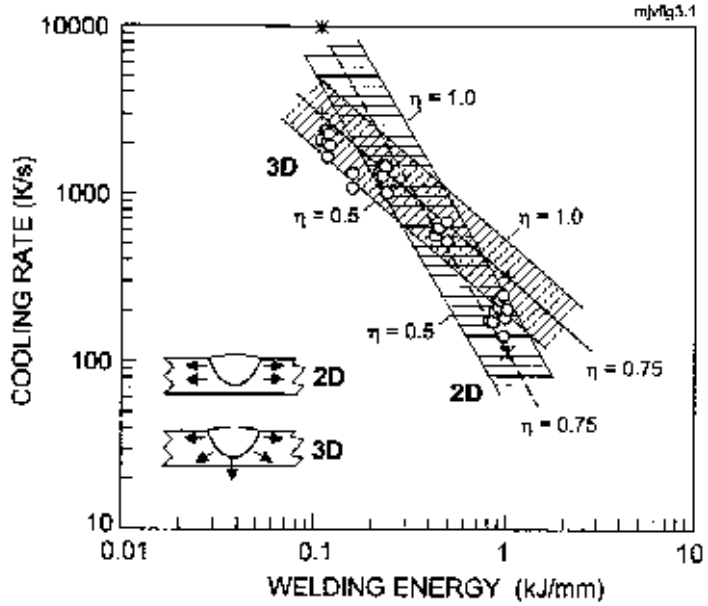

Fig. 3.1. Weld cooling rates at 1425℃ measured by thermocouples and calculated by conductive heat conduction equations (Appendix 6). The scatterbands show the calculated cooling rates for thermal efficiency factors ranging from 0.5 to 1.0.

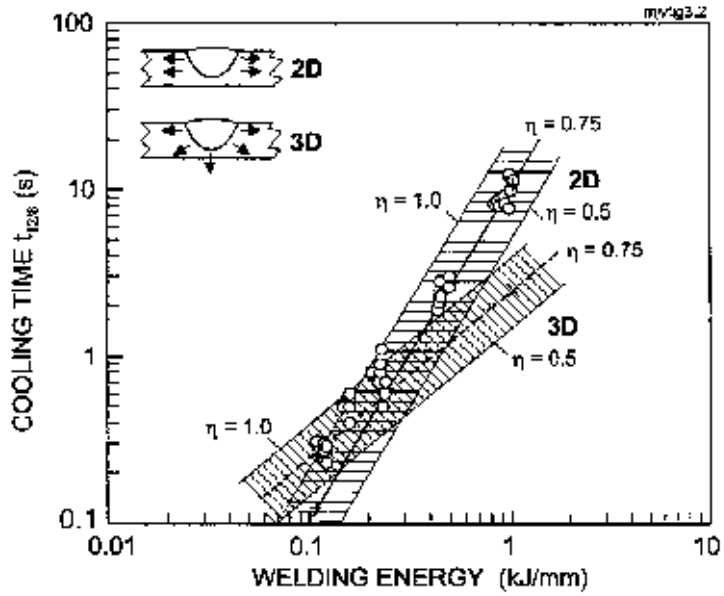

Fig. 3.2. Weld cooling time between 1200℃ and 800℃ ($t_{12/8}$) measured by thermocouples and calculated by conductive heat conduction equations (Appendix 6). The scatterbands show the calculated cooling times for thermal efficiency factors ranging from 0.5 to 1.0.

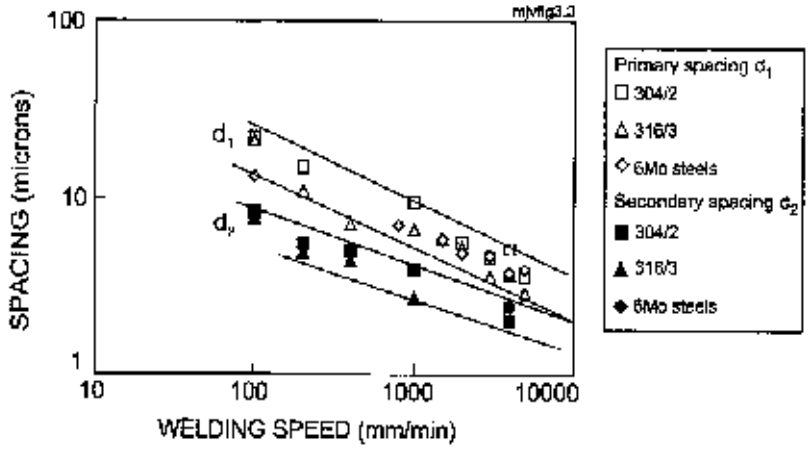

Fig. 3.3. Measured primary (d_1) and secondary (d_2) dendrite arm spacings of the test welds as a function of welding speed. The individual results are averages of 5 - 10 measurements taken from welds showing primary austenitic solidification.

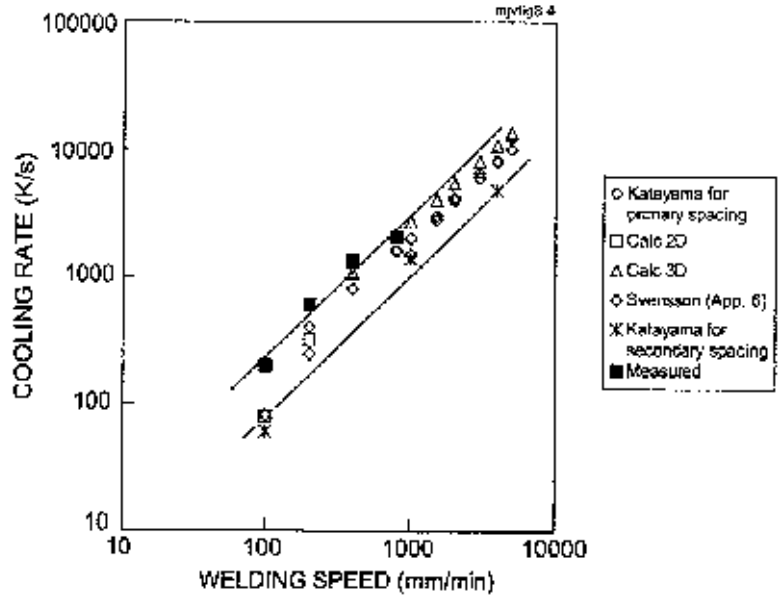

Fig. 3.4. The cooling rates of the test welds calculated from primary and secondary dendrite arm spacing measurements by using the relationships of Katayama & Matsunawa (1984) and comparison of the results to calculations (Appendix 6) and thermocouple measurements.

3.1.2 Solidification rate

The values of the θ-angle measured between the welding direction and the direction of grain growth are summarised in Fig. 3.5. Measurement results are taken from weld metal areas located midway between weld centerline and fusion line and are expressed as averages of 10 measurements for all the welds showing primary austenitic solidification. Measurements show that with low welding speeds where an elliptical weld pool prevails, the θ-angle increases slightly with increasing the welding speed. With welding speeds in excess of about 2000 mm/min the θ-angle remains nearly independent of the welding speed. In these cases the weld pool geometry is an elongated tear drop in which the θ-angle remains almost constant towards the weld centerline irrespective of welding speed.

The θ-angles can further be used for estimating typical solidification rates using equation (2). In these calculations the angle θ-ϕ defined in Fig. 1.3 is assumed to zero. In other words, solidification is assumed to take place normal to the solidification front. Figure 3.6 summarises the mean solidification rates obtained as a function of welding speed. The increase of the welding speed from 100 mm/min to 5000 mm/min (i.e. from 1.7 mm/s to 83 mm/s) increases the solidification rate from about 0.5 - 1 mm/s up to 10 - 15 mm/s. These values agree well with the results presented by Suutala (1981) and Elmer (1988).

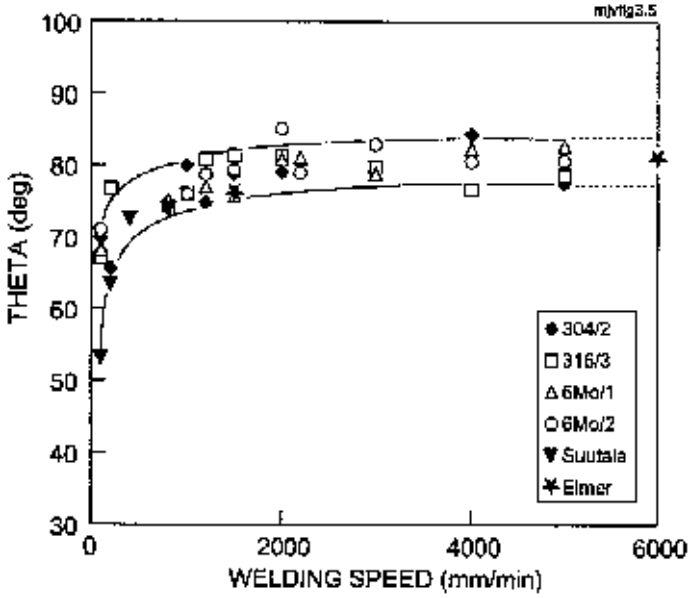

Fig. 3.5. Mean values of angle θ measured at midway between the weld centerline and fusion line and comparison of the results to other studies (Suutala 1981, Elmer 1988).

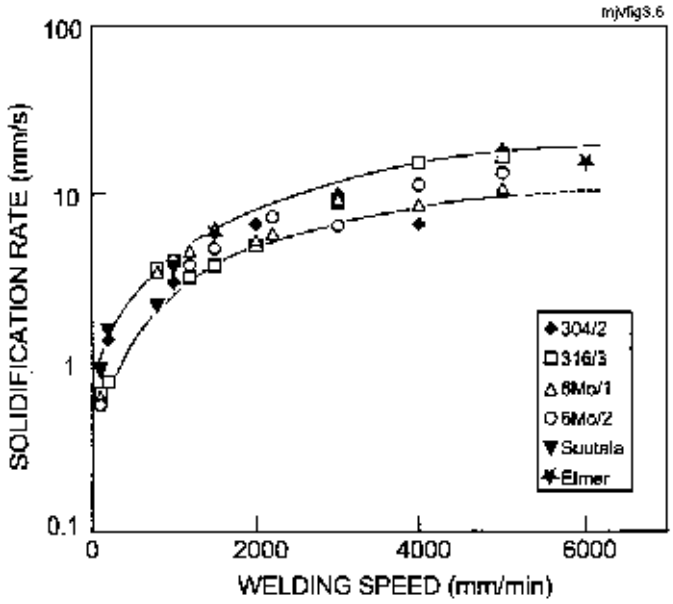

Fig. 3.6. Mean values for solidification rates at midway between weld centerline and fusion line. The values are based on the measured θ-angles (Fig. 3.5) and equation (2) assuming that solidification proceeds normal to the solidification front. The results are compared to those presented by Suutala (1981) and Elmer (1988).

3.1.3 Temperature gradient

The estimates for the temperature gradient (G) prevailing during weld solidification can be derived by dividing the cooling rate GR (Fig. 3.4) by the corresponding solidification rate R (Fig. 3.6). The results for weld area locating midway between weld centerline and fusion line are shown in Fig. 3.7. As expected, the temperature gradient shows an increasing trend with increasing the welding speed. With lowest welding speed of 100 mm/min the temperature gradient is close to the level of 100 K/mm. When increasing the welding speed up to 5000 mm/min the temperature gradient increases by one order of magnitude to about 1000 K/mm. The results, however, show a considerable amount of scatter, arising from local variations in dendrite arm spacing and solidification rates. The estimated values are still of the same order of magnitude as those presented Elmer (1988) as a function of welding speed. The results obtained for low-speed GTA-welding agree reasonably well also with the values gathered from available literature to Table 1.1.

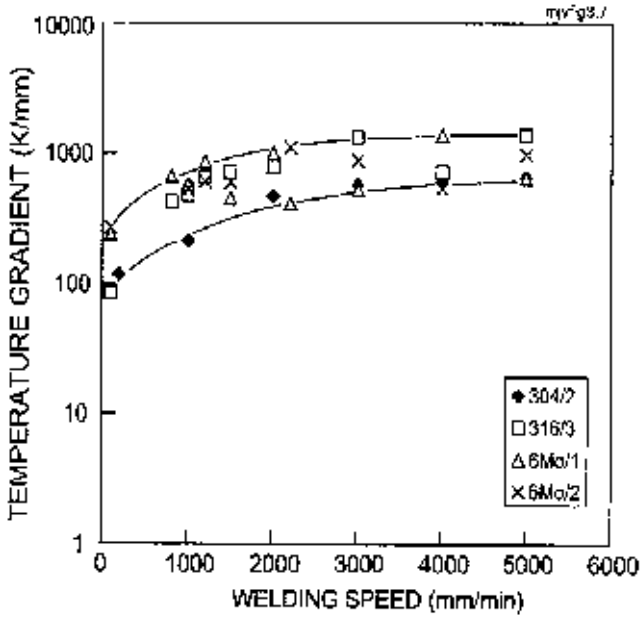

Fig. 3.7. Estimates for temperature gradient at midway between the weld centerline and fusion line determined from the cooling rates of Fig. 3.4 and solidification rates of Fig. 3.6 .

3.2 Microstructures of test welds

According to the solidification behaviour classified earlier by Suutala & Moisio (1980) the microstructures of the test welds could be classified in three groups:

- welds solidifying in primary or fully ferritic mode
- welds changing their solidification mode from primary ferritic to primary austenitic with increasing the welding speed
- welds solidifying in primary or fully austenitic mode.

3.2.1 Primary and fully ferritic solidification

The steels having the highest Cr_{eq}/Ni_{eq} ratios showed primary or fully ferritic solidification with typical features shown in Fig. 3.8. These were the welds in steels 301 (Cr_{eq}/Ni_{eq} = 2.07), 304/1 (Cr_{eq}/Ni_{eq} = 1.81) and 316/1 (Cr_{eq}/Ni_{eq} = 1.76). The most “ferritic” of the steels, AISI 301, exhibited fully ferritic solidification succeeded by transformation to austenite via Widmanstätten mechanism in solid state. Only a small amount of ferrite remained in the microstructure at room temperature at all welding speeds.

In the second most ferritic steel, 304/1, the GTA-welds showed primary ferritic solidification yielding both skeletal and lathy ferrite morphologies in the microstructure. In the laser welds, the solidification was found to change from FA mode to fully ferritic mode at the weld centerlines. In other parts of the laser welds

the ferrite morphology was mostly of lathy type but some skeletal ferrite was also present.

The steel 316/1 that has a Cr_{eq}/Ni_{eq} ratio close to that of 304/1 behaved in a similar way. In 316/1 the weld centerlines were found to show fully ferritic solidification when the welding speed exceeded 1000 mm/min. With increasing welding speed the amount of Widmanstätten austenite was found to increase. With welding speeds in excess of 4000 mm/min the whole weld was found to solidify in fully ferritic mode. The microstructural development as a function of welding speed is seen in Fig. 3.8.

3.2.2 Change in solidification mode

The steel 316/2 having Cr_{eq}/Ni_{eq} of 1.62 was a typical example that showed a change in the solidification mode with increasing the welding speed. In GTA-welding the welds were noticed to solidify in primary ferritic mode, consisting mainly of skeletal ferrite in the microstructure, c.f. Fig. 3.9a. A similar solidification pattern was observed for welding speeds up to 1500 mm/min. Higher speeds resulted in a mixed solidification of primary ferritic and primary austenitic modes, see Fig. 3.9b and c. With increasing the welding speed the extent of primary austenitic solidification was found to increase so that with the highest speed applied the solidification was mostly primary austenitic showing cellular-dendritic and columnar-dendritic morphology, Fig. 3.9d.

3.2.3 Primary and fully austenitic solidification

The welds of steels 316/3 (Cr_{eq}/Ni_{eq} = 1.46), 304/2 (Cr_{eq}/Ni_{eq} = 1.44), 6Mo/1 (Cr_{eq}/Ni_{eq} = 1.32), 6Mo/2 (Cr_{eq}/Ni_{eq} = 1.14) and 6Mo/3 (Cr_{eq}/Ni_{eq} = 1.05) showed primary or fully austenitic solidification with a typical appearance of Fig. 3.10.

The microstructures of welds 316/3 and 304/2 were rather similar, arising from the almost equal Cr_{eq}/Ni_{eq} ratio. The welds contained primary austenite dendrites or cells with secondary interdendritic ferrite. At the lowest speeds, the solidification morphology was mainly columnar dendritic. By increasing welding speed above 400 - 600 mm/min, a mixture of columnar and cellular-dendritic structure prevailed in the microstructure.

In the 6% Mo-alloyed welds 6Mo/1 and 6Mo/2 the solidification mode was primary austenitic whereas 6Mo/3 welds showed fully austenitic solidification. The solidification morphology of welds 6Mo/1 and 6Mo/2 consisted of primary austenite dendrites or cells with secondary ferrite at interdendritic regions. With increasing the welding speed the proportion of cellular-dendritic structure increased substituting columnar dendrites, see Fig. 3.10. Steel 6Mo/1 having a higher Cr_{eq}/Ni_{eq} ratio showed greater amounts of secondary ferrite, the amount of which decreased with increasing welding speed. From GTA-welds of steel 6Mo/2 secondary ferrite was found only occasionally. The laser welds of this steel showed fully austenitic solidification.

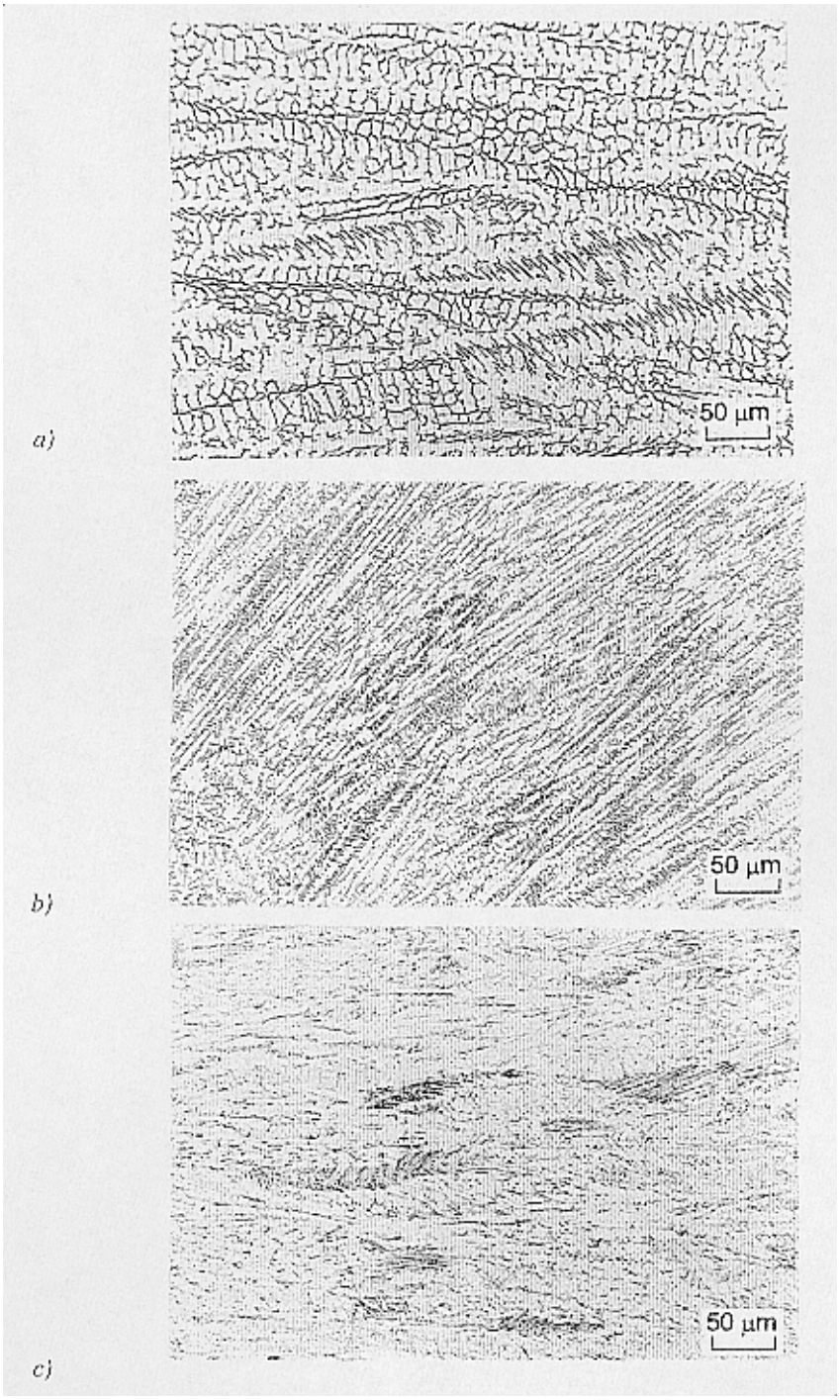

c)

Fig. 3.8. Weld metal microstructures of 316/1 steel midway between the weld centerline and fusion line. GTA-weld with welding speed of 100 mm/min (a) and laser welds with welding speeds of 1000 mm/min (b) and 5000 mm/min (c). Ferrite is dark, austenite is light.

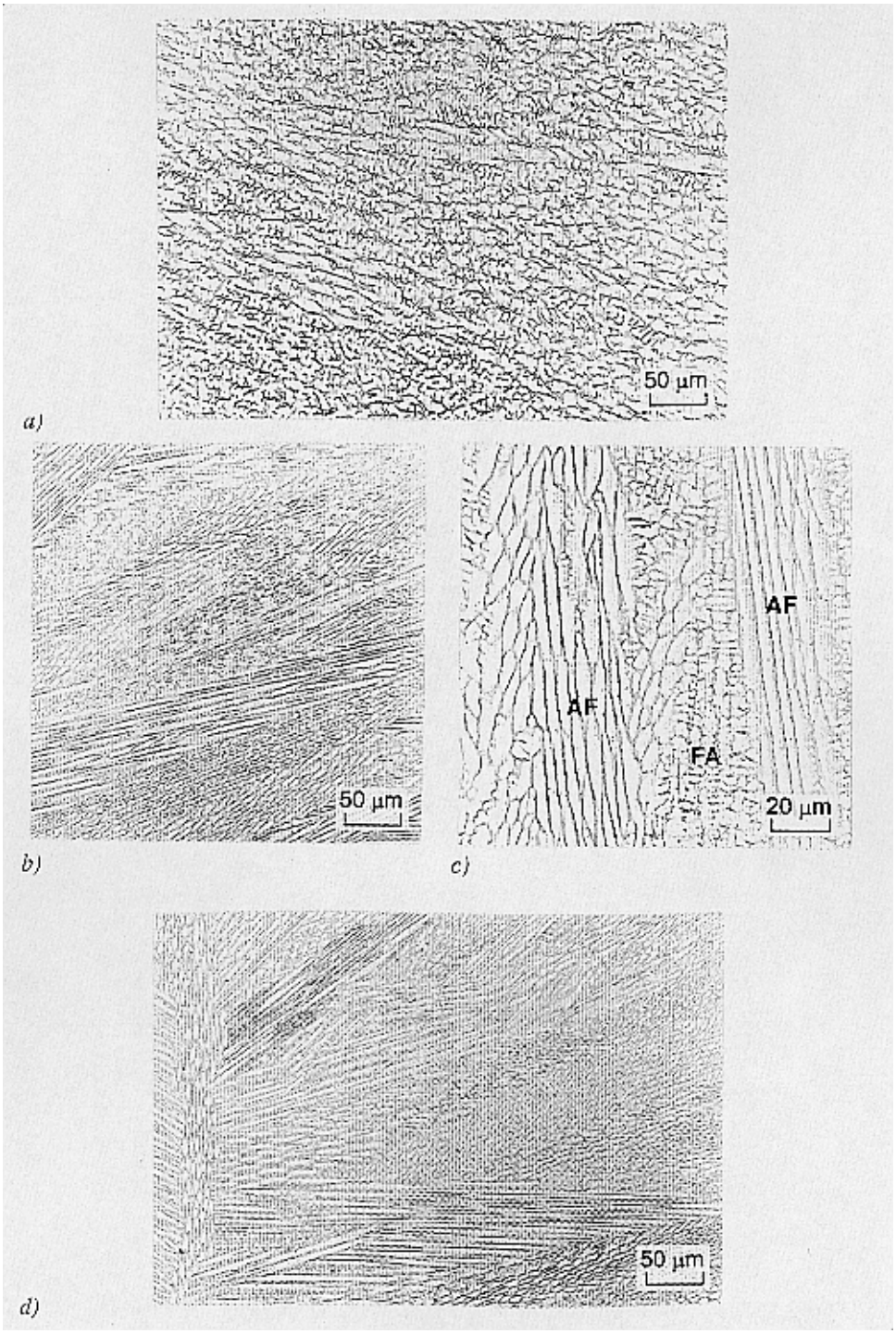

Fig. 3.9. Weld metal microstructures of AISI 316/2 steel midway between the weld centerline and fusion line. GTA-weld with welding speed of 200 mm/min (a) and laser welds with welding speeds of 3000 mm/min (b, c) and 5000 mm/min (d).

For further identification of microstructures the welds of 6Mo/1 and 6Mo/2 steels were studied by scanning electron microscope applying a backscattering electron image technique. The investigation revealed intermetallic phase precipitation accompanied by secondary ferrite present at the interdendritic regions, c.f. Fig. 3.11. According to EDS-analyses the regions containing intermetallic phase showed higher Cr- and Mo-contents (23% Cr, 14% Mo) than did δ-ferrite (21% Cr, 8% Mo) and austenite (20% Cr, 5% Mo). The amount of this intermetallic phase decreased with increasing the welding speed.

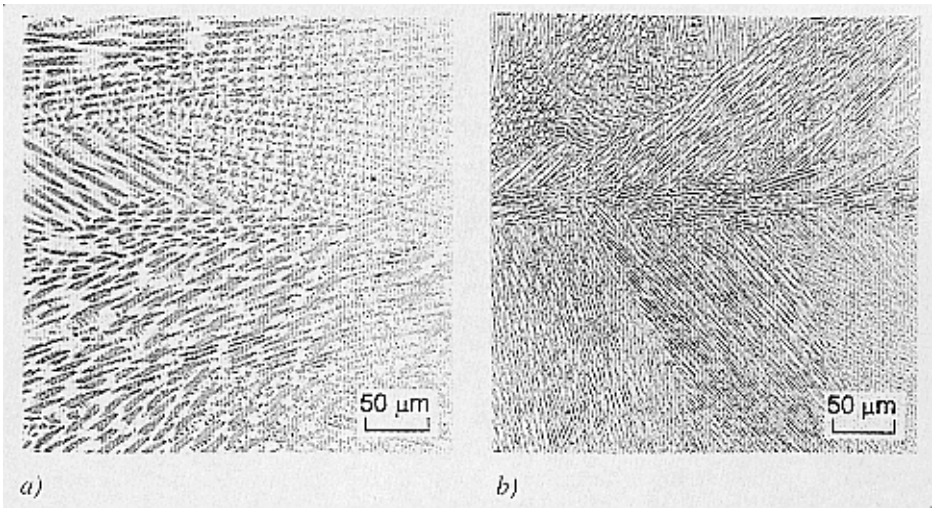

Fig. 3.10. Weld metal microstructures of 6Mo/1 steel. GTA-weld with welding speed of 800 mm/min (a) and laser weld with welding speed of 5000 mm/min (b). With increasing the welding speed the proportion of cellular-dendritic structure is replaced by columnar dendrites.

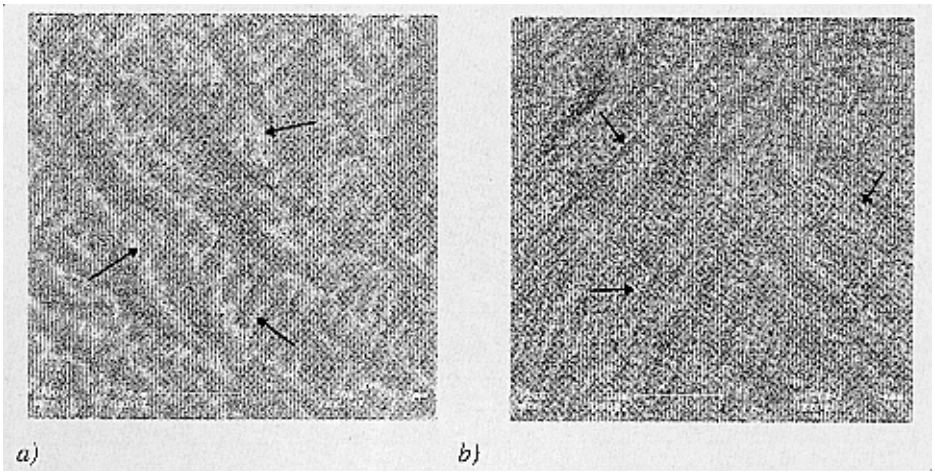

Fig. 3.11. SEM backscatter images showing the morphology of interdendritic δ-ferrite and secondary intermetallic phase present in the 6Mo/1 welds (arrows). GTA-weld 100 mm/min (a) and laser weld 1000 mm/min (b).

3.2.4 Ferrite contents

The ferrite contents measured by Ferritscope meter from the low-speed GTA-weld metals (welding speed 100 mm/min) and predicted using the DeLong and WRC diagrams are shown in Table 3.1. For steel AISI 301 the Ferritscope method yields noticeably higher ferrite contents than do the DeLong and WRC prediction diagrams. Concerning steels AISI 304 and 316, a reasonable agreement between the Ferritscope measurements and the predictions is noticed. The 6% Mo steel welds did not show any indication of ferrite measured by the Ferritscope method.

The ferrite contents of the GTA- and laser welds were further studied by optical image analysis with the results shown in Fig. 3.12. As expected, the ferrite content of the GTA-welds of AISI 301, 304 and 316 steels (Fig. 3.12a and b) remains higher in welds having higher Cr_{eq}/Ni_{eq} ratios and primary or fully ferritic solidification. Correspondingly, welds having lower Cr_{eq}/Ni_{eq} ratios and primary austenitic solidification showed remarkably lower ferrite contents. With increasing welding speed the weld metal ferrite content was found to decrease, except in the case of steel 304/2 which showed very low ferrite content already in the low-speed GTA-weld.

Optical image analyses revealed that also the welds of the 6% Mo steels include δ-ferrite and/or some second phase, c.f. Fig. 3.12c. This was the case especially with the 6Mo/1 steel which has a higher Cr_{eq}/Ni_{eq} ratio, whereas the 6Mo/2 steel showed considerably lower ferrite and second phase contents. The measurements based on the optical microscopy and SEM backscattering analyses agreeably show that the amount of ferrite and second phase decreases with increasing the welding speed. There, however, exists deviation between the measurement methods. In addition to statistical scatter this may arise from differences in the analysing technique: the optical microscopy contains the portions of both ferrite and second phase, whereas the SEM backscattering analyses, performed with polished samples, detect only the portions of the second phase.

Table 3.1. Ferrite contents of the low-speed GTA-welds measured by Ferritscope meter and predicted by DeLong and WRC diagrams (DeLong 1974, Kotecki & Siewert 1992). The number of measurements was 10.

Steel	Cr_{eq} / Ni_{eq}	Ferritscope (%)		DeLong (1974)		WRC 1992	
		Average	Standard dev.	FN	% [1]	FN	% [1]
301	2.07	21.3	2.34	8	7.6	8	7.6
304/1	1.81	5.1	0.2	7	6.8	9	8.4
304/2	1.44	0.1	0.1	0	0	2	2
316/1	1.76	6.9	0.3	7	6.8	8	7.6
316/2	1.62	5.1	0.4	3	3	4	4
316/3	1.41	0.7	0.1	1	1	1	1
6Mo/1	1.32	0	0	-	-	-	-
6Mo/2	1.14	0	0	-	-	-	-

[1] Transformed from FN to percentages according to DeLong (1974).

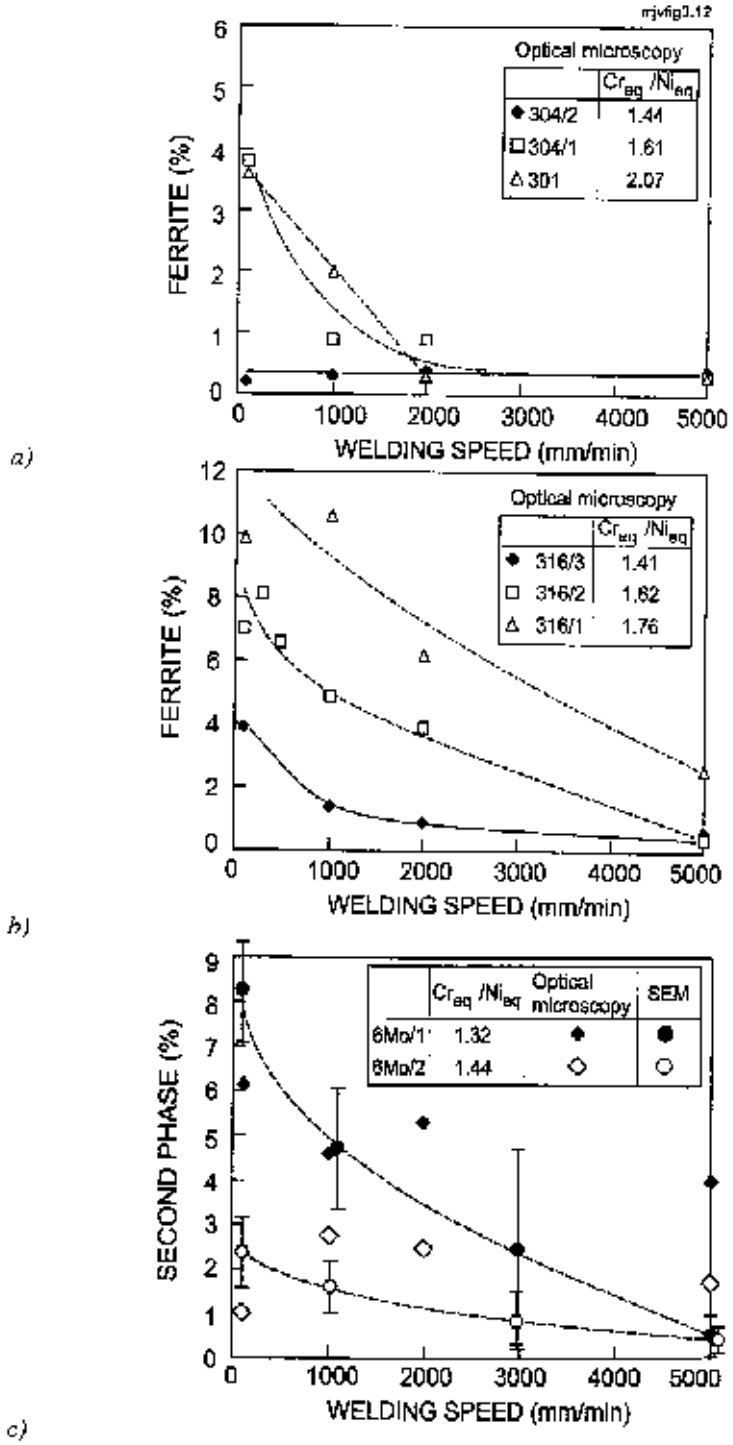

Fig. 3.12. The results of the optical image analyses for 301 and 304 steels (a), 316 steels (b) and 6% Mo steels (c) as a function of welding speed.

3.3 Microanalyses

3.3.1 EPMA line scan analyses

Typical results of the electron probe microanalyses taken from the test welds are shown in Appendix 7. As expected, considerable compositional differences can be observed in the welds when analysed over the solidification microstructure. Welds having primary ferritic solidification showed enrichment of Cr and Mo in δ-ferrite and enrichment of Ni in austenite (Appendix 7, Figs A7.1 - A7.3). Due to solid state transformation from ferrite to austenite the direction of segregation originating from solidification was not possible to judge unambiguously. In primary austenitic solidification the direction of microsegregation became evident, however. In AISI 304 and 316 steels Cr and Mo segregated in the same phase towards the interdendritic regions whereas Ni shows a slight enrichment in the opposite direction, i.e., to dendrite cores (Appendix 7, Figs A7.4 - A7.6). With increasing welding speed the inhomogeneity of the welds studied showed a considerable decrease, see Appendix 7, Figs A7.7 - A7.10.

Figures 3.13 - 3.15 summarise all the measurements by showing the effect of steel composition on segregation behaviour expressed as C(min/av) ratios for Cr, Ni and Mo. The change from primary austenitic to primary ferritic solidification does not seem to have any pronounced effect on the segregation behaviour of Cr. There exists a more distinct drop in the C(min/av) ratio for Ni, located at the FA/AF demarcation. For Mo results indicate that the C(min/av) ratio increases slightly with increasing Cr_{eq}/Ni_{eq} ratio, see Fig. 3.15. Correspondingly, the summarised effect of Cr and Mo expressed as PRE(min/av) ratio shows a slightly increasing trend with Cr_{eq}/Ni_{eq} ratio, c.f. Fig. 3.16.

The results also indicate (Figs 3.13 - 3.16 and Appendix 7, Figs A7.1 - A7.6) that the segregation profiles measured by EPMA at different locations of the weld surface do not exhibit noticeable differences in segregation degree. Only in some individual cases does the weld fusion line show slightly higher segregation than do the ¼ width and weld centerline regions. In the great majority of the cases these possible differences were, however, undetectable and hidden behind overall scatter in the measurement results. For this reason the segregation phenomena of the welds were handled using the average values of these three independent measurements.

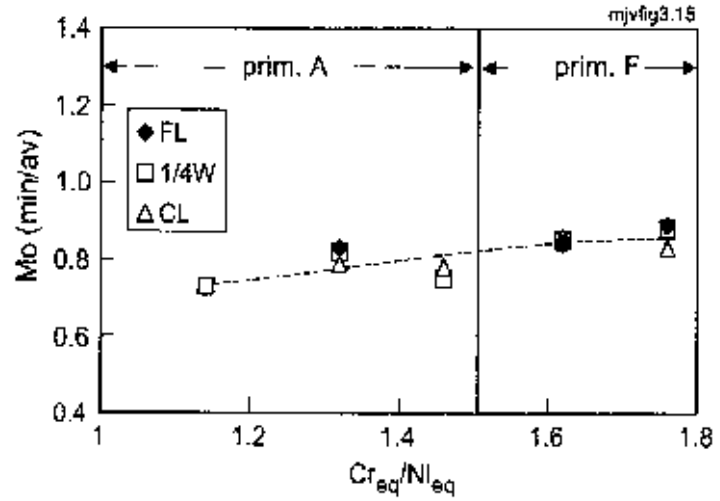

Fig. 3.13. The effect of steel composition on the Cr(min/av) ratio measured from three locations of the low-speed GTA-weld metals studied (welding speed 100 mm/min, FL = weld metal close to fusion line, ¼ W = ¼ width and CL = weld metal close to centerline).

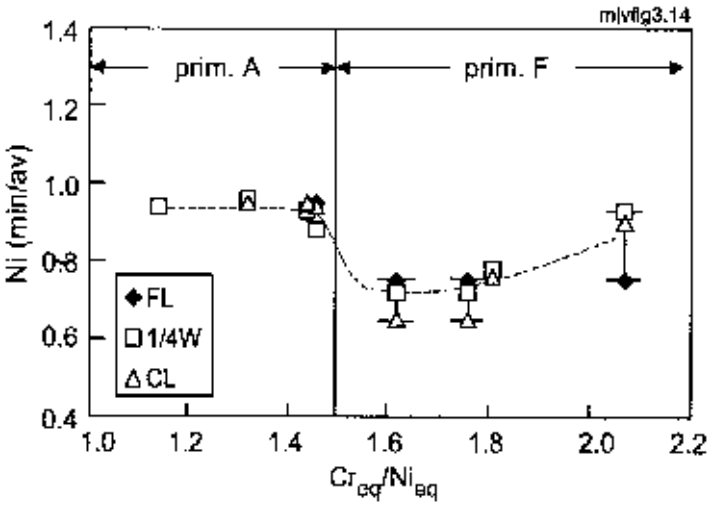

Fig. 3.14. The effect of steel composition on the Ni(min/av) ratio measured from three locations of the low-speed GTA-weld metals studied (welding speed 100 mm/min, FL = weld metal close to fusion line, ¼ W = ¼ width and CL = weld metal close to centerline).

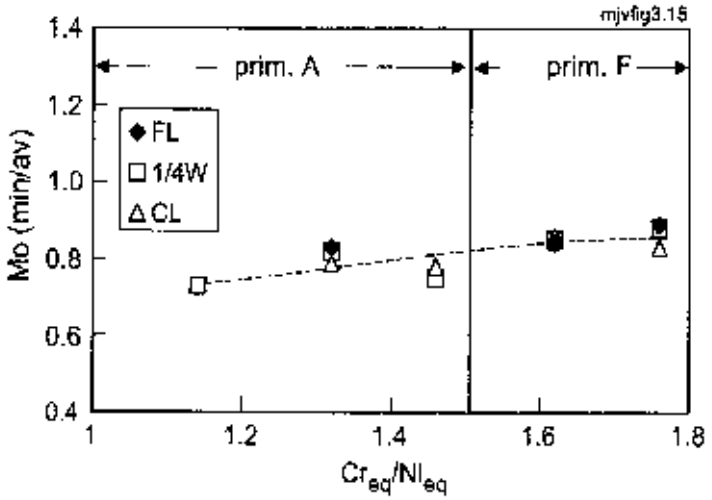

Fig. 3.15. The effect of steel composition on the Mo(min/av) ratio measured from three locations of the low-speed GTA-weld metals studied (welding speed 100 mm/min, FL = weld metal close to fusion line, ¼ W = ¼ width and CL = weld metal close to centerline).

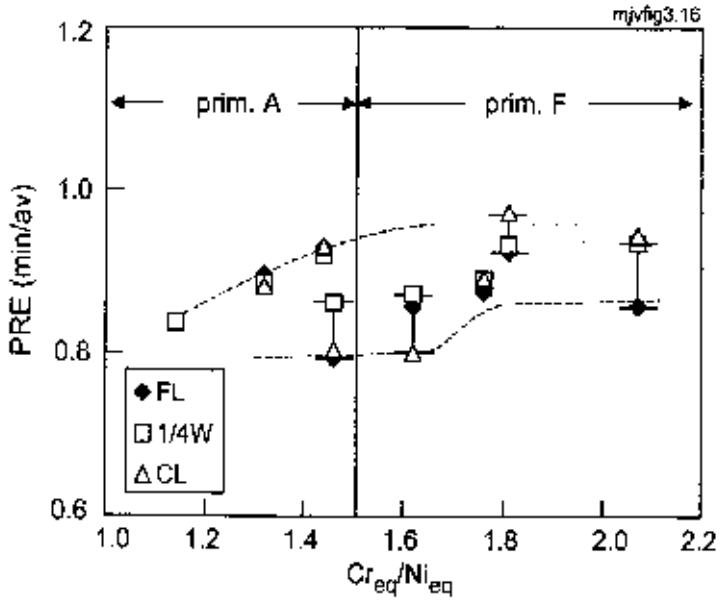

Fig. 3.16. The effect of steel composition on the PRE(min/av) ratio based on measurements from three locations of the low-speed GTA-weld metals studied (welding speed 100 mm/min, FL = weld metal close to fusion line, ¼ W = ¼ width and CL = weld metal close to centerline).

The effect of welding speed on segregation behaviour was further demonstrated by plotting the C(max/min) and C(min/av) ratios obtained from the EPMA measurements. Figures 3.17 and 3.18 summarise these results expressed as PRE-index. The beneficial effect of increasing welding speed is clearly demonstrated. Also the steel composition seems to have a distinct effect on weld segregation behaviour (Fig. 3.18). The welds showing primary austenitic solidification (i.e. $Cr_{eq}/Ni_{eq} < 1.5$ for conventional arc welds) are noticed to show higher degree of inhomogeneity. It is also evident that the degree of segregation expressed as PRE(max/min) ratio seems to be more affected by composition and welding speed than that expressed as PRE(min/av) ratio.

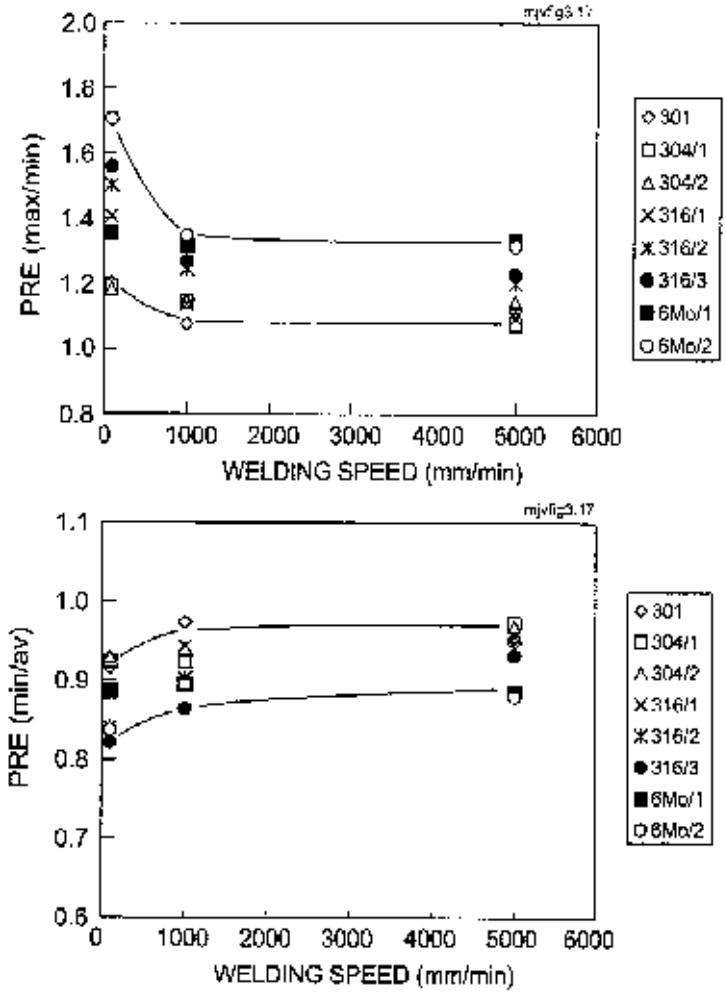

Fig. 3.17. The PRE(max/min) and PRE(min/av) ratios calculated from the EPMA line scan analyses as a function of welding speed.

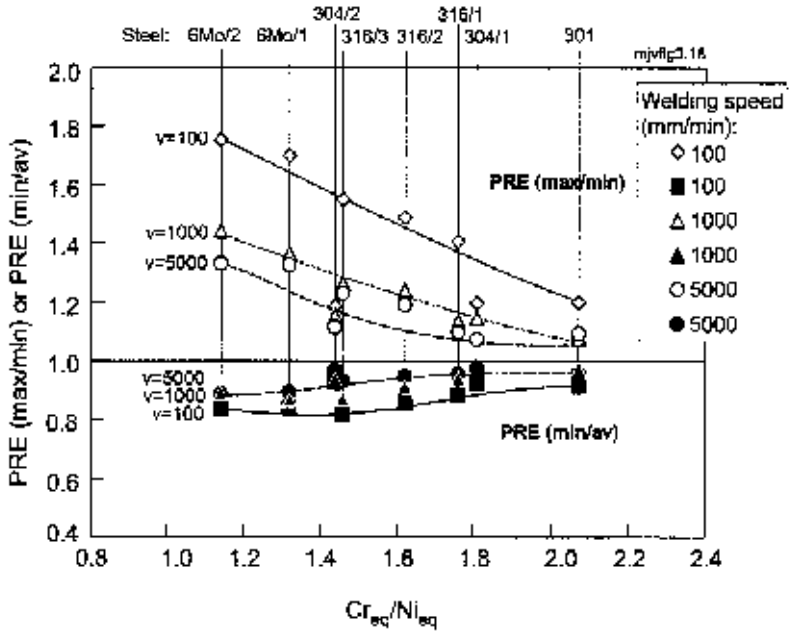

Fig. 3.18. The effect of steel composition (expressed as Cr_{eq}/Ni_{eq} ratio) on segregation behaviour of the welds studied for welding speeds of 100, 1000 and 5000 mm/min, based on the EPMA line scan analyses.

3.3.2 CMA mapping

Two dimensional computer aided microprobe analyses (CMA) were applied in examining the magnitude of microsegregation in welds of steel 6Mo/1. Results for the three welding speeds studied are shown in Appendix 8. Results supported those of the EPMA line scan analyses in showing a distinct decrease in the magnitude of segregation with increase in welding speed from 100 mm/min to 1500 mm/min and, further, to 5000 mm/min. The direction of microsegregation was noticed to be consistent with the EPMA line scan analyses. Appendix 8 (Fig. A8.2) shows the results of the CMA analyses expressed as local variation of PRE-index of the weld metals studied. Due to microsegregation of Cr and Mo towards interdendritic regions, the dendrite cores exhibit the lowest PRE-values. With increasing the welding speed the variation of PRE-index, however, clearly decreases.

3.3.3 Nitrogen analyses

Nitrogen content of some representative weld metals are shown in Table 3.2. For steel 316/2 the measurements show that the weld metal nitrogen content remains close to the base metal level for all studied welding speeds. For steel 6Mo/2, the low-speed GTA-weld, however, shows nitrogen loss with respect to base metal nitrogen content. The weld metal nitrogen content again becomes close to the base

metal level with increasing welding speed to 800 mm/min or more. For steel 6Mo/3 even a slightly higher nitrogen loss than measured for low-speed welding of 6Mo/2 steel takes place when using pure Ar as a shielding gas. With nitrogen addition to the shielding gas, weld nitrogen content again increases almost to the base metal level.

Table 3.2. Weld metal nitrogen contents expressed as averages of two measurements. In high-speed welds the nitrogen content has been calculated from the volume fraction of weld metal and base metal in the analysed sample (equation 21).

a) Effect of welding speed in GTA- and laser welding

Steel	N_{bm}	N_{weld}				
		GTAW		Laser		
		100 [1]	800	2000	4000	5000
316/2	0.052	0.055	0.053	0.054	0.059	-
6Mo/2	0.184	0.149	0.172	0.178	0.174	0.173

[1] welding speed (mm/min)

b) Effect of shielding gas in GTA-welding (welding speed 200 mm/min)

Steel	N_{bm}	N_{weld}	
		Ar (99.998%)	Ar + 10.5% N_2
6Mo/3	0.210	0.140	0.190

The distribution of nitrogen was also studied by the SEM-Q microsond analyser with results shown in Fig. 3.19. The measurements were performed for 6Mo/3 welds using pure argon and Ar plus 10.5% nitrogen as shielding gas. Results indicate that the nitrogen content of the weld metal is higher at the interdendritic regions than at the dendrite cores for both shielding gases. The segregation and partitioning of nitrogen is noticed to take place in the same phase with Cr and Mo. Nitrogen addition to the shielding gas seems to increase the nitrogen content both at the interdendritic regions and at the dendrite cores.

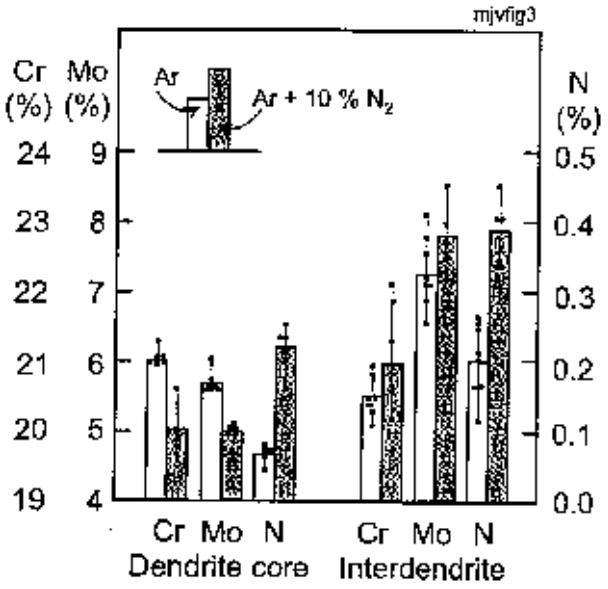

Fig. 3.19. Partitioning of Cr, Mo and N between dendrite cores and interdendritic regions in 6Mo/3 welds measured by SEM-Q (EPMA) microsond analyser. The analyses have been taken from various locations at weld centerline regions.

3.3.4 Transmission electron microscopy

A scanning-transmission electron microscope equipped with field emission gun (FEG-STEM) was used in analysing the effect of welding speed on weld metal microstructure. For steel 316/1 showing primary ferritic solidification, the results indicate that an increase in welding speed from 100 mm/min (Fig. 3.20) to 5000 mm/min (Fig. 3.21) results in a more homogeneous distribution of Cr, Ni and especially Mo over the analysed region.

The effect of welding speed was correspondingly demonstrated with 6% Mo alloyed steel, c.f. Figs 3.22 - 3.25. The welds of this steel were shown to exhibit precipitation of intermetallic phase at the interdendritic regions, c.f. Fig. 3.22. The diffraction analyses of the weld metal reported elsewhere (Nenonen et al. 1998) revealed that the intermetallic phase is σ-phase which has nucleated and grown into δ-ferrite. The line analyses made over different phases revealed that Cr- and especially Mo-contents of the σ-phase are considerably higher than those of the δ-ferrite and austenite, see Fig. 3.23. Comparative studies of the high-speed laser weld (5000 mm/min) of the same steel revealed that high welding speed significantly decreases the solidification cell size and precipitation of σ-phase, see Fig. 3.24. High-speed welding also decreases the magnitude of interdendritic segregation of Cr and Mo in fully austenitic regions, c.f. Fig. 3.25. At regions where δ-ferrite and small particles of σ-phase remained in the microstructure the line analyses again revealed higher variations of Cr, Mo and Ni that were of the same order of magnitude as in case of the low-speed weld.

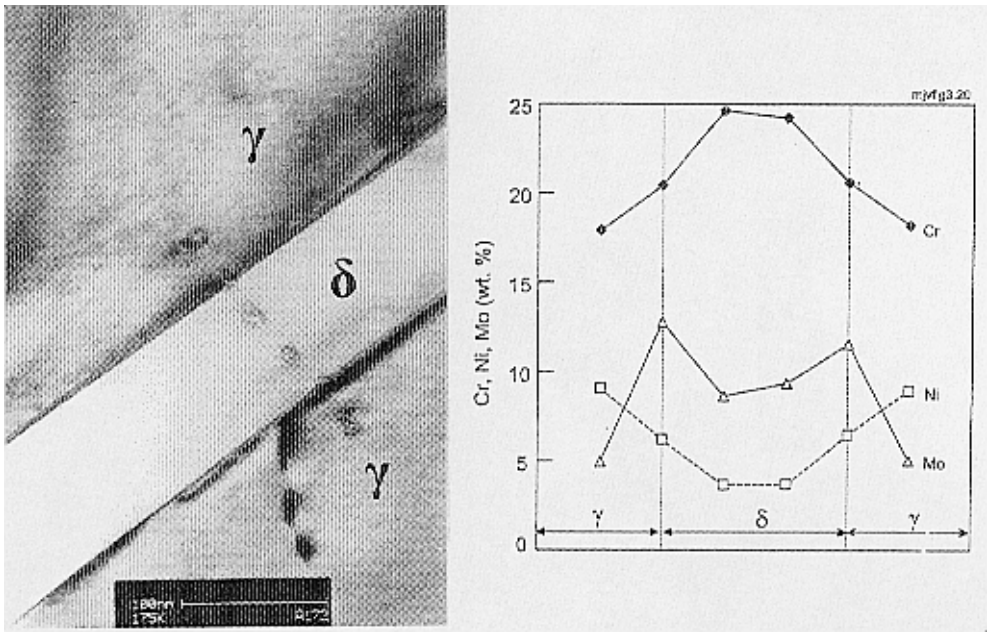

Fig. 3.20. Distribution of Cr, Ni and Mo over δ/γ interface in 316/1 steel weld (GTA-welding, 100 mm/min).

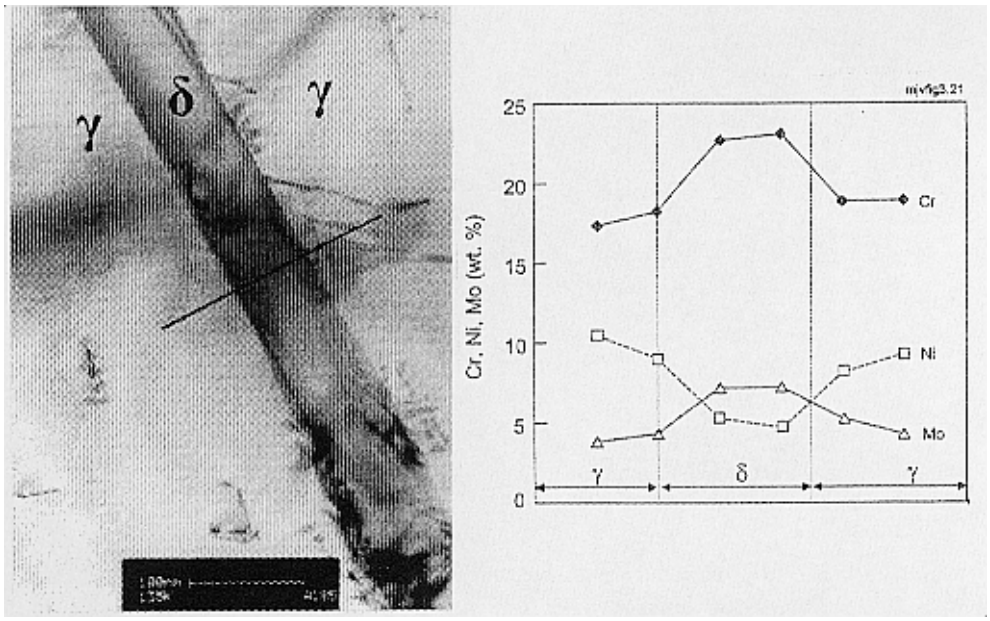

Fig. 3.21. Distribution of Cr, Ni and Mo over δ/γ interface in 316/1 steel weld (laser welding, 5000 mm/min).

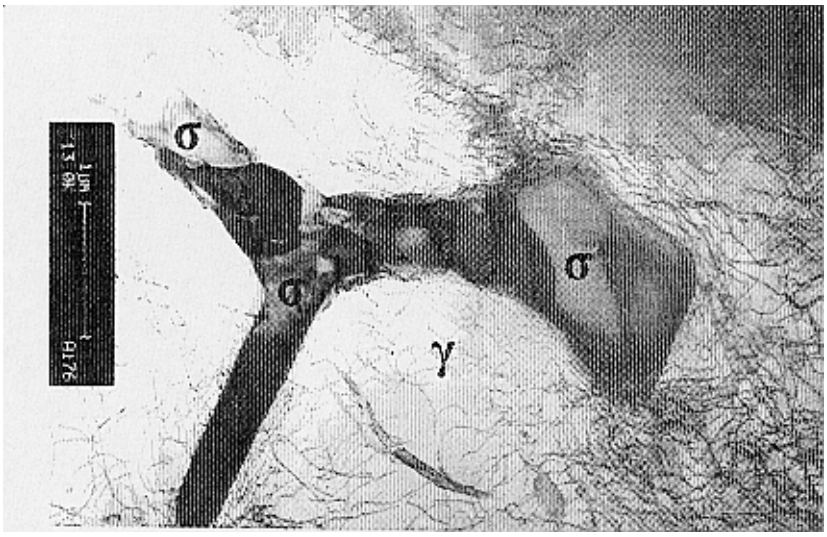

Fig. 3.22. Typical microstructure of the GTA-weld of steel 6Mo/1 welded with speed of 100 mm/min. Coarse σ-phase is detected at the interdendritic region.

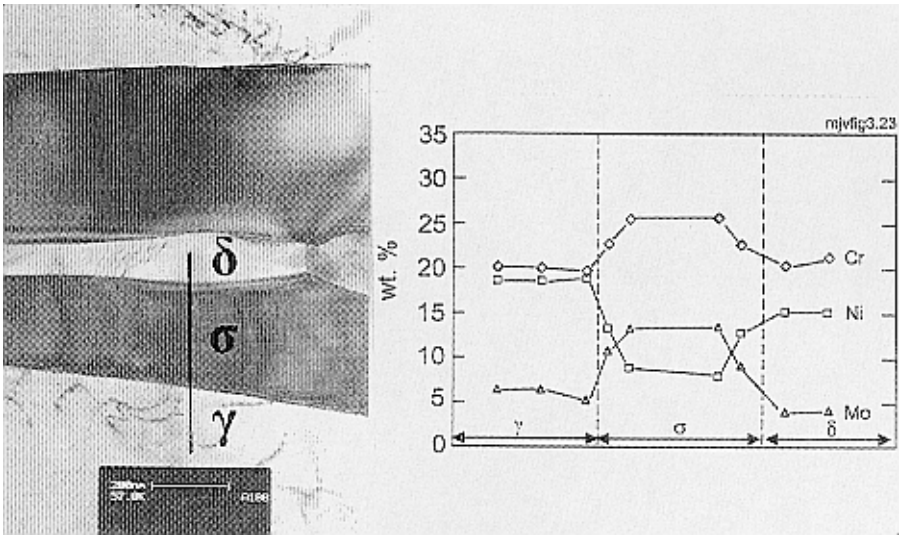

a) *b)*

Fig. 3.23. Microstructure and line analyses of GTA-weld of steel 6Mo/1 welded with speed of 100 mm/min. δ-ferrite inside the σ-phase (a) and results of the line scan analyses over the microstructure (b).

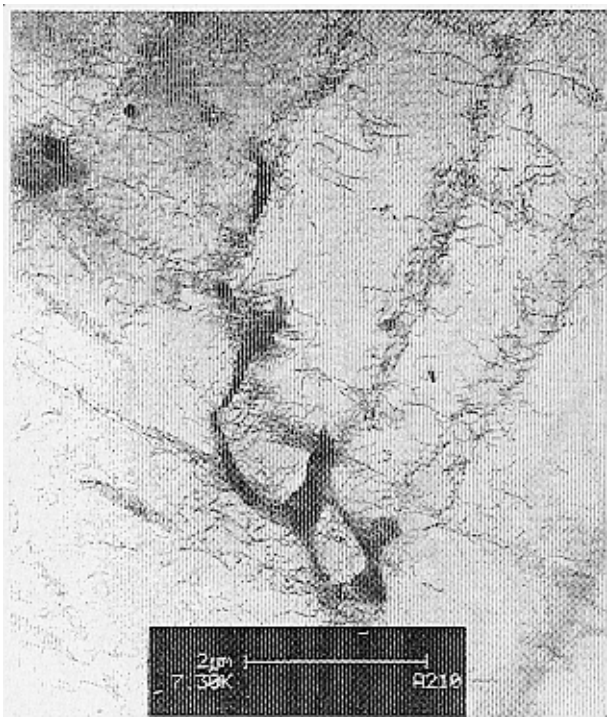

Fig. 3.24. Microstructure of laser weld of steel 6Mo/1 welded with speed of 5000 mm/min showing a small amount of second phase at the intercellular regions.

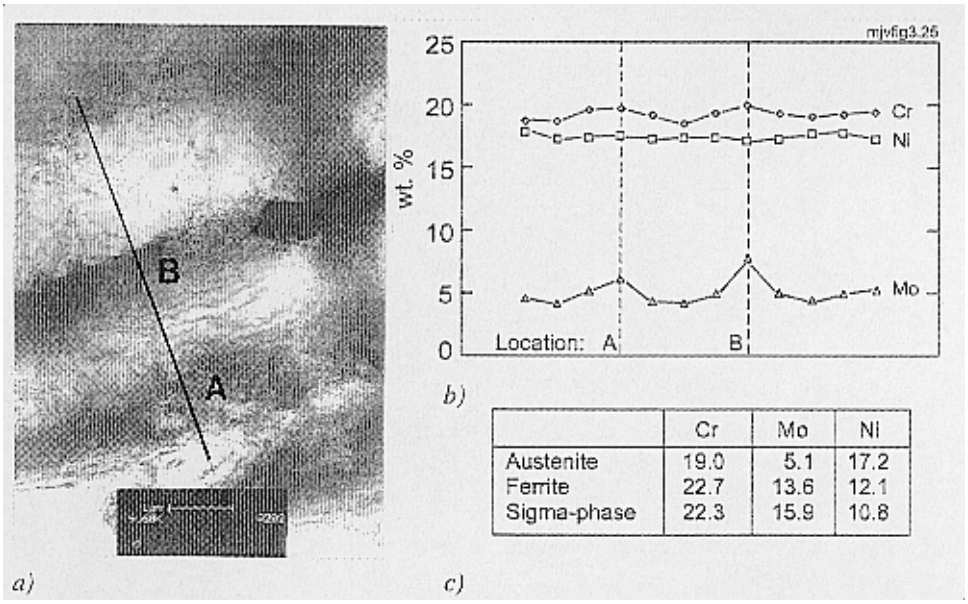

	Cr	Mo	Ni
Austenite	19.0	5.1	17.2
Ferrite	22.7	13.6	12.1
Sigma-phase	22.3	15.9	10.8

Fig. 3.25. Microstructure and line scan analyses of laser weld of steel 6Mo/1 welded with speed of 5000 mm/min. Fine cellular solidification structure (a), the results of the line scan analyses over fully austenitic microstructure (b) and Cr, Ni and Mo contents of austenite, δ-ferrite and σ-phase at regions where detected (c).

3.4 Corrosion properties

3.4.1 Potential measurements

Results of the potentiodynamic measurements for the welded samples are presented in Figs 3.26 and 3.27. For AISI 301, 304/1 and 304/2 welds the pitting potentials lie very close to the corresponding base metal values, see Fig. 3.26. An increase in the welding speed does not, therefore, seem to have any noticeable effect on pitting potential of these welds. The 304/1 and 304/2 welds, however, systematically exhibit somewhat higher pitting potentials than do the AISI 301 welds.

The Mo-alloyed AISI 316 welds have noticeably higher pitting potentials than AISI 301 and 304 type welds, see Fig. 3.27. A low welding speed is clearly found to deteriorate the pitting potential of these Mo-alloyed welds. The drop in the pitting potential seems to be higher with 316/1 steel than with 316/2 and 316/3 steels. With increasing welding speed from 100 mm/min the pitting potential of all the welds is noticeably increased. The 316/1 steel shows highest tendency to increase pitting potential. In the 316/2 and 316/3 steels the pitting potentials of the high-speed laser welds remain somewhat lower.

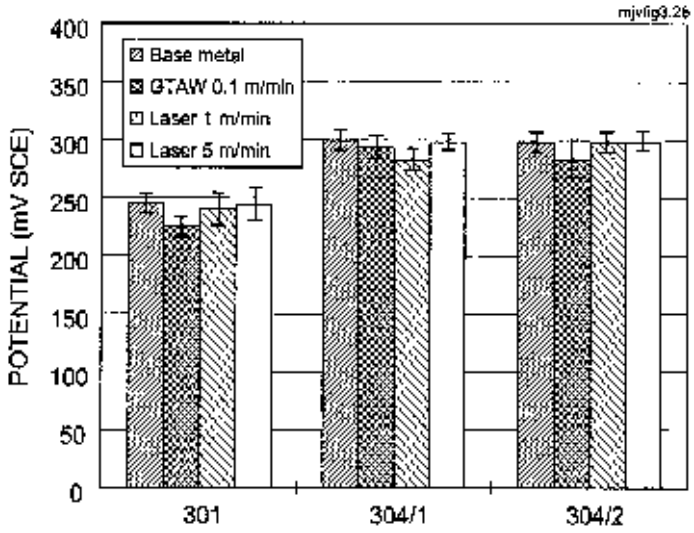

Fig. 3.26. Results of pitting potential measurements in 3.56% NaCl for AISI 301 and 304 steels

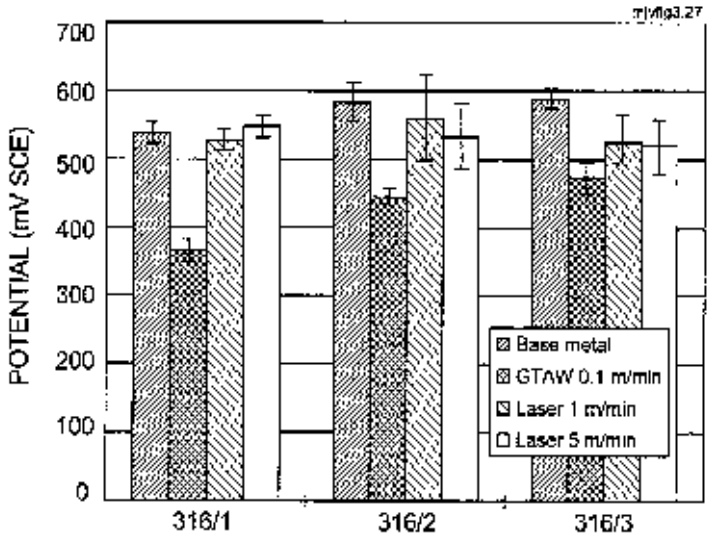

Fig. 3.27. Results of pitting potential measurements in 3.56% NaCl for AISI 316 steels.

3.4.2 $FeCl_3$ immersion tests

The results of the $FeCl_3$ immersion tests expressed as critical pitting temperatures are summarised in Figure 3.28. Agreeably to Fig. 1.11 the measurements show that the CPT-temperatures of the base metals and the welds depend strongly from the composition. For steels and welds of AISI 301 and 304 steels the CPT-temperatures fall systematically below 5°C, which due to crystallisation of $FeCl_3$ is a lower limit for the test method. For Mo-alloyed AISI 316 and 6% Mo steels the CPT-temperatures became measurable. In case of 6% Mo steels laser welding (1000 mm/min) seems to lead to about 5 - 10°C higher CPT-temperature than does GTAW (100 mm/min).

Fig. 3.28 summarises also the results of the reference tests carried out for steel 6Mo/3 welds applying nitrogen alloyed shielding gases. Nitrogen addition to the shielding gas seems systematically to improve the CPT-temperature of the weld metal. The measured rise in the CPT-temperature of the 6Mo/3 steel welds by applying nitrogen addition is 5 - 10°C which is practically the same as in the case of increasing the welding speed from 100 mm/min to 1000 mm/min. The applicability of nitrogen alloyed shielding gas was, however, limited due to rapid electrode deterioration with nitrogen contents in excess of 5% in the shielding gas.

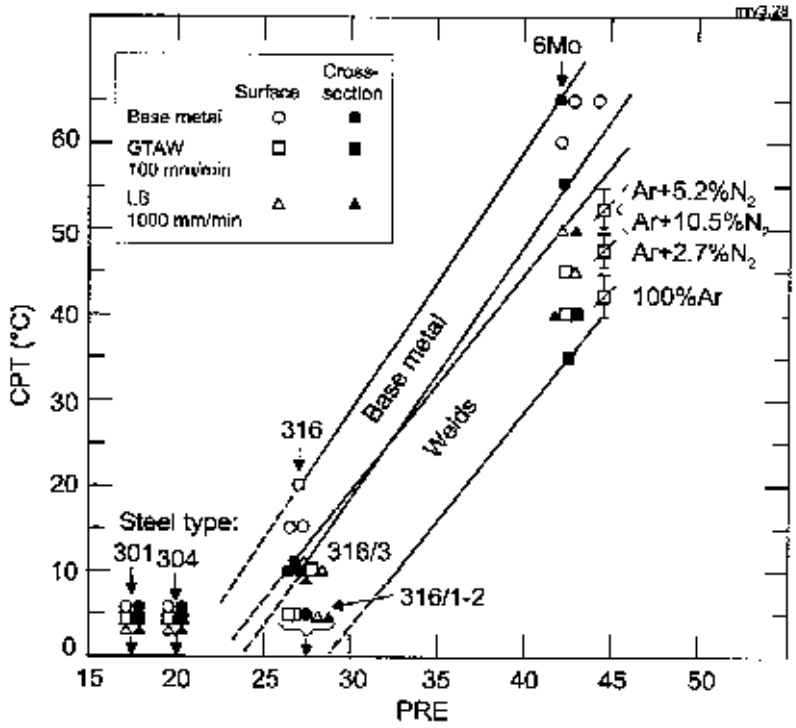

Figure 3.28. The results of the $FeCl_3$ immersion tests of the base metals and welds expressed as function of pitting resistance equivalent (PRE= Cr + 3.3Mo + 13N).

SEM investigations were further used to study the location of the corrosion pits with respect to weld microstructure. In GTA-welds of steel 316/1 showing primary ferritic solidification corrosion pits were observed to locate close to δ-ferrite/austenite phase boundaries with further propagation to austenite leaving δ-ferrite uncorroded, c.f. Figs 3.29 and 3.30. The laser welds exhibited lower pit density, though the mechanism was the same as for the GTA-welds. In primary austenitic solidification, pitting corrosion was concentrated along austenite dendrites as shown by Fig. 3.31. Again laser welds displayed less growth of corrosion pits than did the GTA-welds.

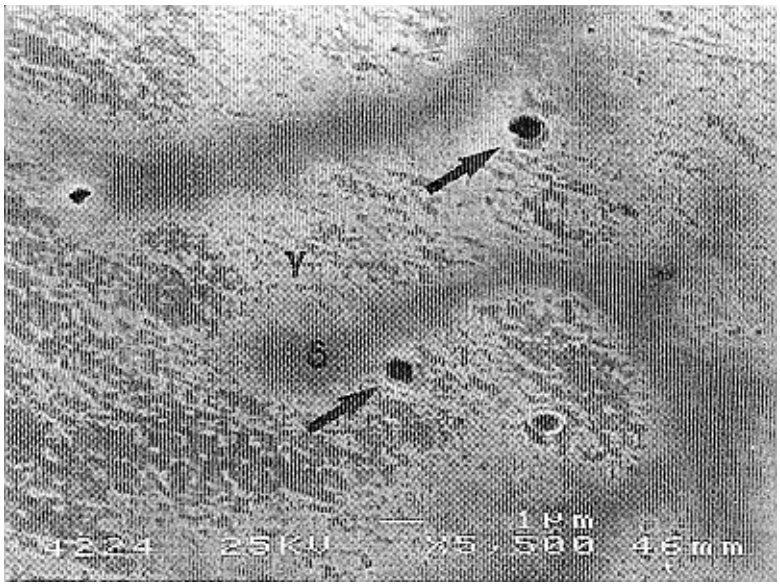

Fig. 3.29. Pit initiation and growth in the vicinity of δ/γ phase boundaries in GTA-weld of 316/1 steel showing primary ferritic solidification.

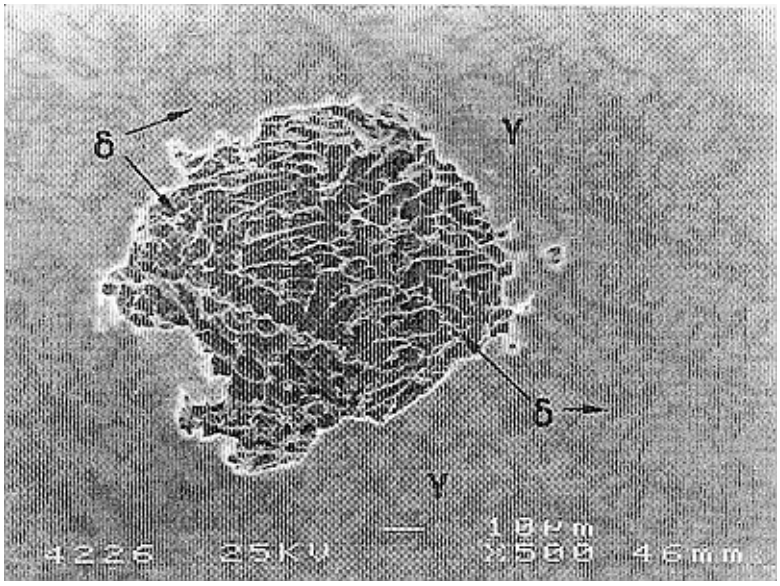

Fig. 3.30. Pit growth in the weld of 316/1 steel. Austenite is corroding selectively and δ-ferrite remains in the microstructure.

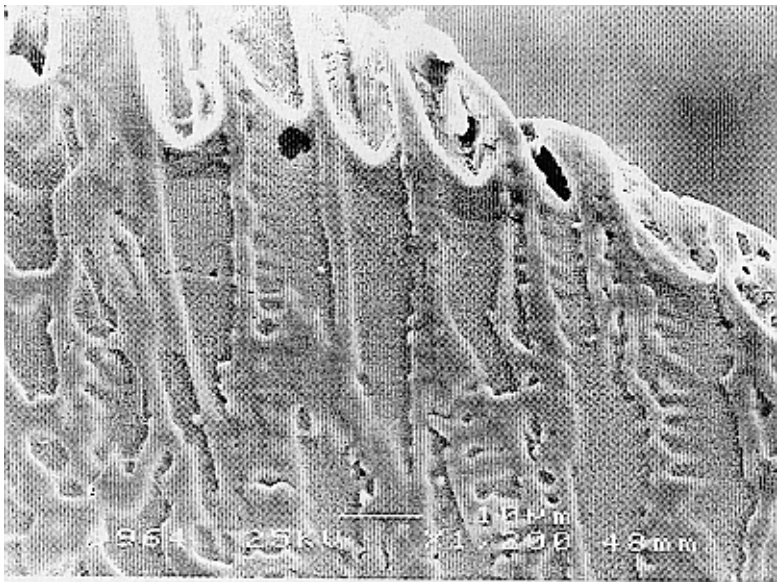

Fig. 3.31. Propagation of pitting corrosion along austenitic dendrite cores in GTA-weld of 6Mo/3 steel (shielding gas 100% Ar).

3.5 Modelling

3.5.1 Macroscopic simulations

Macroscopic simulation of autogenous GTA-welding was implemented in two phases: (1) comparing the calculated weld shapes to measured data and (2) studying the effect of weld shape variations on solidification parameters.

The results of phase (1) simulations for steel AISI 304/2 are shown in Figs 3.32 and 3.33. With both welding speeds the calculated convective flow is directed outward from the weld centerline with maximum flow rates of 29 cm/s and 34 cm/s for welding speeds of 100 mm/min and 200 mm/min, respectively. For both simulations the calculated penetrations correlate well with experiments. The weld width, however, becomes somewhat larger in simulations than in experiments. In surface sections the calculated and experimental pool shapes are reasonably close, see Fig. 3.33.

Phase (2) simulations were intended to study possible effects of weld shape variations on solidification parameters of autogenous GTA-welds. For this purpose welding of steel AISI 304 was simulated using two welding speeds (100 and 400 mm/min) and two sulphur contents (20 and 150 ppm) with the results shown in Fig. 3.34. Both of these parameters have a remarkable effect on weld penetration shape. At the lower welding speed, an increase in the sulphur content reverses the flow rate from outward to inward which drastically increases the weld

penetration. In the case of higher welding speed, however, the flow rate is not changed and also the weld penetration remains almost the same. The maximum flow rate of the low-speed welds is 36 cm/s and decreases to 25 - 26 cm/s when the sulphur content is increased from 20 to 150 ppm.

Solidification parameters, i.e., temperature gradient, solidification rate and cooling rate, were further calculated from the weld surface sections shown in Fig. 3.33. Results are summarised in Figs 3.35 - 3.37. Welding speed seems to have a distinct effect on solidification parameters, especially on weld cooling and solidification rates. The effect of weld sulphur content and the resulting weld shape variation in the weld surface section remains negligible. The calculated solidification parameters are noticed to fall in the same area as those evaluated from the corresponding welding experiments, c.f. Figs 3.4, 3.6 and 3.7. Distribution of the solidification parameters across the weld shows a reasonable correlation also with the distributions presented by David & Vitek (1991), c.f. Figs 1.1 and 1.4.

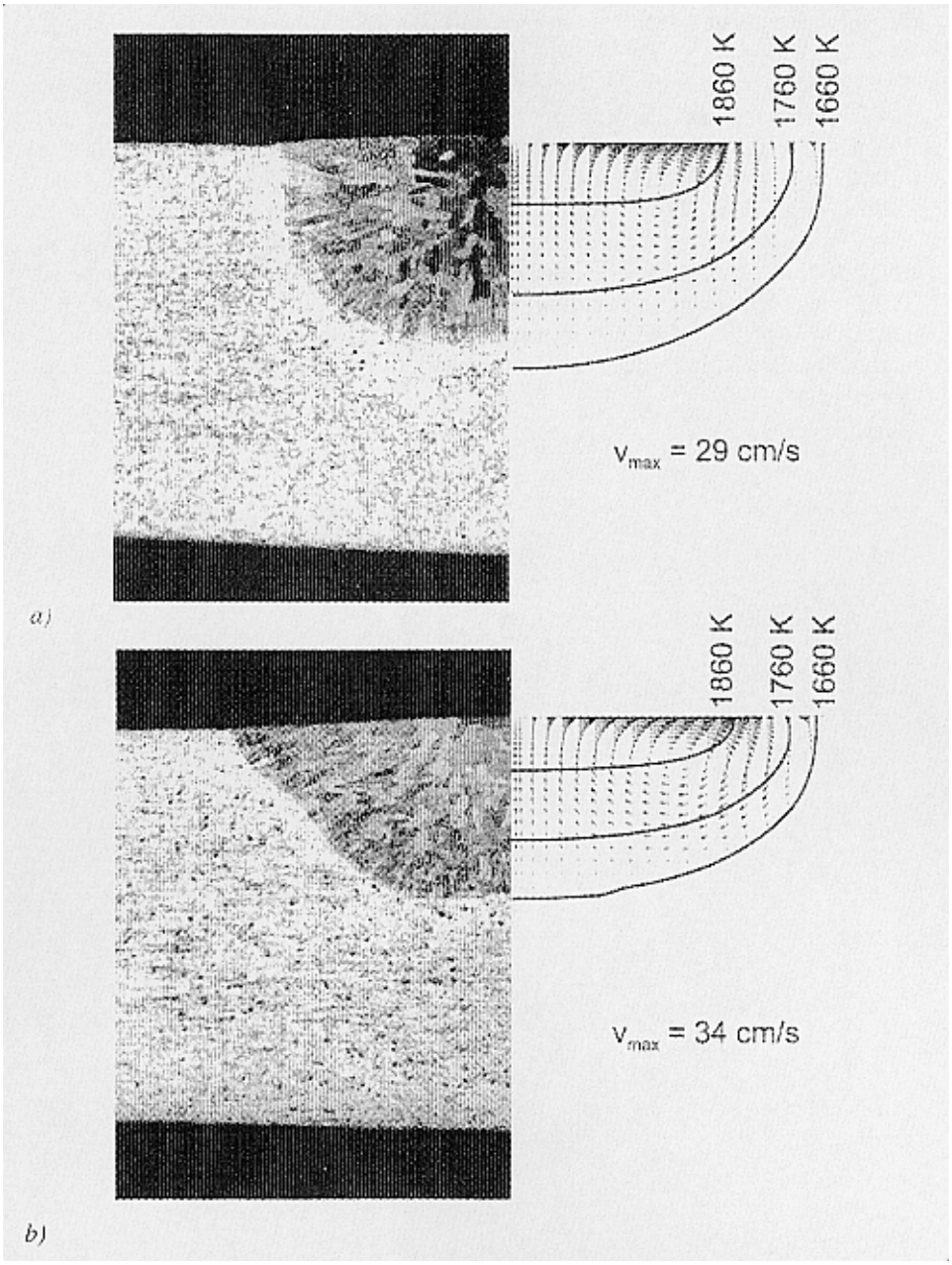

Fig. 3.32. Cross-section shapes of 304/2 welds from both macroscopic simulations and welding experiments. Welding speed 100 mm/min (a) and 200 mm/min (b). Simulations show the temperature isotherms for 1860, 1760 and 1660 K and the maximum flow rate of the weld pool (v_{max}).

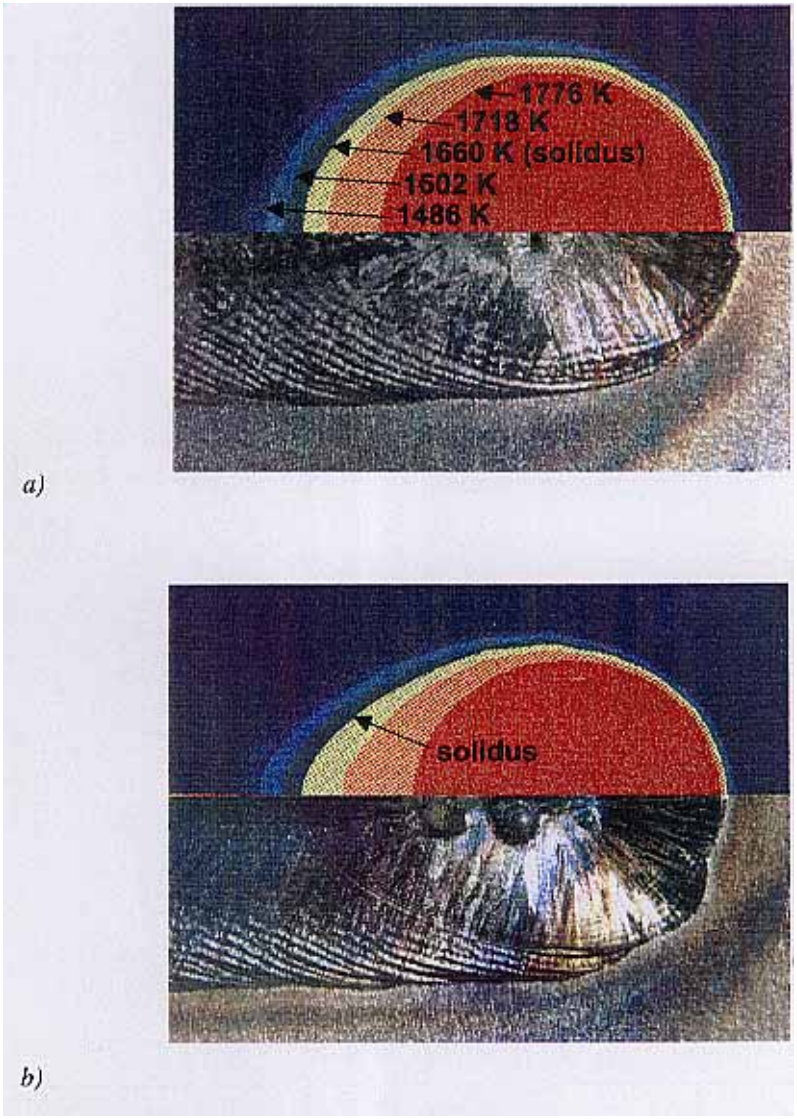

Fig. 3.33. Surface section shapes of 304/2 welds calculated by macroscopic simulations and compared to welding experiments. Welding speed 100 mm/min (a) and 200 mm/min (b).

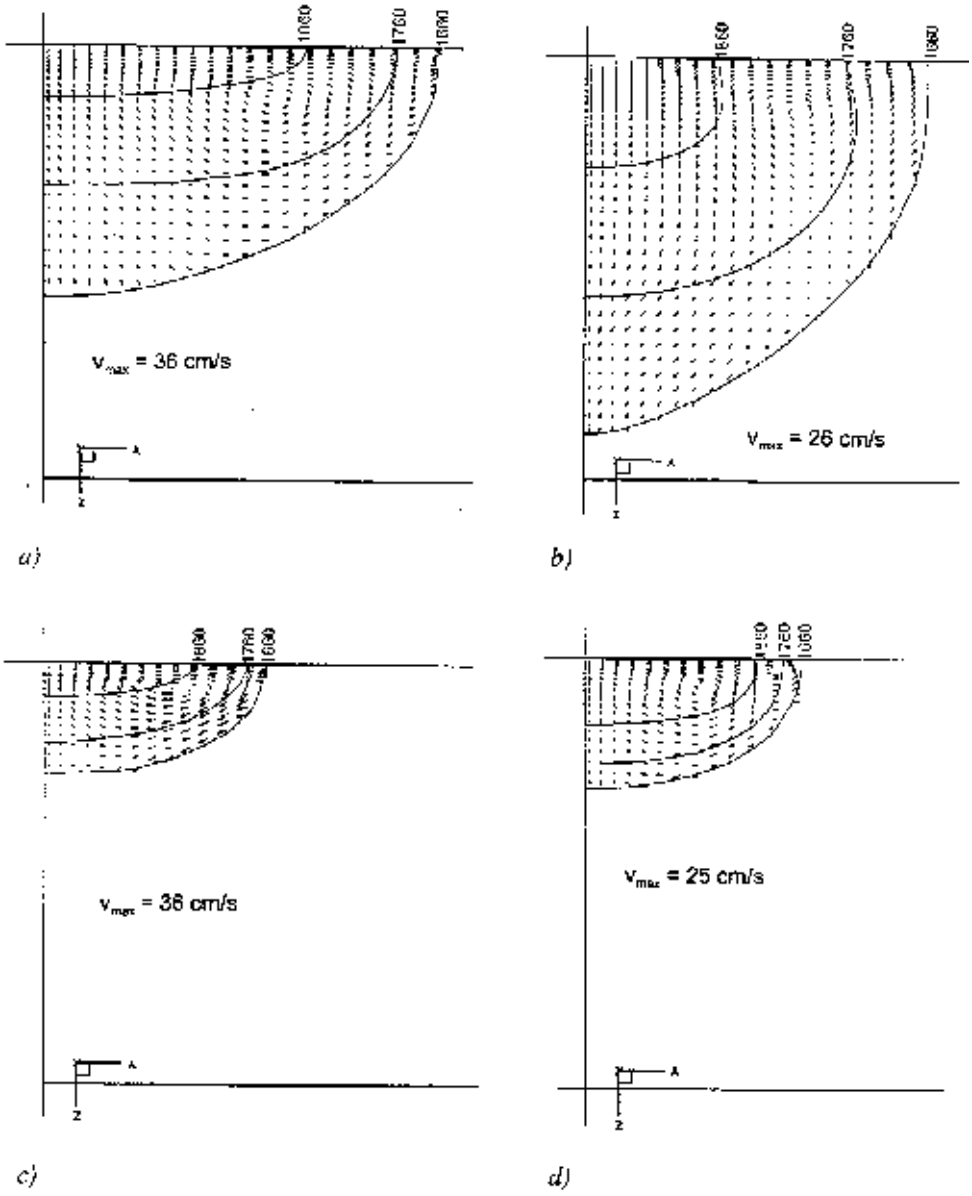

Fig. 3.34. Results of the macroscopic simulations expressed as temperature isotherms for 1860, 1760 and 1660 K and the maximum flow rate of the weld pool (v_{max}) showing the predicted effect of welding speed (v) and sulphur content (S) on the weld pool flow in cross-sections: v = 100 mm/min, S = 20 ppm (a); v = 100 mm/min, S = 150 pp (b); v = 400 mm/min, S = 20 ppm (c); v = 400 mm/min, S = 150 ppm (d).

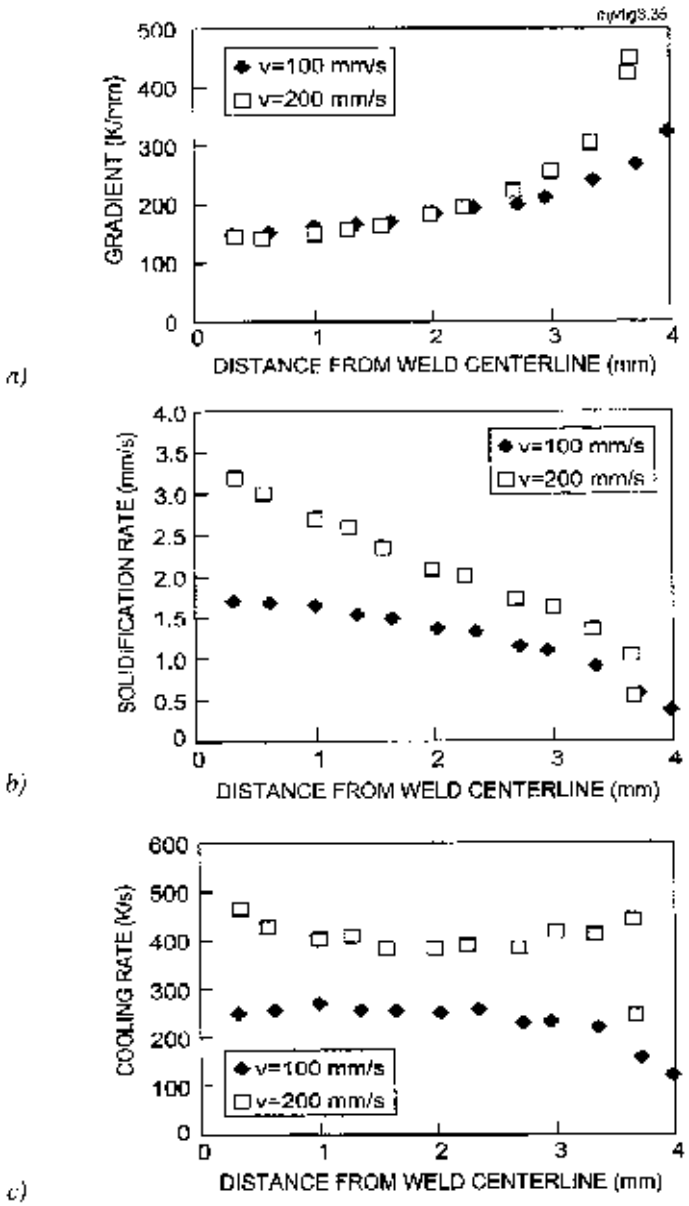

Fig 3.35. Calculated temperature gradient (a), solidification rate (b) and cooling rate (c) for GTA-welds with welding speeds of 100 and 200 mm/min.

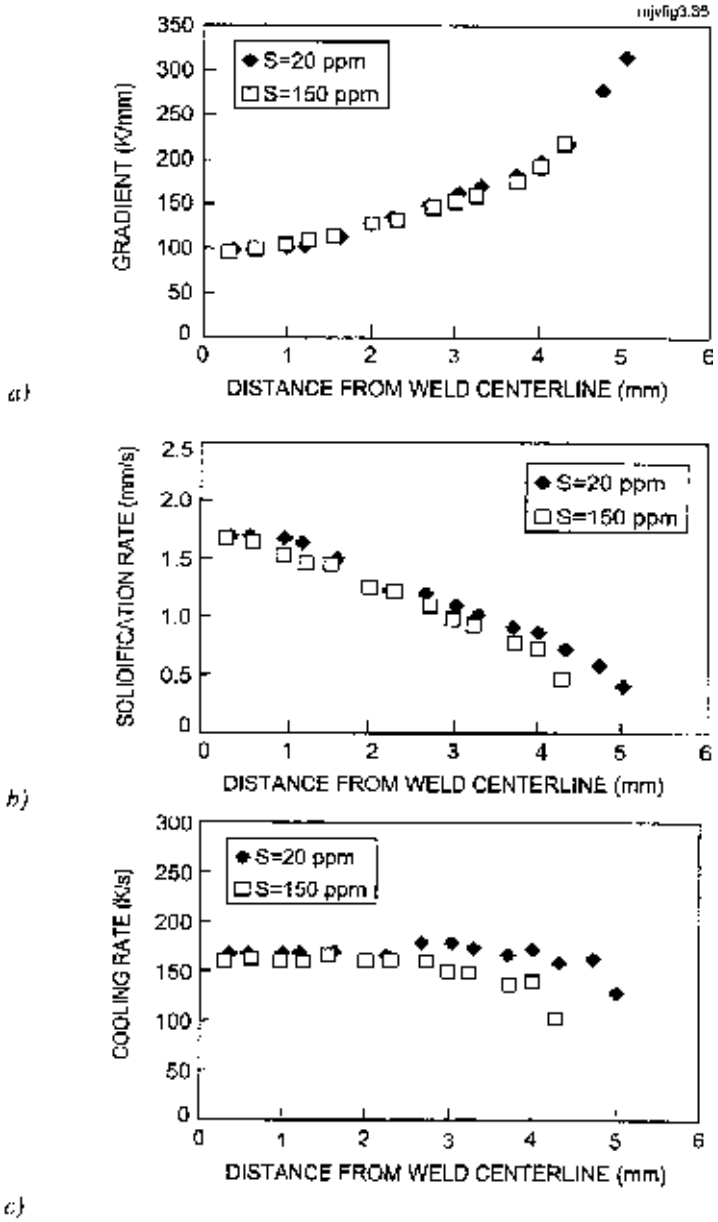

Fig. 3.36. Calculated effect of weld sulphur content and related weld shape variation (Fig. 3.34) on temperature gradient (a), solidification rate (b) and cooling rate (c) for GTA-welds with welding speed of 100 mm/min.

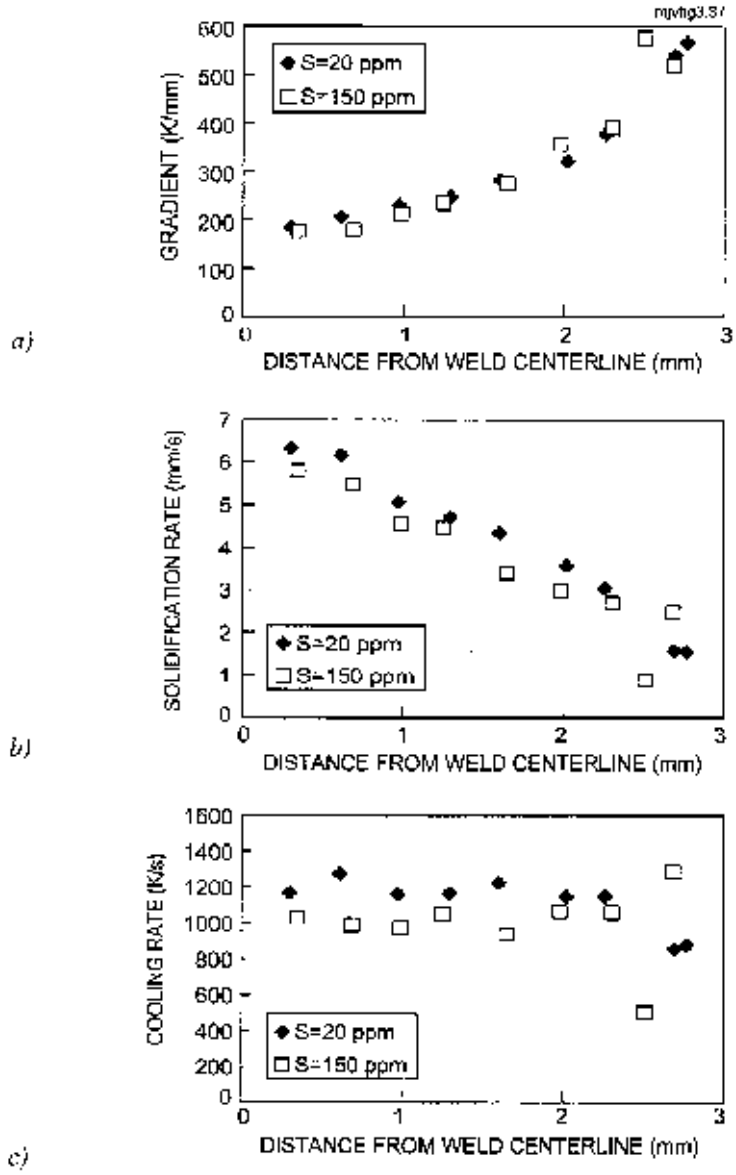

Fig. 3.37. Calculated effect of weld sulphur content and related weld shape variation (Fig. 3.34) on temperature gradient (a), solidification rate (b) and cooling rate (c) for GTA-welds with welding speed of 400 mm/min.

3.5.2 Microscopic simulations

Tip modelling

Dendrite tip modelling as described in Appendix 2 was applied to calculate solidification of constrained dendritic growth as a function of weld solidification parameters, i.e., solidification rate and temperature gradient. Partition coefficients needed in the calculations were first determined by the Thermocalc™ database with results shown in Table 3.3. The calculations were then carried out with a PC program developed for steels showing primary austenitic solidification. In addition, the CDGMS-model of Appendix 3 was applied in the prediction of the primary phase of solidification and the calculation of segregation at the dendrite tip of the steels studied.

Table 3.3. Equilibrium partition coefficients for Cr and Mo needed in the PC program. The values are determined by the Thermocalc™ database.

Steel	$\mathbf{k_{Cr}}$	$\mathbf{k_{Mo}}$
304/2	0.84	-
316/3	0.85	0.60
6Mo/1	0.84	0.64
6Mo/2	0.84	0.64

The three following approaches were used in the calculations:

- coupled macro-micro modelling based on solidification parameters obtained from the macroscopic simulations of GTA-welds, shown in Figs 3.35 - 3.37
- calculation of core composition as a function of average solidification rate and temperature gradient based on values determined from the weld experiments, c.f. Fig. 3.38
- prediction of the primary phase of solidification and calculation of segregation at the dendrite tip as a function of solidification rate by the CDGMS-model.

Results of the first series of simulations expressed as PRE(min/av) ratio of the weld metals are summarised in Figs 3.39 and 3.40. The magnitude of segregation seems to depend largely on the steel composition. This is seen from the calculations showing that the magnitude of segregation is highest for 6Mo/1 steel and lowest for the Mo-free steel 304/2. Increasing the welding speed from 100 to 200 mm/min seems to have only a slight effect on segregation behaviour, see Fig. 3.39. A somewhat more pronounced decrease in the segregation is produced by increasing the welding speed to 400 mm/min, c.f. Figs 3.40 a and b.

In addition to the dependence on steel composition and the effect of welding speed, the simulations predict that the segregation of the welds is slightly higher

close to the weld fusion line and decreases gradually towards the weld centerline. It is further noticed that the effect of weld shape variation produced by varying the sulphur content (Fig. 3.34) seems to have only a minor, if any, effect on segregation behaviour, see Fig. 3.40.

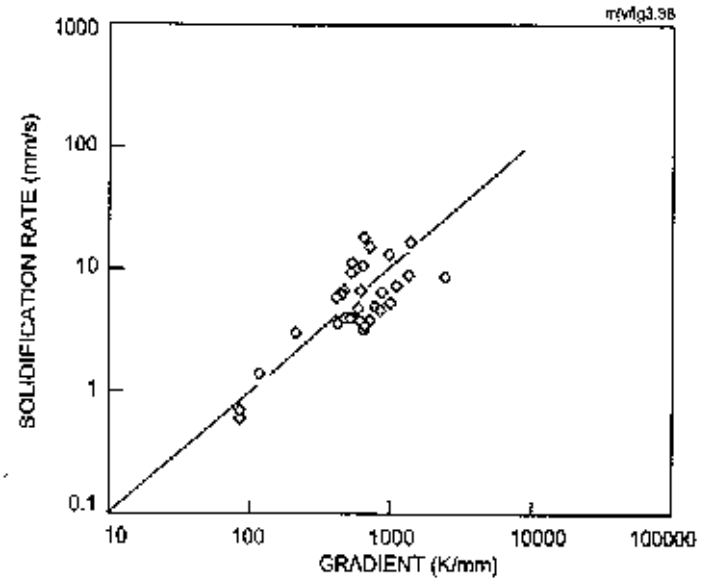

Fig. 3.38. Values of solidification rate (R) and temperature gradient (G) used in the microscopic simulations (line). The measured G-R values and determination of the line is based on experiments shown in Figs 3.6 and 3.7.

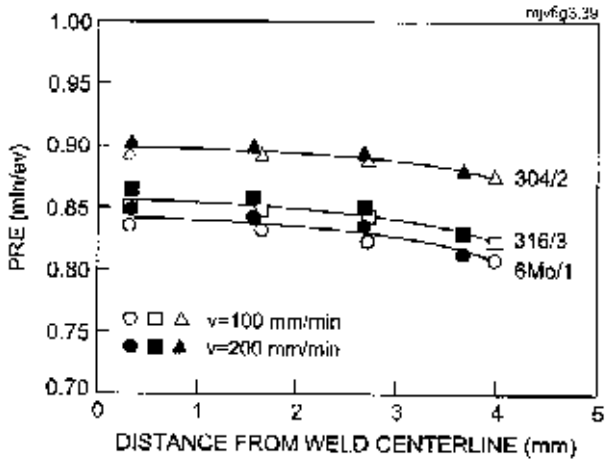

Fig. 3.39. Predicted effect of welding speed and steel composition on segregation behavior expressed as PRE(min/av) ratio. The results are based on combined macro-micro simulations with input data shown in Fig. 3.35.

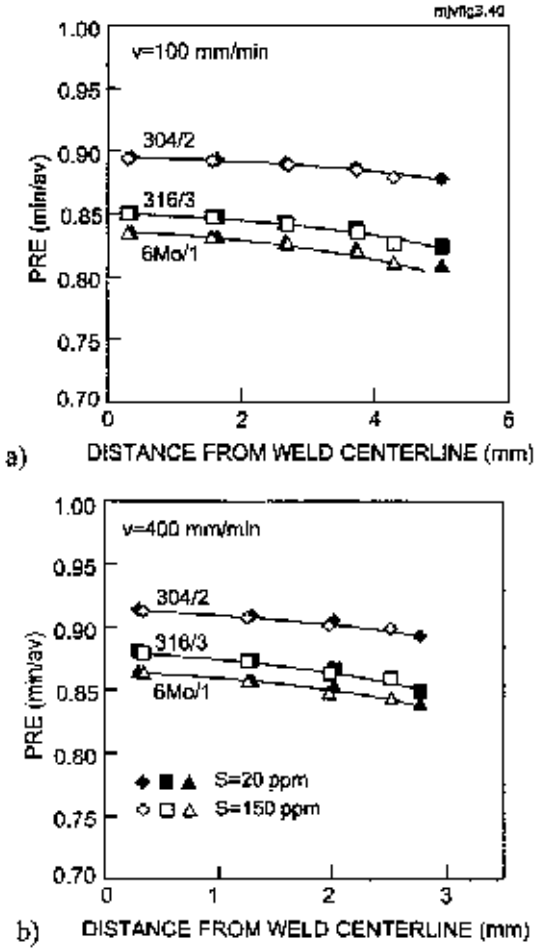

Fig. 3.40. Predicted effect of welding speed (a: 100 mm/min and b: 400 mm/min), weld shape variation (S = 20 ppm, S = 150 ppm) and steel composition on segregation behavior expressed as PRE(min/av) ratio. The results are based on combined macro-micro simulations with input data shown in Figs 3.36 and 3.37.

The second series of the microscopic simulations established the effect of increasing solidification rate and temperature gradient (see Fig. 3.38) on segregation behavior. The results are summarised by Figs 3.41 - 3.42. It is readily seen that the Cr- and Mo-contents at the dendrite tip constantly increase with increasing solidification rate in the range 0.1 to 100 mm/s. Calculations show reasonably good agreement with the experimental results shown in Figs 3.41 and 3.42. The calculations indicate that Mo segregates more strongly than Cr. The effect of velocity correction to the partition coefficient (see Appendix 2) seems to result in a slightly lower degree of heterogeneity for the highest solidification rates used. With solidification rates below 10 mm/s the velocity correction has, however, no practical effect on the predicted segregation behaviour.

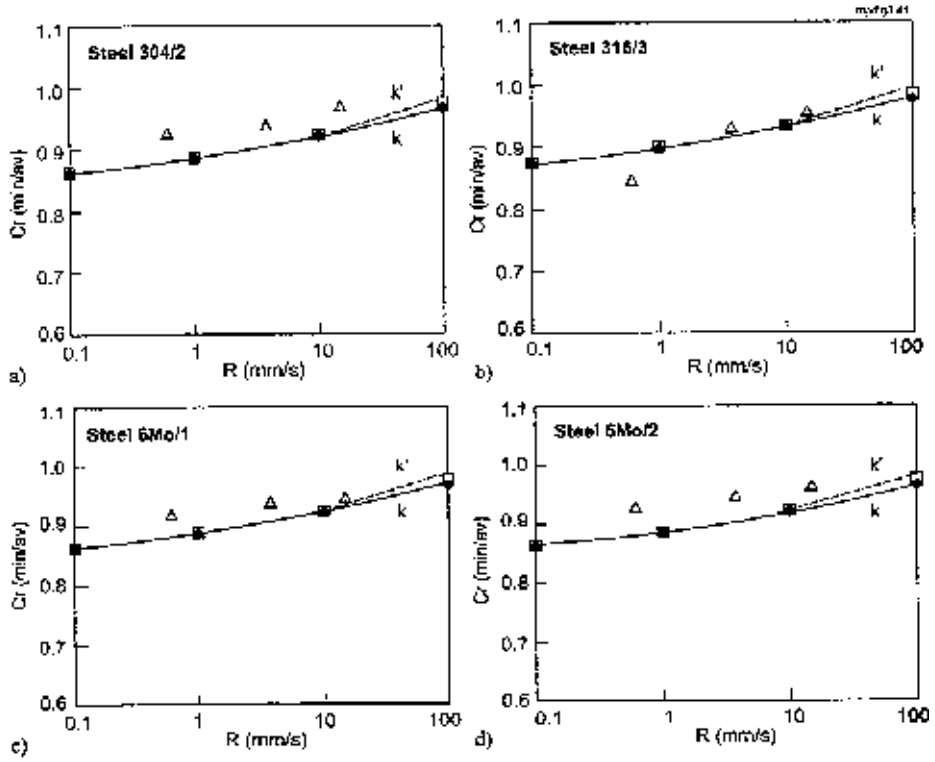

Fig. 3.41. Cr-enrichment at dendrite or cell tip as a function of solidification rate R. The symbols k and k' refer to equilibrium and velocity dependent partition ratios (Appendix 2), respectively. The calculations are represented by the lines and the measured values by the triangles.

Figure 3.43 summarises the results of the previous calculations showing the effect of solidification rate on the PRE(min/av)-ratio. As can be seen this ratio becomes lower for the Mo-alloyed steel grades than for the Mo-free steel 304/2. This is due to microsegregation of Mo. With higher solidification rates the difference between the steels studied remains smaller.

The third phase of the dendrite tip calculations included prediction of the solidification mode for the steels studied by using the CDGMS-model. The calculations are summarised as a function of solidification rate in Fig. 3.44. Primary ferritic solidification is predicted for steels 301, 304/1 and 316/1 with practically all solidification rates used in calculations. Steel 316/2 exhibits a change from primary ferritic to primary austenitic solidification with increasing solidification rate. The other steels 304/2, 316/3 as well as the 6% Mo alloyed grades show primary austenitic solidification over the whole solidification rate range studied.

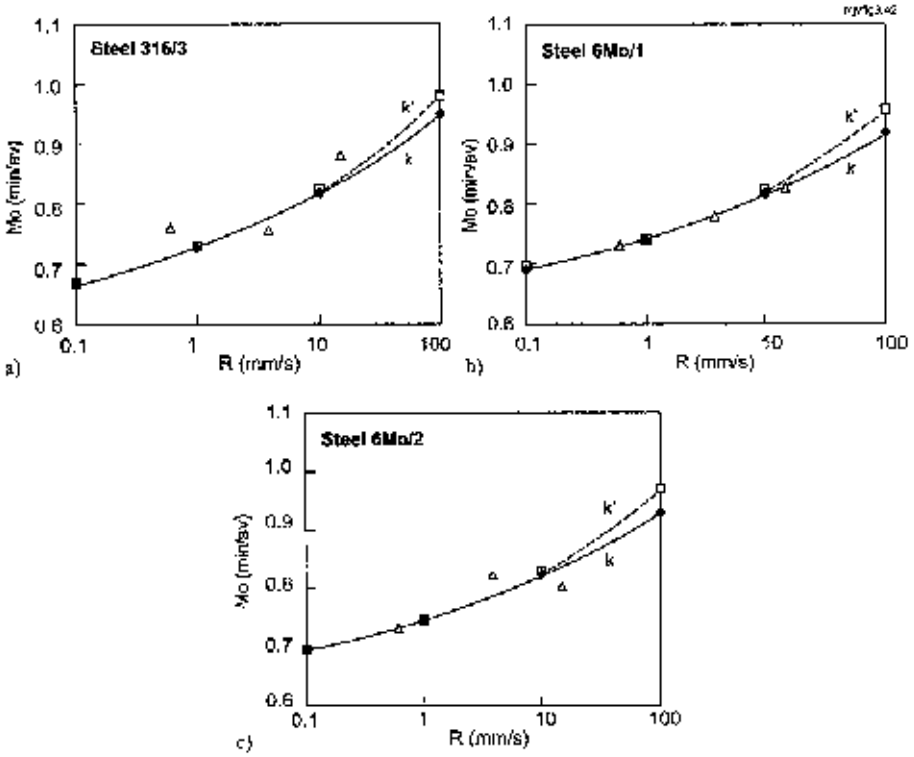

Fig. 3.42. Mo-enrichment at dendrite or cell tip as a function of solidification rate R. The designations correspond to Fig. 3.41.

Based on the results of the CDGMS-model the effect of solidification mode on segregation behavior is illustrated in Fig. 3.45. The calculations indicate that in low-speed welding, i.e., with low values of the solidification rate, primary ferritic solidification of steel 316/1 results in considerably less segregation of Cr and Mo than in the case of primary austenitic solidification of steel 316/3. With increasing the solidification rate austenitic solidification results in noticeable dendrite tip enrichment and produces a continually decreasing PRE(min/av) ratio. With solidification rates in excess of 10–20 mm/s the dendrite tip composition becomes almost equal in both solidification modes. It should, however, be noticed that these calculations compare segregation behaviour during solidification without considering solid state transformations after solidification.

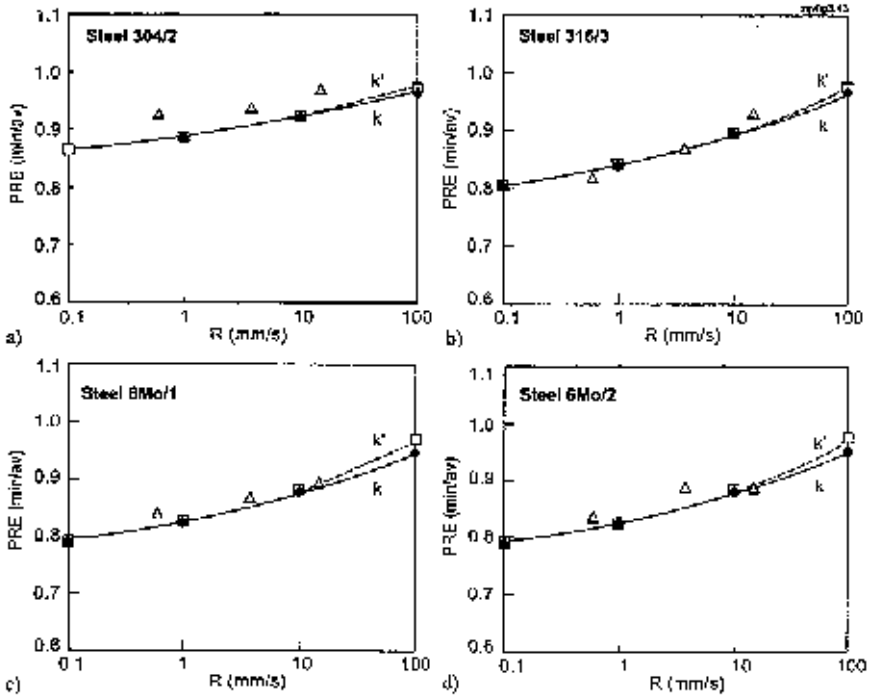

Fig. 3.43. PRE(min/av) ratio of dendrite or cell tip as a function of solidification rate R. Nitrogen is added to the PRE-index (PRE = Cr + 3.3Mo + 13N) as average value. The designations correspond to Fig. 3.41.

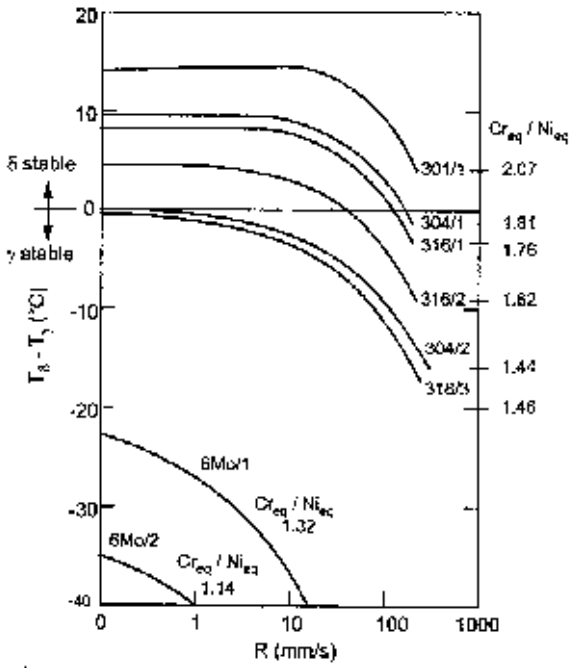

Fig. 3.44. Predicted phase stabilities calculated by the CDGMS-model for the steels studied as a function of weld solidification rate.

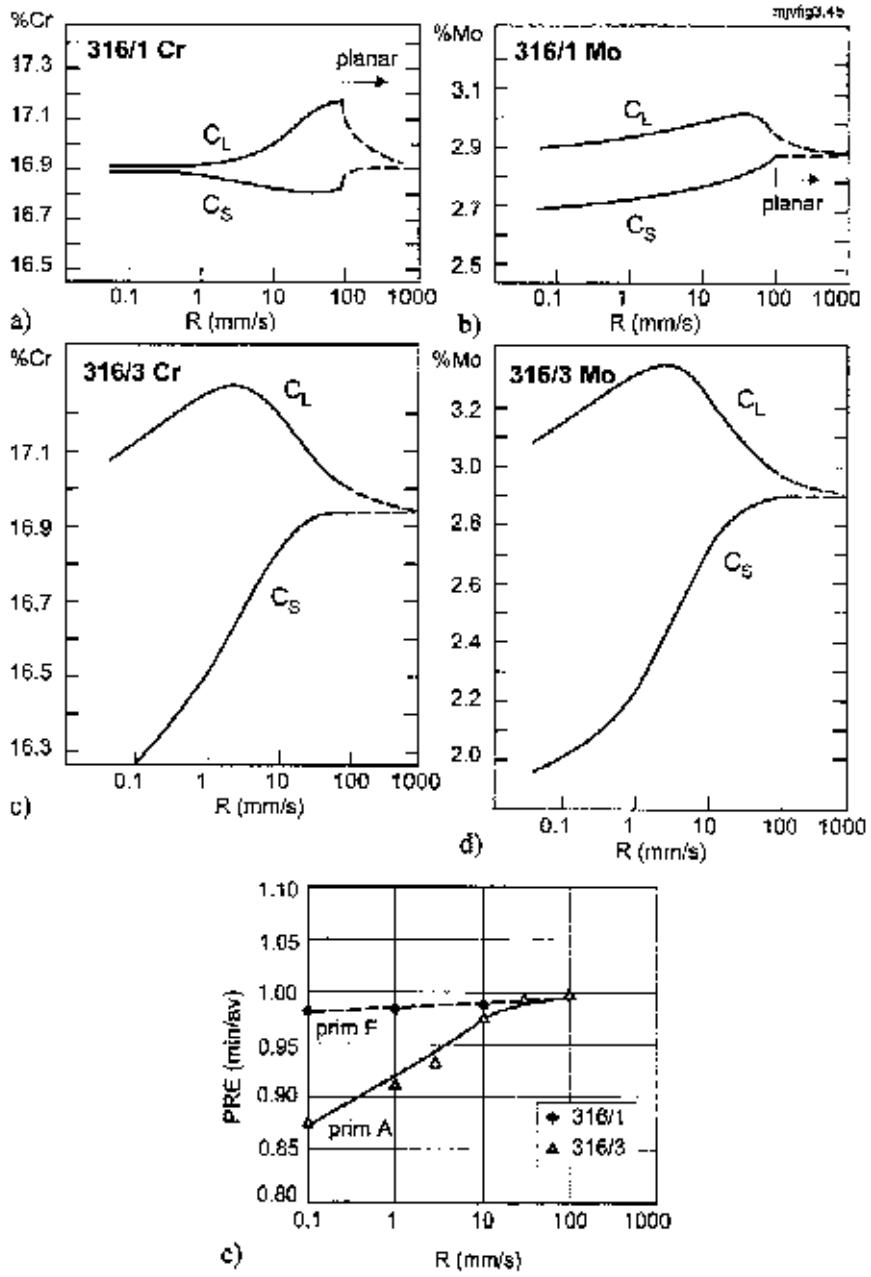

Fig. 3.45. Compositional development of dendrite tip during primary ferritic solidification of steel 316/1 and primary austenitic solidification of steel 316/3 predicted by the CDGMS-model as a function of solidification rate. Steel 316/1: Cr (a), Mo (b). Steel 316/3: Cr (c), Mo (d). PRE(min/av) ratio for both steels (e).

Interdendritic solidification modelling

Solute redistribution in the interdendritic direction was calculated by (1) exploiting the computer program described in Appendix 4 and (2) using the model developed by Nippon Steel Co., see Appendix 5. The calculations of phase (1) could be used in evaluating the welds showing primary austenitic solidification. In phase (2) the segregation behaviour taking place in primary austenitic and primary ferritic solidification could be compared among the steels studied.

The results of phase (1) simulations are summarised in Figs 3.46 and 3.47. In these calculations the results obtained by macroscopic simulations of the low-speed GTA-weld (v = 100 mm/min, see Fig. 3.35) have been used as input data. Results show that the calculations applying the TIP-ID connection yield similar predictions for all solidification models used.[4] The calculated segregation profiles also match reasonably well the EPMA measurements of the weld metals. In the final stage of solidification all the models, however, systematically predict higher enrichment of alloying elements than is measured experimentally.

The effect of solidification conditions on solute redistribution in the interdendritic direction was further simulated as a function of solidification rate. In these simulations the solidification rate was increased as shown in Fig. 3.38. These simulations are in correspondence with the dendrite tip modelling (Figs 3.41 - 3.43), showing now the effect of increasing solidification rate in the transverse direction. It is readily seen from the results shown in Fig. 3.48 that increasing solidification rate decreases the magnitude of microsegregation also in the interdendritic direction when the TIP-ID linking is applied. By increasing the solidification rate from 1 mm/s up to 10 mm/s, a slight increase in the PRE(local/av) ratio is observed. The magnitude of segregation further decreases as the solidification rate goes up to 50 mm/s. With the highest solidification rate of 100 mm/s the local PRE value becomes close to the base metal level.

For comparison, the interdendritic calculations were carried out using the ID-models without connection to the dendrite tip model. In this case the composition of solid in the beginning of solidification is calculated directly from the equilibrium partition coefficients (Table 3.3). The results of these calculations, shown in Fig. 3.48 (lower curves), indicate that the composition profiles calculated by this means do not show any noticeable dependence on the solidification rate. Consequently, the deviation from the prediction of the TIP-ID model continually increases with the solidification rate.

[4] Ohnaka, Brody-Flemings (B-F) and Giovanola-Kurz (G-K), see Appendix 4.

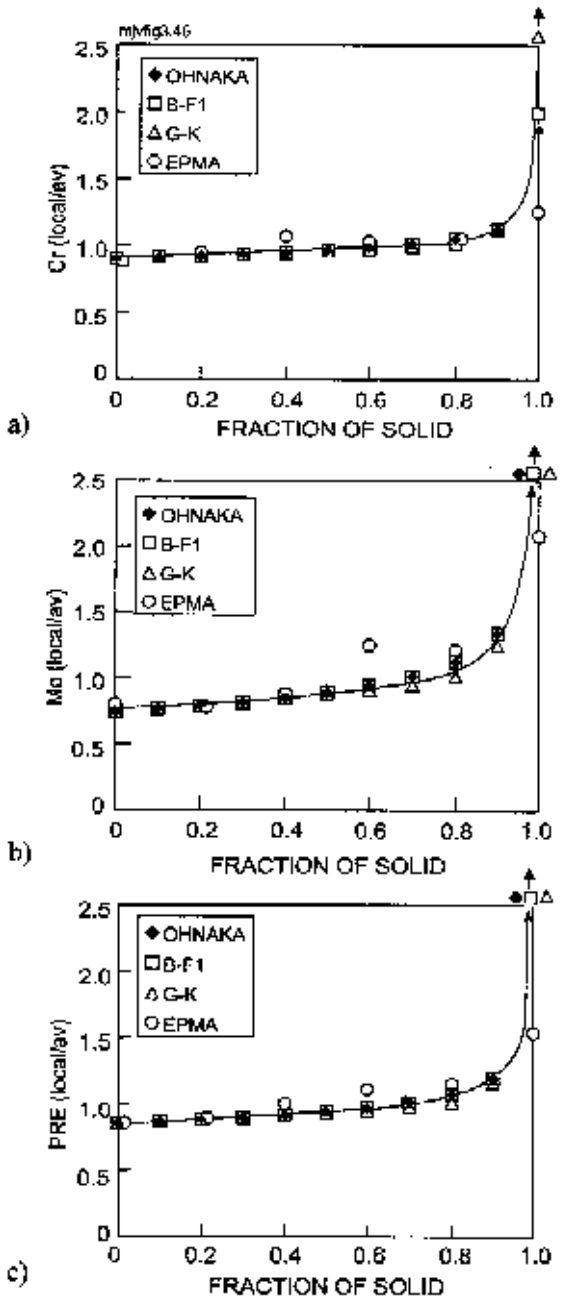

Fig. 3.46. Predicted solute redistribution for Cr (a), Mo (b) and PRE (c) for low-speed GTA-welds of 316/3 steel applying the TIP-ID model and comparison of the calculations to the results of EPMA line scan analyses. The solidification parameters used as input data have been taken from the macroscopic simulations for v = 100 mm/min using values calculated for ¼ weld width region (Fig. 3.35). The microscopic models applied (Ohnaka, B-F1 and G-K) are explained in Appendix 4.

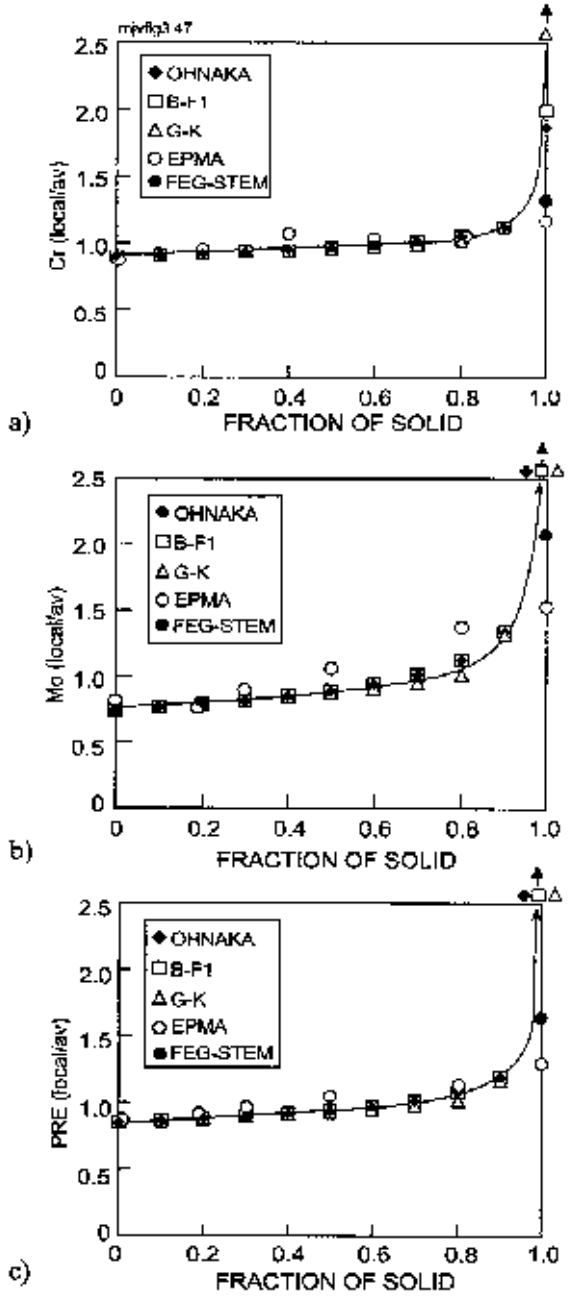

Fig. 3.47. Predicted solute redistribution for Cr (a), Mo (b) and PRE (c) for low-speed GTA-welds of steel 6Mo/1 applying the TIP-ID model and comparison of the calculations to the results of EPMA and FEG-STEM analyses. The solidification parameters used as input data have been taken from the macroscopic simulations for v = 100 mm/min using values calculated for ¼ weld width region (Fig. 3.35). The models applied (Ohnaka, B-F1 and G-K) are explained in Appendix 4.

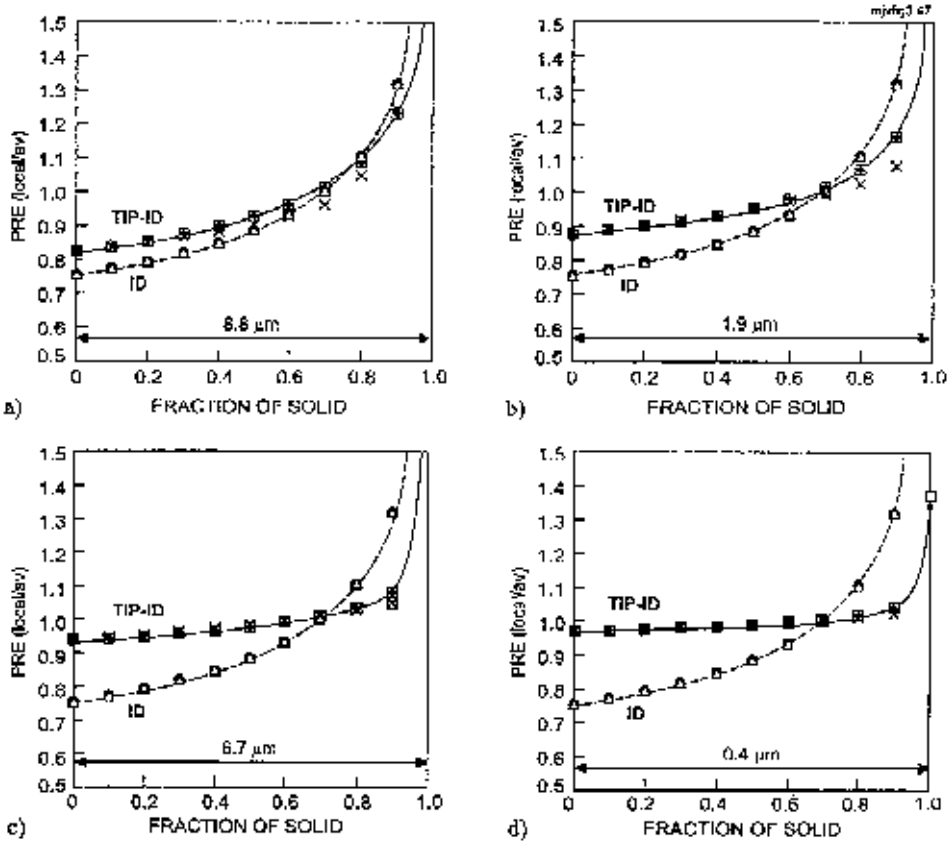

Fig. 3.48. Solute redistribution in the interdendritic direction calculated by TIP-ID model (upper curves) and by the ID-model using equilibrium partition coefficients (see Table 3.3) in calculation of input analysis (lower curves). The steel studied is 6Mo/1. The curves are based on calculations according to the models specified in Appendix 4. The solidification rates are 1 mm/s (a), 10 mm/s (b), 50 mm/s (c) and 100 mm/s (d). The calculations are based on use of the velocity corrected partition coefficient k'. The distance in µm refers to half of primary dendrite arm spacing.

Results of simulation phase (2) that utilised the model of Nippon Steel Co. are shown in Figs 3.49 and 3.50 for primary ferritic and primary austenitic solidification modes, respectively. In case of primary ferritic solidification the model predicts segregation of Cr and Mo towards the interdendritic region, c.f. Fig. 3.49a. Segregation of Ni and N remains weaker. As the solidification proceeds, second phase austenite accompanied by an increase in Ni and N contents is formed. Correspondingly, the concentrations of Cr and Mo remain lower than in ferrite. During further post-solidification cooling austenite grows into ferrite and changes the segregation profile as shown in Fig. 3.49b. As a result,

a strong enrichment of Cr and Mo is noticed at the δ/γ interface. The distribution of Ni becomes opposite. Nitrogen is enriched in austenite, as expected.

In case of primary austenitic solidification of weld 6Mo/1 (Fig. 3.50a) the segregation of Cr, Mo and N takes place to the interdendritic direction. Ni, however, shows a slight tendency to segregate towards the dendrite cores. The solidification terminates as ferrite which is enriched in Cr and Mo and depleted in Ni and N. Post-solidification cooling further increases the partitioning of these elements between austenite and ferrite, see Fig. 3.50b.

The distribution of PRE expressed as PRE(local/av) ratios are shown in Fig. 3.51. The model predicts a noticeable difference in the distribution of this ratio between primary austenitic and primary ferritic solidification. In primary ferritic solidification the δ/γ interface is associated with a distinct drop in PRE-distribution. A further decrease in the PRE-value takes place in the austenite phase where the PRE(local/av) ratio falls below 1.

In case of primary austenitic solidification the PRE-values become the lowest at the dendrite cores which is due to segregation of Cr, Mo and N towards interdendritic region. For this reason, the lowest value of the PRE(local/av) ratio becomes lower in primary austenitic welds than in primary ferritic welds. It is noticeable that in primary austenitic welds the local PRE-value remains below the base metal level up to distance ratios as high as about 80% of the calculation regime, see Fig. 3.51b.

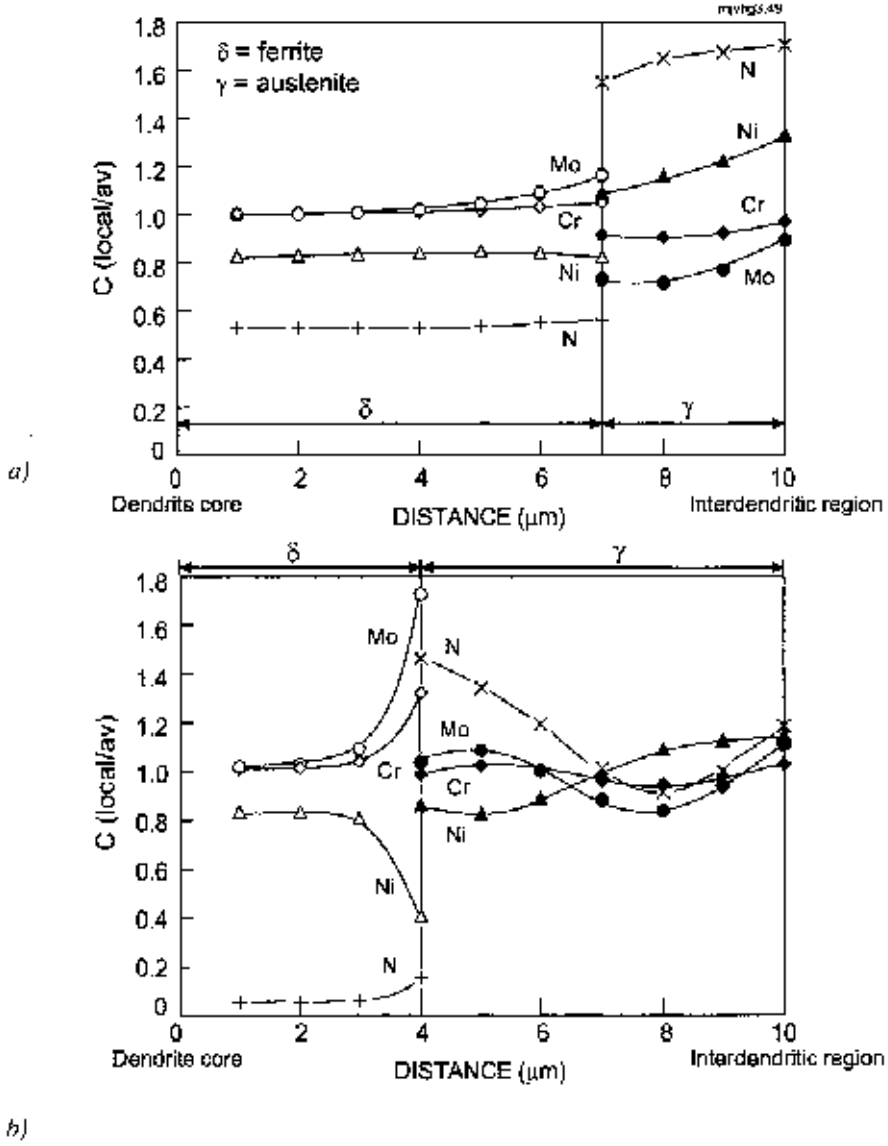

Fig. 3.49. Predicted segregation profiles of Cr, Ni, Mo and N just after solidification (a) and at temperature of 1273 K (b) for steel 316/1 showing primary ferritic solidification. Arc power of 1580 W and solidification rate of 1 mm/s have been used as input parameters to the simulation of GTA-welding.

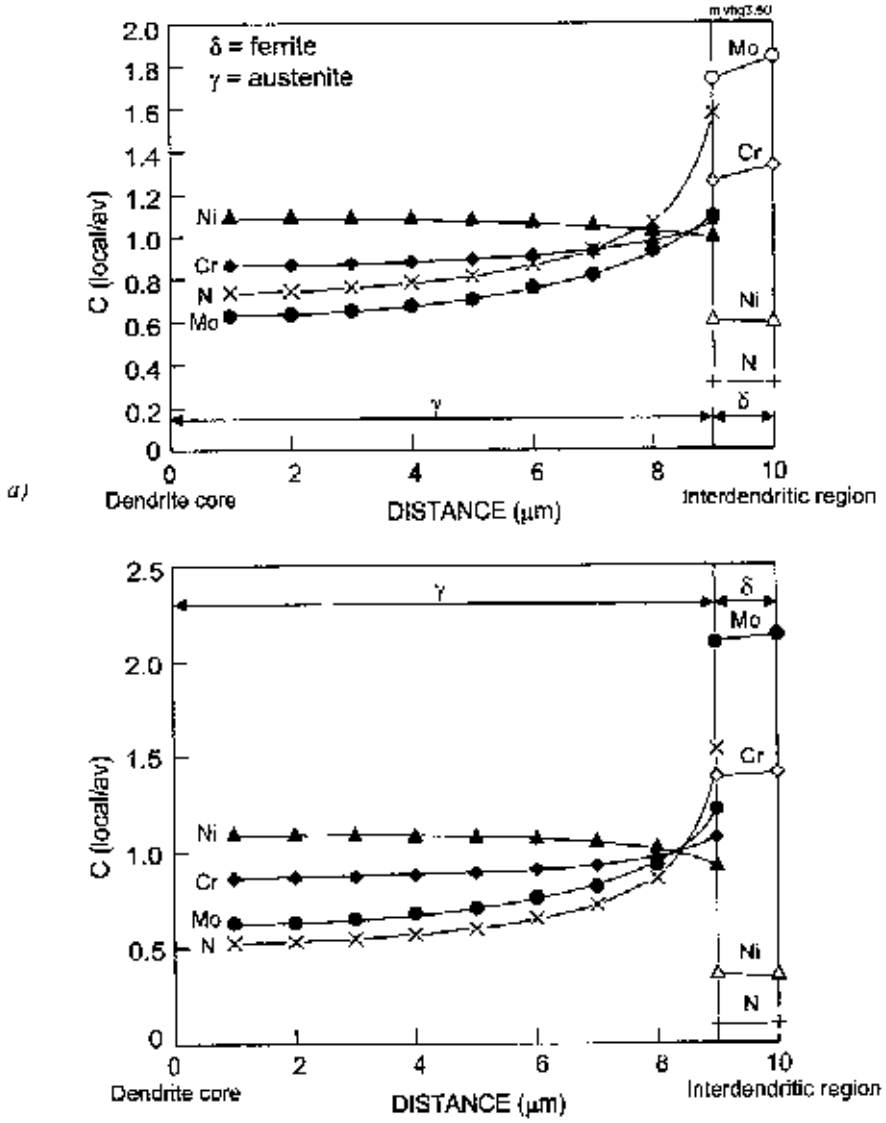

Fig. 3.50. Predicted segregation profiles of Cr, Ni, Mo and N just after solidification (a) and at temperature of 1273 K (b) for steel 6Mo/1 showing primary austenitic solidification. Arc power of 1580 W and solidification rate of 1 mm/s have been used as input parameters to the simulation of GTA-welding.

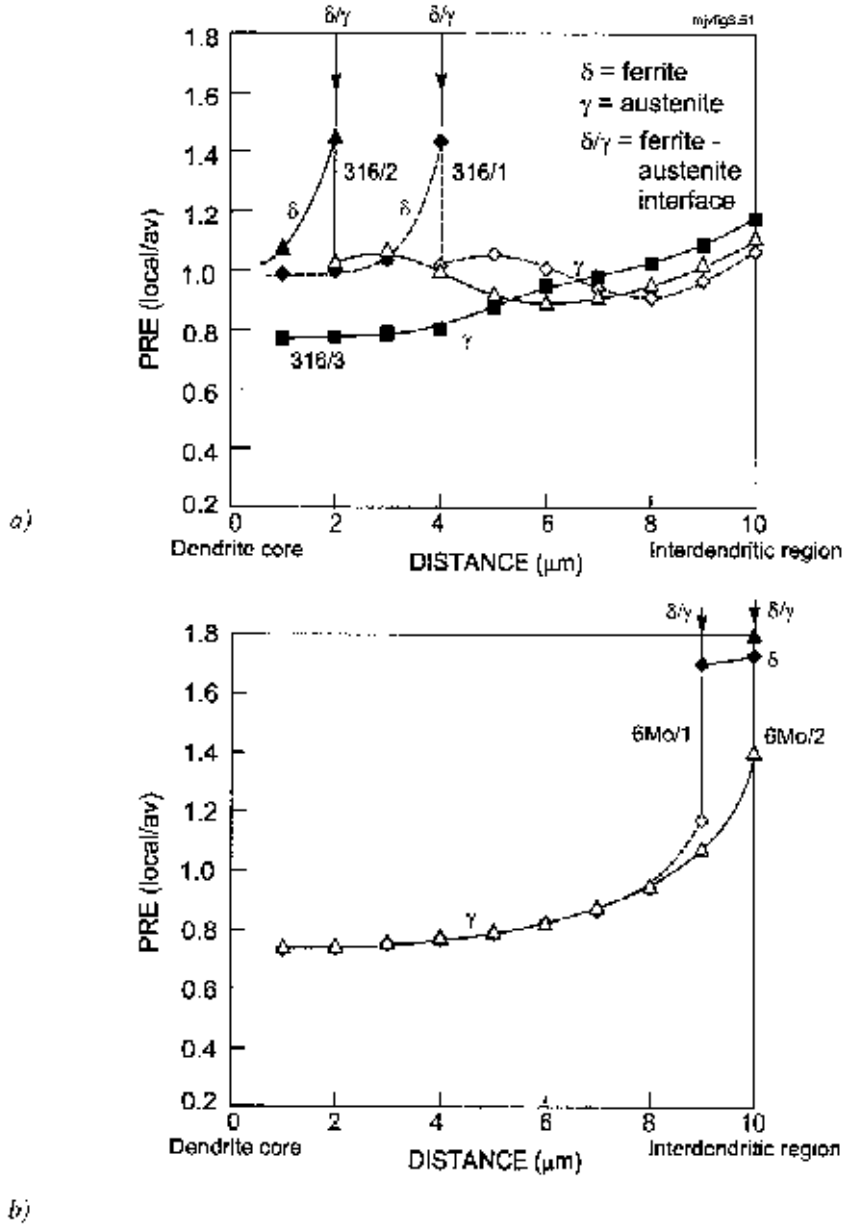

Fig. 3.51. PRE(local/av) distribution profiles for 316 steels (a) and 6% Mo steels (b) based on calculated segregation profiles of Cr, Mo and N. The pitting index of PRE = Cr + 3.3Mo + 13N has been used. Arc power of 1580 W and solidification rate of 1 mm/s have been used as input parameters to the simulation of GTA-welding.

4. Discussion

The discussion of the results is divided to five main parts. First, the behaviour and validity of the models used are evaluated. The predictability of pitting corrosion resistance by the present models is then assessed. This is succeeded by evaluation of the experimental procedures. Finally, remarks on needs for future development and applicability of the results are discussed.

4.1 Assessment of the present models

4.1.1 Macroscopic modelling

Good correlation between the calculated and experimental weld shape shown in Figs 3.32 and 3.33 supports the validity of the WELD3D model used in the cases studied. Agreement between calculations and experiments indicated that the simulation of electromagnetic, buoyancy and surface tension forces gives a sufficiently accurate prediction on the weld pool flow and resulting fusion zone shape. The role of plasma shear force, that was excluded from the calculations, obviously plays only a negligible role in the cases studied. This arises from the short arc length of 2 mm (Table 2.2) applied in the welding experiments as well as in the simulations. This claim is supported by the observations of Matsunawa et al. (1987) showing that the role of plasma shear forces becomes important only with long electric arcs.

The results of Figs 3.32 and 3.34 show that the maximum flow rate caused by the previous three forces ranges from 25 to 36 cm/s. These values correspond well to recent studies of other authors where flow rates ranging from 20 to 40 cm/s have been calculated for moving heat sources (Mundra et al. 1997a, b, Hong et al. 1998). With these flow rates the effect of convective heat transfer becomes an important factor in determining the weld pool shape. This can be assessed by calculating the dimensionless Peclet number (P_e) which is a measure of the relative magnitudes of convective and conductive heat transfers and is given by the following equation (DebRoy & David 1995):

$$P_e = \frac{v_{max}\rho c L}{\lambda} \tag{22}$$

where v_{max} is maximum flow rate in the weld pool (see Figs 3.32 and 3.34), ρ is the density of molten weld metal, c the specific heat at constant pressure, λ is the thermal conductivity of the melt and L is the characteristic length that can be taken as the depth of the weld pool. When the Peclet number is much larger than one, the heat transport occurs primarily by convection, and heat conduction in the weld pool is of secondary importance. For the cases studied[5] the Peclet number varied from 54 to 187 indicating that the heat transport of the present weld pools is essentially convective and the role of conduction in the weld pool region is, thus,

[5] ρ = 7200 kg/m^3, c = 837 J/(kgK), λ = 42 W/(mK) and L = weld depth taken from Figs 3.31 and 3.33 (DebRoy & David 1995).

negligible. In the solid state heat transfer by conduction becomes, however, important. This is why the thermal conductivity of the solid and plate dimensions are also of great importance in determining the size of the molten pool (David & DebRoy 1995).

Concerning pool flow directions and the resulting fusion zone shape, the macroscopic simulations show a good agreement with the observations of other authors (Heiple & Roper 1982, Zacharia et al. 1989c, 1991, Winkler et al. 1997). It has been suggested that the surface tension force direction changes from outward to inward when the sulphur content exceeds 50 - 60 ppm (Mills & Keene 1990, Scheller et al. 1995). A similar trend is observed in the present simulations having a low welding speed of 100 mm/min, c.f. Fig. 3.34a and b. With a welding speed of 400 mm/min (Figs 3.34c, d) the pool flow direction, however, remains outward directed with both low and high sulphur levels. This is explained by the lower width of the high-speed welds with respect to arc radius. Consequently, the main portion of the weld pool is located below the arc, which due to higher peak temperatures results in negative temperature gradient of surface tension irrespective of sulphur content as demonstrated by McNallan & DebRoy (1991).

The main purpose of using the WELD3D model in the present study was to predict the solidification parameters, i.e., cooling rate, temperature gradient and solidification rate across the weld surface as shown in Figs 3.35 - 3.37. The distribution of these parameters across the solidifying weld show a reasonable agreement with the data presented by David & Vitek (1991), see Fig. 1.1. Agreeably the calculations demonstrate that the cooling and solidification rates increase as solidification proceeds from fusion line to weld centerline, whereas the values of the temperature gradient change in an opposite direction.

The accuracy of the WELD3D model can be further assessed by comparing the calculated solidification parameters to those measured or analytically calculated. Concerning weld cooling rates Fig. 4.1 demonstrates a good agreement between the calculated and measured values. This is, especially, true for values calculated by WELD3D for weld centerline and ¼ width regions, whereas the values calculated for the fusion line regions fall somewhat below the measured or analytically calculated values. This is in consistence with the cooling rate measurements that were performed by immersing thermocouples into the weld pool central region. The value of the thermal efficiency may still have an effect on the compatibility of the calculated and measured cooling rates. Reasonably good agreement with the thermocouple measurements, however, indicates that the efficiency of 0.75 chosen according to Smartt (1990) is of the correct order of magnitude.

Reasonable correlation between solidification rate and temperature gradient was also obtained, see Figs 4.2 and 4.3, respectively. With low welding speed of 100 mm/min the results show a good compatibility with the welding experiments of Suutala (1981). With increasing the welding speed to 200 and 400 mm/min the solidification rate seems, however, to show slightly higher values than those measured experimentally. This may arise from differences in the calculated and actual weld pool shapes. It is possible that in reality the pool of a high-speed weld

becomes more elongated than predicted which results in too small an angle θ and, thus, too high an estimate of solidification rate. The difference may originate also from incompatibility in the physical properties such as viscosity and thermal conductivity of the weld pool. In the welding speed range of the present WELD3D simulations the difference shown in Fig. 4.2 remains, however, reasonably small.

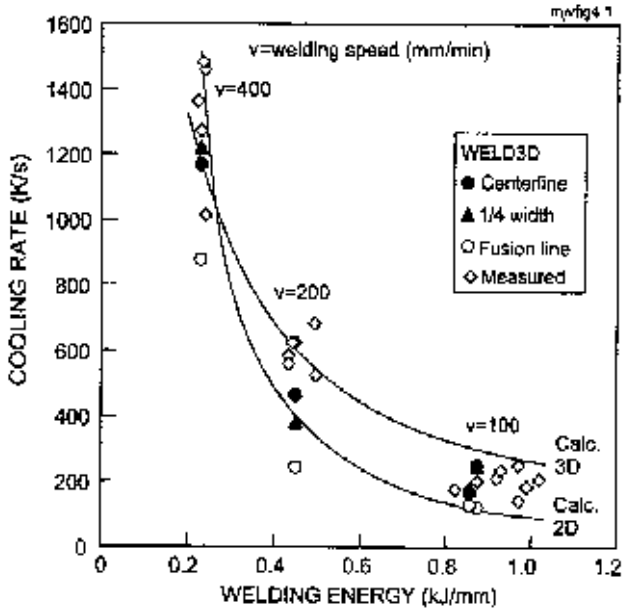

Fig. 4.1. Comparison of cooling rates calculated by WELD3D to those measured by thermocouples, c.f. Figs 3.1 and 3.2. The cooling rates are calculated with a thermal efficiency of 0.75.

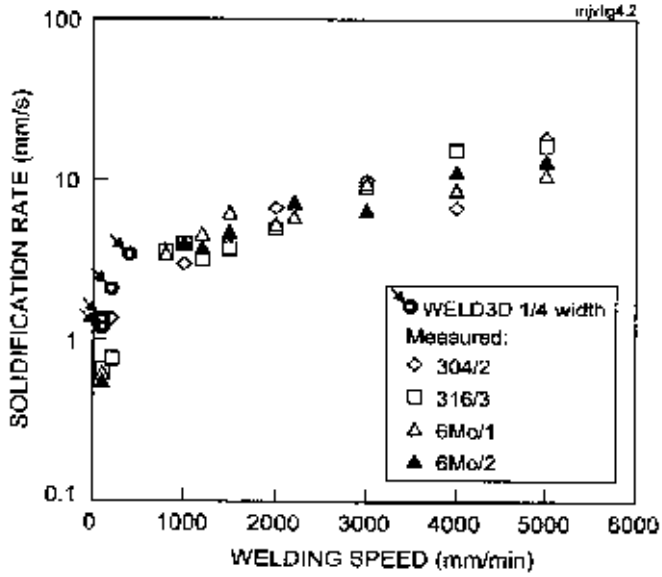

Fig. 4.2. Comparison of solidification rates calculated by WELD3D to those determined from the predicted weld pool geometry, c.f. Fig. 3.6.

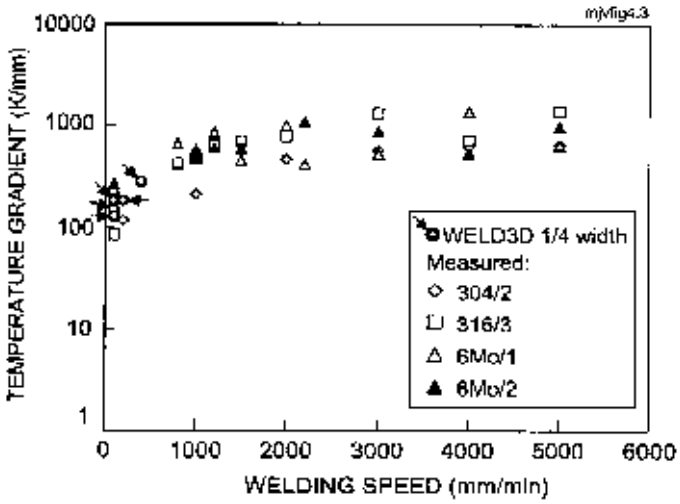

Fig. 4.3. Comparison of temperature gradients calculated by WELD3D to those determined experimentally, c.f. Fig. 3.7.

4.1.2 Dendrite tip modelling

The combined macro-micro simulations representing welding speed range of conventional GTAW gave a clear indication on the effect of steel composition on segregation behaviour in the direction of advancing dendrite tip, see Figs 3.39 and 3.40. Results indicated that the effect of welding speed is also of some importance. Increasing the welding speed, from 100 to 200 and further to 400 mm/min is, however, insufficient to cause a substantial decrease in microsegregation. This is explained by the fact that such an increase has only a marginal effect on the solidification rate that is the main parameter affecting solute redistribution (see Fig. 4.2 and Appendix 2, equation A2.1).

Results of the macro-micro simulations further proposed that the weld surface close to the fusion line may become slightly more susceptible to pitting corrosion than the central region of the weld metal. This trend stems from the slower solidification rate close to the weld fusion line (Figs 3.35 - 3.37) which, according to the dendrite tip model should produce slightly higher microsegregation at this region. Neither the EPMA line scan analyses nor the corrosion tests validate this indication obtained by simulation, however. The difference in behaviour between the model and the experiments may arise from the fact that the macroscopic model oversimplifies the grain growth phenomena by assuming that grain growth always occurs normal to the weld solidification front. This simplification assumes that dendrite packets always grow at a constant θ-angle and, thus, also a constant solidification rate exists at fixed distances from the weld fusion line. A considerable variation in grain growth direction does, however, exist in real welds as stated in chapter 1.2.2. Therefore, the segregation behaviour of real welds exhibits much more statistical scatter than do the simulated welds. On the other

hand, the accuracy of the EPMA line scan analyses may be insufficient to detect the effect of local solidification rate variations on segregation. In future studies line scan analyses as a function of θ angle would reveal more detailed information on this topic. The use of FEG-STEM-microscopy leading to considerably better analysing accuracy would also be of importance to verify the previous indications obtained by modelling.

The effect of weld shape on solidification parameters was, further, demonstrated by varying the sulphur content of the welds. Weld shape variations with constant parameters were, however, shown to have only a negligible effect on solidification parameters and, hence, on segregation behaviour. Consequently, weld shape variations caused by variable weld chemistry can be regarded as of secondary importance as long as the welding parameters are kept constant. Hence, the macroscopic modelling indicates that the solidification parameters depend mainly on the welding parameters such as welding speed and resulting heat input.

The predictability and accuracy of the macro-micro simulations can be judged by comparing the simulation results with experimental measurements. Concerning Cr- and Mo-contents having a direct effect on PRE-index, a reasonably good agreement exists between the simulations and experiments. This is seen by comparing the calculated and measured PRE(local/av) ratios of dendrite cores (see Figs 3.46 and 3.47 for $f_s = 0$) which are known to dominate the pitting corrosion behaviour of welds showing primary austenitic solidification (Garner 1982 and 1983, Ogawa et al. 1982, Marshall & Gooch 1993). Hence, the macro-micro approach seems to yield reliable results concerning primary austenitic solidification that is typical of high-alloyed austenitic stainless steels.

The effect of welding speed and resulting solidification parameters were, further, studied by the dendrite tip model for welds showing primary austenitic solidification. The main purpose of these studies was to demonstrate the effect of welding speed that is substantially higher than used in the macro-micro simulations. These calculations indicate that weld inhomogeneity continuously decreases with increasing solidification rate, see Figs 3.41 - 3.43. It is noticeable that the calculations show a reasonably good fit to the experimental measurements. This indicates that the partition coefficients determined by the Thermocalc™ database are of the correct order of magnitude. The accuracy of the tip model for this type of an application is supported by work of Nakao et al. (1993) and Nakao & Nishimoto (1993) which also show good compatibility between modelling and segregation measurements.

From the welding experiments it can be seen that the highest welding speed of 5000 mm/min used in the experiments increases the solidification rate to about 10 mm/s, c.f. Fig. 3.6. In case of the 6% Mo alloyed stainless steels this means (see Fig. 3.43) that the PRE-ratio increases from about 0.82 (R = 1.0 mm/s) close to 0.90 (R = 10 mm/s). A further increase in the PRE-ratio would require solidification rates well in excess of 10 mm/s which means considerably higher welding speeds than those used in the present study. This, in turn, causes a constant decrease in the weld width and penetration when the arc or beam power

is not changed. Consequently, a further decrease of weld segregation and increase of pitting corrosion resistance are connected to high-speed surface remelting rather than fusion welding.

Figures 3.41 - 3.43 indicate also that the use of velocity dependent partition coefficients is not important when the solidification rate remains below 10 mm/s. With respect to the present study the velocity dependence is, thus, not needed to consider with welding speeds below about 5000 mm/min.

The effect of solidification mode on solute redistribution in dendrite tip direction could be further studied with the CDGMS-model described in Appendix 3. Results clearly indicate that primary ferritic solidification yields a considerably more homogeneous segregation profile than is the case in the primary austenitic mode, see Fig. 3.45. This arises from a lower segregation tendency and higher diffusion rates of alloying elements prevailing in primary ferritic mode (Fredriksson 1976, Brooks 1990, Campbell 1991). Consequently, solidification rates of about 10 mm/s are needed in primary austenitic mode to reach equal homogeneity as in primary ferritic mode with solidification rates of 0.1 to 1 mm/s, c.f. Fig. 3.45e.

It should, however, be noted that the CDGMS-model does not consider the role of solid state transformation of ferrite to austenite with consequent partitioning that extensively changes the segregation profile of primary ferritic welds after solidification, see Fig. 1.10. The role of solid state transformations can be, however, evaluated based on the experimental investigations. A comparison of the segregation behaviour of the 316 steels having the same Mo-content (see Fig. 3.18) indicate that primary ferritic mode (steel 316/1) exhibits slightly lower segregation also at room temperature than is the case with primary austenitic mode (steel 316/3). This is due to a slight decrease in segregation and partitioning of Cr and Mo with increasing Cr_{eq}/Ni_{eq} ratio. This observation is supported by the results of Suutala & Moisio (1980), see Fig. 1.10.

The CDGMS-model was applied also in prediction of the solidification mode according to results shown in Fig. 3.44. For steel 316/2 the calculations indicated a change in the solidification mode from primary ferritic to primary austenitic with increasing solidification rate. This tendency was observed also in the microstructural studies (Fig. 3.9). This change has been shown to be associated with increased susceptibility to solidification cracking (Lippold 1985, 1994). With the model it can be demonstrated that the change to primary austenitic solidification with associated cracking problem can be avoided by adjusting the weld composition to a sufficiently high Cr_{eq}/Ni_{eq} ratio. The results obtained by the CDGMS-calculations (Fig. 3.44) indicate that steel 316/1, having Cr_{eq}/Ni_{eq} ratio of 1.74[6], maintains primary ferritic mode well above the solidification rates normally associated with fusion welding (Fig. 3.6). On the other hand, steel 316/2 (Cr_{eq}/Ni_{eq} = 1.59[7]) was shown to change the solidification mode earlier than 316/1. These

[6] Cr_{eq}/Ni_{eq} = 1.74 (Schaeffler); Cr_{eq}/Ni_{eq} = 1.76 (Hammar & Svensson)
[7] Cr_{eq}/Ni_{eq} = 1.59 (Schaeffler); Cr_{eq}/Ni_{eq} = 1.62 (Hammar & Svensson)

findings suggest that Schaeffler's Cr_{eq}/Ni_{eq} ratio should not be much lower than 1.74 to maintain primary ferritic solidification in high-speed welding. This conclusion agrees well with the results of Lippold (1994) showing that Schaeffler's Cr_{eq}/Ni_{eq} ratios below 1.68 result in a change to austenitic solidification and, hence, an increased risk to solidification cracking.

4.1.3 Interdendritic modelling

Interdendritic or intercellular segregation plays a major role in solidification of welds and castings. In the final stage of solidication the interdendritic segregation becomes particularly strong as seen from the results of Figs 3.46 - 3.48. The NSC-model (Figs 3.49 - 3.51) shows a similar trend and emphasise that the solidification mode and partitioning of alloying elements between ferrite and austenite result in further compositional variations in the interdendritic direction.

The interdendritic models included in the PC-program (Appendix 4) could be used in case of primary austenitic solidification. For these welds the models showed reasonable compatibility with the EPMA measurements, see Figs 3.46 and 3.47. The calculations agree well with measurements as long as the fraction of solidified metal f_s exceeds 0.6 - 0.8. For these cases it is noticed that the PRE(local/av) ratio of the solidified structure remains below unity and the pitting corrosion resistance of the region that corresponds to dendrite core is predicted to remain below the base metal level. Simulations carried out with the NSC-model lead to a similar conclusion, c.f. Fig. 3.51. Both models agreeably predict that the PRE(local/av) ratio of the 316/3 and 6Mo/1 steels remains below unity to f_s values as high as 0.6 and 0.8, respectively.

In the final stages of solidification, i.e., with $f_s > 0.6 - 0.8$, a sharp increase in segregation was noticed. This is easily understood from the form of Scheil equation (17) that predicts an infinite composition for the termination of solidification when the equilibrium partition coefficient k is below unity. This arises from the fact that the solid state diffusion is not accounted for in Scheil's approximation. In the more sophisticated models used in the present study (Appendix 4) solid state diffusion is included in the calculations but the final compositions are still considerably higher than measured by EPMA, c.f. Figs 3.46 and 3.47. The discrepancy is partly explained by the fact that the models do not take into account the formation of δ-ferrite or other second phases. Consequently, the calculated analysis of the last melt to solidify remains higher than in reality. Another reason arises from the inaccuracy of the EPMA line scan analysis at narrow interdendritic regions which is due to the relatively large analysing volume (diameter 2 μm, analysing depth 1 μm) typical of the method. This is supported by the more accurate EDS-analyses taken by the FEG-STEM microscope (spot diameter 5 nm) that show clearly higher interdendritic compositions, see Fig. 3.47. The improvement in the accuracy arises from the considerably better resolution and from the use of thin-foil samples where the analysing area remains considerably smaller than in EPMA. This implication agrees well with comparable investigations of Koseki et al. (1994).

The reliability of the interdendritic calculations was further evaluated as a function of solidification rate with results shown in Fig. 3.48. There was a clear indication that the combined TIP-ID modelling can be regarded as a reasonable approach for calculation of solute redistribution. This statement is based on the sensitivity of the TIP-ID models to solidification rate (Fig. 3.48). With a solidification rate of 1 mm/s the results of the TIP-ID models also show good compatibility with the EPMA measurements (Figs 3.46 and 3.47). On the contrary, the ID models using equilibrium partitioning as input data did not show any noticeable dependence on the solidification rate (Fig. 3.48). From the previous differences it can be judged that the role of solutal undercooling on segregation behaviour is of great importance when studying the enhanced solidification rates typical of high-speed welding. In conventional arc welding applying a low solidificaton rate, i.e., of the order of 1 mm/s, the calculations based on equilibrium partitioning are also applicable with only a marginal error, c.f. Fig. 3.48a. The difference between the TIP-ID and the equilibrium models becomes, however, significant as soon as the solidification rate is enhanced to 10 mm/s and in excess (Fig. 3.48 b-d).

TIP-ID modelling indicates that the inhomogeneity of a weld is affected not only by the decrease of the interdendritic segregation but also by a constant decrease of dendrite or cell arm spacing. According to the calculations (Fig. 3.48) the spacing decreases from 17.6 to as small as 0.8 μm with increasing the solidification rate from 1 to 100 mm/s. Consequently, the dendrite or cell core area that is susceptible to pitting corrosion will rapidly decrease with increasing solidification rate. These results are supported by the experimental findings of Garner (1983), demonstrating that the critical pitting corrosion temperature of high-alloyed austenitic weld metals increases with decreasing the area of pit susceptible dendrite cores in the weld metal microstructure.

The use of the interdendritic NSC-model (Appendix 5) made it possible to study also the roles of solidification mode and ferrite-austenite transformation on solute redistribution. For steels and welds showing primary austenitic solidification the results exhibit a similar trend with the interdendritic calculations discussed above. For steels 316/3, 6Mo/1 and 6Mo/2, the NSC-model predicts (Fig. 3.51) that the PRE(local/av) ratio of the dendrite cores is below 0.8 which is somewhat lower than the corresponding values measured for the low-speed welds (100 mm/min) by the EPMA line scan analyses (see Fig. 3.18) and calculated by the dendrite tip model (solidification rate of 1 mm/s in Fig. 3.43). This difference, although relatively small, obviously arises from the assumption of equilibrium in the solid/liquid interface that is included in the NSC-model. This leads to somewhat more pronounced segregation profile than is the case with the TIP-ID model which takes the undercooling effects into account. The difference is supported also by the ID simulations of Fig. 3.48a showing a corresponding difference between the ID and TIP-ID curves.

For primary ferritic solidification the NSC-model shows a steep concentration gradient at the δ/γ interface, c.f. Figs 3.49 and 3.51, which is well understood by partitioning of the alloying elements between ferrite and austenite in solid state. This result obtained by modelling agrees reasonably well with the FEG-STEM and

EPMA line scan analyses as well as those measured by Lyman et al. (1978) and Brooks & Thompson (1991). The agreement of the calculations can be, further, assessed by comparing the calculated and measured partition ratios as summarised by Table 4.1. The comparison shows a reasonable good agreement. The calculated partition ratios of Cr and Ni are close to the values determined from the FEG-STEM measurements and those obtained from Fig. 1.10. For Mo the calculated partition ratio remains somewhat lower than that obtained from the experiments.

Table 4.1. Partition ratios ($P = C_\delta/C_\gamma$) calculated by the NSC-model for 316/1 steel and comparison of the results to FEG-STEM and EPMA measurements and to values shown in Fig. 1.10.

Partition ratio P	NSC-model (Fig. 3.49b)	FEG-STEM (Fig. 3.20)	EPMA (App.7)	Fig. 1.10
Cr	1.5	1.40	1.2-1.3	1.3-1.4
Ni	0.5	0.45	0.6-0.7	0.4-0.6
Mo	1.7	2.5	1.9-2.0	1.9-2.1

The NSC-model made it possible to demonstrate also the distribution of nitrogen during weld solidification and cooling. In both primary austenitic and primary ferritic solidification, nitrogen is predicted to concentrate towards the interdendritic region (Figs 3.49 - 3.50). In primary ferritic mode this can be explained by the low solubility of nitrogen in ferrite due to which nitrogen enriches in austenite. In primary austenitic mode nitrogen enrichment of the interdendritic region is explained by segregation of nitrogen in the same phase with Cr and Mo to interdendritic region and a slight segregation of Ni to dendrite cores (Fig. 3.50). These factors together increase the solubility of nitrogen in interdendritic austenite (Small & Pehlke 1968). This finding is supported by the EPMA (SEM-Q) measurements, c.f. Fig. 3.19. Also the investigations of Ogawa & Koseki (1988) are in agreement with the previous results. The measurements of Marshall & Gooch (1993) using laser microprobe mass spectroscopy (LAMMS) show, however, an opposite distribution for nitrogen. The discrepancy may arise from microstructural differences in comparison to the present study. The presence of second phase ferrite at the interdendritic regions would be one explanation to different partitioning of nitrogen, which is well understood from the simulation results of Fig. 3.50b.

From the previous results it can be concluded that the segregation of nitrogen may be less effective with respect to pitting corrosion resistance than is usually assumed. The C(local/av) ratio of about 0.5 calculated for dendrite cores of 6Mo/1 weld (see Fig. 3.50b) would propose that only about 50% of the total nitrogen can be regarded as effective at the core areas. This evaluation shows that due to segregation and partitioning the effect of nitrogen may remain lower than usually calculated from constant weld metal nitrogen contents. A similar conclusion is also drawn from Fig. 3.19. Concerning pitting corrosion resistance the difference between cases which consider constant nitrogen and segregated nitrogen remains, however, reasonably low as discussed in the next chapter.

4.2 Predictability of pitting corrosion resistance

The effect of solute redistribution on pitting corrosion resistance can be evaluated by reconstructing CPT-prediction diagrams based on the present results. In this approach the work of Suutala & Kurkela (1984) shown in Fig. 1.11 has been used. Prediction of the CPT-temperature for the present welds is based on calculating the minimum concentration of Cr, Mo and in some cases also N that are obtained from the modelling results for the steels studied. These compositional minimum values are then used to calculate the CPT-temperatures of welds by using the correlation shown for the base metals in Fig. 1.11. Consequently, the effect of Cr- and Mo-depletion on local PRE-index of segregated welds can be calculated and compared then to experimental CPT-values measured for corresponding welds.

Figure 4.4 summarises the predicted CPT-temperatures based on the macro-micro and the NSC-models and compares the results to experiments. The macro-micro model applied to welds showing primary austenitic solidification, predicts CPT-temperatures that are in good agreement with the measurements. This arises from the reasonably good accuracy of the WELD3D model for calculation of the solidification parameters (Figs 4.1 - 4.3). Another reason is that these calculations applying the TIP-ID approach take the effect of solidification rate into account as discussed earlier.

The NSC-model applied for primary austenitic welds predicts somewhat lower CPT-temperatures than do the previous macro-micro model and the experiments. This is due to the model being based on equilibrium calculations in the solid-liquid interface. The model is, thus, slightly conservative concerning primary austenitic solidification. For primary ferritic solidification the NSC-model predicts higher CPT-temperatures than for the primary austenitic welds. This finding agrees reasonably well with the results of the line scan analyses (Figs 3.16 and 3.18) which indicate the same ranking. However, a discrepancy is found when comparing these results to the measured CPT-temperatures, i.e., primary ferritic welds of steels 316/1 and 316/2 show lower CPT-temperatures than do primary austenitic weld 316/3 (Fig. 3.28). The pitting potential measurements support this observation (Fig. 3.27). This disagreement arises most obviously from the dominating role of the δ/γ interfaces in pitting corrosion. The δ/γ interfaces are known to be the most sensitive sites to pitting attack in austenitic welds containing δ-ferrite (Cieslak et al. 1982, Grekula et al. 1984, Fenn & Newton 1986). Modelling of the δ/γ interface phenomena needs, thus, further development with respect to its role on pitting corrosion resistance.

The macro-micro and the NSC-models could be applied also in demonstrating the roles of welding speed (100 to 400 mm/min), variation of solidification parameters (weld centerline to fusion line) and segregation of nitrogen during solidification, see Fig. 4.4. These factors were noticed to be of some importance on CPT-behaviour of welds. This applies mainly high alloyed austenitic stainless steels which are more sensitive to variation of these parameters. For AISI 301 and 304 type steels these factors are of lesser importance.

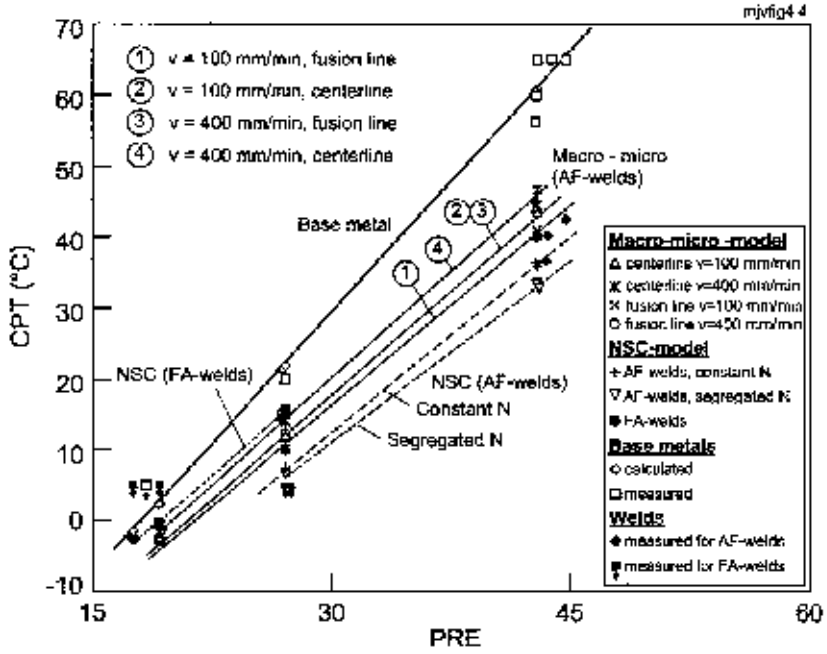

Fig. 4.4. Predicted CPT-temperatures as a function of PRE based on the macro-micro simulations (welding speed 100 - 400 mm/min) and the NSC-model (solidification rate 1.0 mm/s) and comparison of the calculations to measured data of GTA-welds and base metals (Fig. 3.28).

The effect of increasing solidification rate beyond the scope of conventional GTA-welding was studied with the dendrite tip model. From these results the CPT-prediction diagram of Fig. 4.5 can be constructed. It is readily seen that the predicted CPT-temperature of the weld metal significantly depends on the solidification rate. With the lowest solidification rate of 0.1 mm/s used in the calculations the magnitude of microsegregation becomes highest and the CPT-temperatures are the lowest, i.e., about 10 - 25°C below the base metal level depending on steel composition. In conventional GTA-welding the solidification rates are typically on the order of 1 mm/s (Fig. 3.6). In this case the predicted difference between weld and base metal is about 10 - 20°C, depending again on the alloying level. High-speed laser welding further increases the solidification rate up to 10 mm/s or more with a consequent improvement in the predicted CPT-temperature. In this case the difference between the base metal and the weld remains below 5 - 15°C for different steels studied. Higher solidification rates of 50 and 100 mm/s used in the calculations are typical of high-speed surface remelting techniques which can be argued to yield CPT-temperatures even closer to the base metal level.

The predictability and accuracy of the present CPT-prediction model was, further, critically examined by gathering reference data from literature that included steel composition and CPT-measurement results for base metals and autogenous welds. Segregation behaviour of welds in these reference steels was then calculated by the dendrite tip model and CPT-prediction was derived from the calculated segregation in a similar manner as above. Figure 4.6 shows that there exists a good correlation between the calculated and measured values. Figure 4.7, further, plots the calculated and measured CPT-temperatures on the same diagram showing a reasonably high correlation coefficient. These results corroborate that the dendrite tip model can be regarded as a reliable method for estimating pitting corrosion behaviour of stainless steel welds showing primary austenitic solidification. Based on the good agreement it can be confirmed that the pitting corrosion resistance of the dendrite cores dominates the pitting corrosion resistance of these welds.

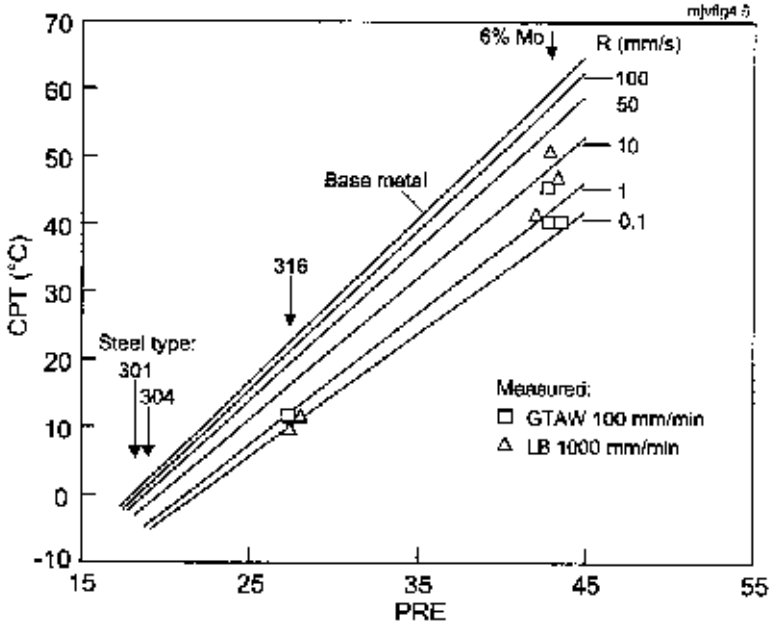

Fig. 4.5. Calculated CPT-temperatures of the welds based on dendrite tip modelling as a function of weld solidification rate (R). The calculated lines are compared to measured data of welds showing primary austenitic solidification (Fig. 3.28).

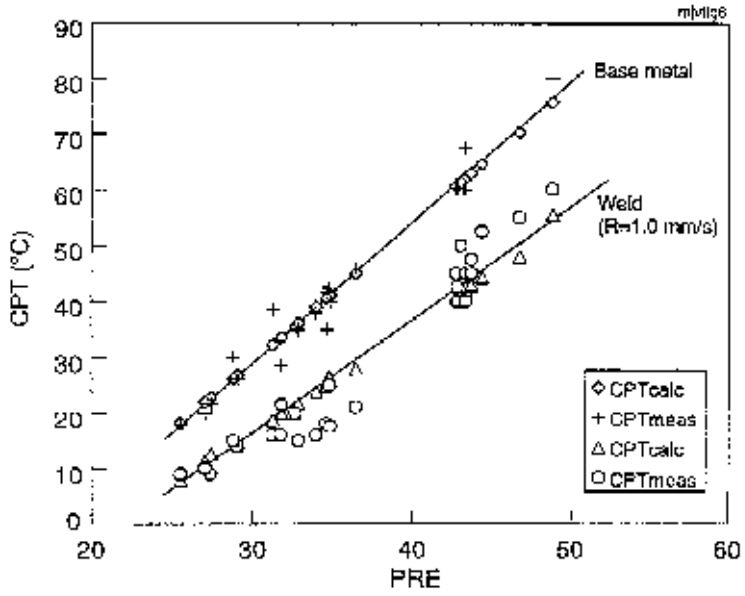

Fig. 4.6. Comparison of calculated and measured CPT-temperatures as a function of PRE based on calculations of the present study and reference data gathered from literature (Garner 1977, Suutala & Kurkela 1984, Leinonen et al. 1991, Koseki et al. 1995, Gagnepain et al. 1996, Vilpas & Hänninen 1998).

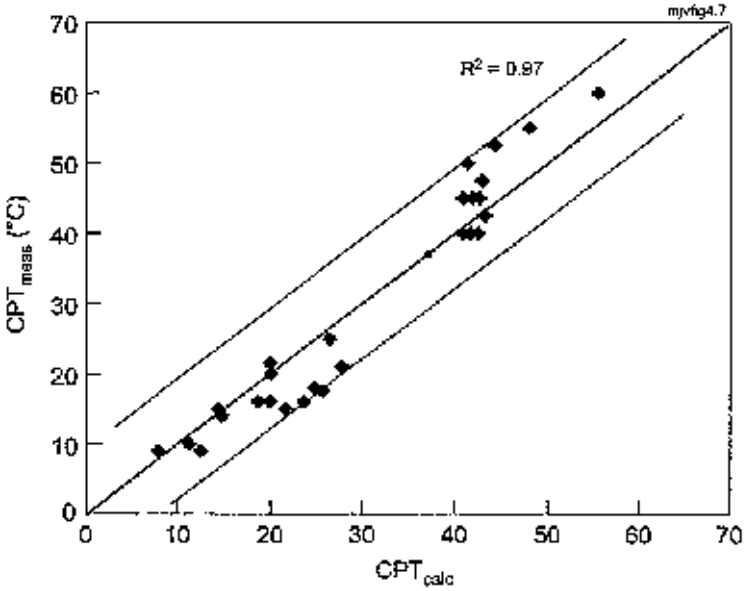

Fig. 4.7. Comparison of calculated and measured CPT-temperatures for autogenous welds based on literature data (see Fig. 4.6) and the present study.

4.3 Evaluation of experimental procedures

4.3.1 Solidification parameters

As background for the current investigation, weld cooling rate during solidification was assessed by several methods. The reasonably good compatibility between the measured values and those obtained by the WELD3D model (Fig. 4.1) indicate that the cooling rates are of the right order of magnitude. There was a good agreement also with the thermocouple measurements and analytical calculations (Figs 3.1 and 3.4). This suggests that cooling rates can be determined with a reasonable accuracy also by using the heat conduction equations shown in Appendix 6.

Uncertainty about the thermal efficiency of a welding process is, however, a factor that may cause inaccuracy in the cooling rate calculations. In the present study thermal efficiency of 0.75 was used according to Smartt (1990). The calorimeter measurements of DuPont & Marder (1995) show somewhat lower thermal efficiency ranging from 0.62 to 0.72 for GTAW. Niles & Jackson (1975) have reported values ranging from as low as 0.35 up to 0.75. Compatibility between the cooling rate measurements and the calculations indicate that the assumed thermal efficiency of 0.75 is a good estimation for the present study. It can, further, be concluded from Fig. 3.1 that a moderate variation in the value of thermal efficiency, e.g. between 0.6 - 0.8, results in only a marginal variation in the cooling rate calculations.

Accuracy of the cooling cycle measurements is also supported by their agreement with the calculations in showing a transition from 3-dimensional to 2-dimensional cooling with increasing the welding energy. From the calculated curves shown in Figs 3.1 and 3.2, it can also be observed that the transition from 3-dimensional to 2-dimensional cooling depends not only on welding energy but also on the temperature range considered. At higher temperatures such as during solidification, the cooling remains 3-dimensional for higher welding energy values (Fig. 3.1) than is the case with, e.g., the temperature range of 1200 to 800°C (Fig. 3.2). The difference can be explained by differences in heat dissipation through the plate thickness. At lower temperature more time for heat dissipation through the plate is available which causes an earlier shift to 2-dimensional cooling than is the case with higher temperatures.

Reliable results were obtained for GTA-welds but thermocouple immersion measurements were not possible for the laser welding experiments. For these welds, cooling rate determination was based on an empirical relationship between primary and secondary dendrite arm spacing and cooling rate (Katayama & Matsunawa 1984). The accuracy of this cooling rate estimation was disturbed by local variation in arm spacings which is seen from the scatter in the measurements (Fig. 3.3). This is explained by relatively large variation of solidification parameters as demonstrated in the present study by the WELD3D model (Figs 3.35 - 3.37) and documented also by Elmer (1988). Consequently, only estimates for the weld cooling rates can be derived from the spacing measurements. Better

accuracy could, probably be achieved if the spacing - cooling rate relationship was determined separately for each steel type. In spite of the scatter average spacing values from Fig. 3.3 result in cooling rates reasonably close to those calculated and measured, c.f. Fig. 3.4.

Determination of the solidification rate was found to be even more important than the cooling rate estimation because solidification rate directly affects solute redistribution, see Appendix 2 and Figs 3.41 - 3.43. For this reason the measurement accuracy of θ, needed in calculation of the solidification rate is of great importance. The other angle, ϕ shown in Fig. 1.3, is not easily measurable and causes a further uncertainty in this respect. By omitting angle ϕ, as was done in the present study, the solidification is assumed to take place normal to the solidification front. When considering microsegregation, the previous assumption will, however, not produce an error because the direction of minimum solidification rate is of interest which means that the segregation tendency is in maximum.

Figure 3.5 shows that θ could be determined within an accuracy of $\pm 5°$ which, in the case of low welding speeds, keeps the scatter of solidification rate below ± 1 mm/s, c.f. Fig. 3.6. For the high-speed welds the scatter becomes notably higher reaching the value of about ± 5 mm/s when the highest welding speed of 5000 mm/min is considered. This obviously causes inaccuracy in the calculation of solute redistribution. In the present study the average solidification rates were still in good agreement with values presented or calculated from data available in the literature, c.f. Fig. 3.6. In future studies the effect of local variations in the solidification rate needs further consideration. The role of ϕ in determination of the local solidification rate may also need to be addressed.

Average cooling and solidification rates were also used in calculating average temperature gradient in the weld metal. Although the values show scatter, there is a reasonable agreement with data available in literature, c.f. Figs 3.7 and 1.4 as well as Table 1.1. Temperature gradient does not play a major role in the dendrite tip calculations which is seen from Appendix 2 (equations A2.1 and A2.8). Error arising from scatter in temperature gradient, therefore, is not of primary importance. Temperature gradient does have an important role in constitutional supercooling and in determining the solidification morphology which could not be described by the present models.

4.3.2 Ferrite content

Figure 4.8 compares the measured ferrite contents (Fig. 3.12) to the conventional Schaeffler diagram and those developed for high cooling rate welds (Nakao et al. 1988). For conventional GTA-welding the compatibility of the measured and the predicted ferrite contents is good and remains within the accuracy of the Schaeffler-diagram that is regarded to be $\pm$ 4% up to 18% ferrite content (Lefebvre 1993). A fair agreement exists also with the Ferritscope measurements and the DeLong and WRC-predictions that were performed for the low-speed welds (Table 3.1). The exceptionally high ferrite content measured for the 301 weld,

however, deviates from the prediction (see Table 3.1). The deviation is most probably produced by the instability of austenite typical of low Ni-alloyed weld metal and from the formation of martensite which is detected by the Ferritscope.

Concerning high cooling rate welds the measured ferrite content decreases in a fair accordance with the prediction diagrams of Figs 4.8b and c. It should nevertheless be noticed that the prediction diagrams can be used only in approximate analysis of the weld behaviour. One reason for inaccuracy arises from differences in the weld cooling rates between the diagrams that were available and those measured for the present welds, c.f. Fig. 4.8. Within the accuracy of ± 4% stated above a reasonably good compatibility can still be found. Concerning the 6% Mo welds the compatibility between the measured and predicted ferrite contents is, however, somewhat more limited. In these welds the precipitation of σ-phase is expected to cause an additional inaccuracy with respect to the Schaeffler diagram. The FEG-STEM studies demonstrated that the precipitation of σ-phase cannot be completely eliminated even with the highest welding speed used (Figs 3.24 and 3.25). Once formed, σ-phase remains in the microstucture which may partly explain the difference to Schaeffler prediction diagram that considers δ-ferrite content at room temperature. The results, thus, indicate that further development is needed to improve the prediction accuracy of high alloy austenitic stainless steel welds that may show precipitation of intermetallic phases.

In addition to welding speed the weld metal ferrite content shown in Fig. 4.8 may be affected also by nitrogen content of the weld metal. In the present case the nitrogen content measurements of Table 3.2, however, indicate that the role of nitrogen remains reasonably small. Concerning steel 316/2 this can be justified by negligible differences in the weld metal nitrogen contents deposited with different welding speeds, c.f. Table 3.2a. These results indicate that the change of the solidification mode faced with 316/2 weld cannot originate from variation in the weld nitrogen content. The observed change must therefore be due to increase of the solidification rate which favours the growth of primary austenite dendrites or cells (Suutala 1981, 1983, Bobadilla 1996). Nitrogen analyses indicate that nitrogen loss, which is possible in low-speed welds and large weld pools, remains negligible when considering low or moderate nitrogen contents typical of AISI 304 and 316 steels. In the 6Mo/2 steel having a higher nitrogen content, a clear indication of nitrogen loss was, however, detected in low-speed GTA-welding. This agrees well with the findings of Allum (1992) and Hertzman & Wessman (1998).

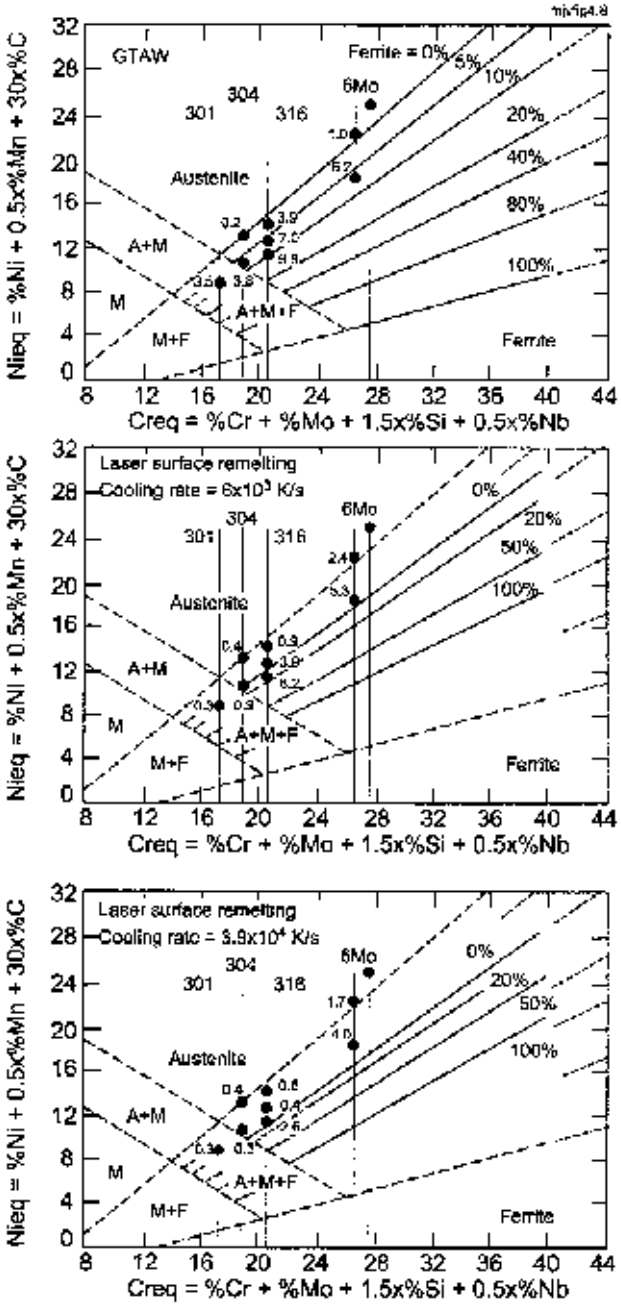

Fig. 4.8. Comparison of measured ferrite contents to the prediction diagrams proposed for different cooling rates by Nakao et al. (1988). The calculated cooling rates for the welds of the present study are: 80 K/s (a), 5400 K/s (b) and 14000 K/s (c). The corresponding welding speeds used were 100, 2000 and 5000 mm/min, respectively.

4.3.3 Microanalyses

The accuracy of the microanalyses is an important factor that affects the interpretation of the results of modelling. Electron probe microanalyses (EPMA) were used as the principal method to evaluate the magnitude of microsegregation. Concerning primary austenitic welds the resolution capability of EPMA can be evaluated by comparing the spot diameter (1 μm), typical analysing depth (1 μm) and step between individual measurements (2 μm) to the dendrite arm spacing of the test welds. Based on this comparison EPMA can be regarded sufficiently accurate within the dendrite core regions that are relatively wide with respect to the interdendritic regions (Fig. 3.50). Sufficient accuracy is further supported by modelling of the primary austenitic welds showing good compatibility between the calculated and measured core analyses (Figs 3.43 and 3.46).

At the narrow interdendritic regions and δ/γ interfaces the usefulness of EPMA is, however, limited. This became evident when comparing the results of the interdendritic simulations to the measured data. The EDS analyses carried out with the FEG-STEM microscope yielded substantially better accuracy arising from its better resolution and spot diameter of as small as 5 nm, c.f. Figs 3.20 - 3.25. In welds of 6% Mo steels the accuracy of the FEG-STEM analyses was demonstrated by identification of σ-phase at the interdendritic regions which could not be unambiguously defined by the EPMA line scan analyses. This difference in accuracy agrees well with the simulation results presented by Koseki et al. (1994) which correlated better with STEM analyses carried out by Brooks & Thompson (1991) than those performed using EPMA.

The accuracy of the EPMA line scan analyses becomes limited also with increasing welding speed. This arises from the drastic decrease in the dendrite arm spacing to 3 - 5 μm typical of high-speed welding. Consequently, the segregation behaviour may not be reliably assessed and the calculated PRE-pattern may look somewhat more uniform than it is in reality. In the welds showing primary austenitic solidification, the dendrite core region with the lowest Cr- and Mo-contents is, however, reasonably wide with respect to the more narrow interdendritic regions. The argumentation is supported by the interdendritic simulations showing that the dendrite cores cover the main part of the microstructure, c.f. Figs 3.46 - 3.48. It is, therefore, probable that the EPMA-measurements determined from the core regions yield sufficiently accurate data concerning also high speed welds. This is supported by good correlation between EPMA-measurements and dendrite tip modelling, c.f. Figs 3.41 - 3.43. At the extremely narrow interdendritic regions of the laser welds, the accuracy of EPMA line scan analyses is insufficient.

EPMA (SEM-Q) measurements, carried out to detect the distribution of nitrogen, could be understood in agreement with the interdendritic simulations. This supports the fact that the segregation behaviour of nitrogen is correctly established, c.f. Figs 3.19 and 3.50. Due to the lightness of nitrogen, accuracy of the nitrogen analyses is, however, limited. Nitrogen contents are measured from analysing areas with typical diameter of 2 μm and depth of 1 μm which may also

decrease the accuracy and increase scatter at least at the narrow interdendritic regions, c.f. Fig. 3.19. The results of the nitrogen analyses should, thus, be treated only as a semiquantitative trend that shows the segregation direction.

4.3.4 Corrosion tests

Critical pitting temperature (CPT) and pitting potential measurements of austenitic stainless steel welds often result in scatter as can be observed from the results of Figs 1.11 and 3.28. Scatter arises from several factors such as variations in pit initiation phenomena, local changes in segregation, amount of δ-ferrite and precipitation of intermetallic phases.

In the present investigation the calculation of pitting corrosion resistance is based on segregation models which is expected to have good correlation with pit propagation. The initiation of pits is, however, governed by factors that are outside the scope of the models. For this reason the actual corrosion behaviour of welds may deviate from the prediction.

For primary austenitic solidification the good agreement found between modelling and experiments indicates that the pitting corrosion resistance is dominated by segregation behaviour of the dendrite cores. Results may still show scatter for the above stated reasons. Scatter in the present study between predicted and measured CPT-temperatures is about ±5 - 10°C, c.f. Fig. 3.28. This variation remains within the experimental results of Suutala & Kurkela (1984) for autogenous GTA-welds (Fig. 1.11) and those of Woollin (1995) for high-speed laser surface melts.

One source of scatter arises most probably from differences in δ-ferrite content of the welds. The δ/γ interfaces are known to play an important role in initiation of pitting corrosion. This is corroborated by the corrosion tests where pit initiation close to the δ/γ interfaces (Fig. 3.29) and growth into austenite was observed (Fig. 3.30). Also, the relatively sharp concentration gradients observed by FEG-STEM (Figs 3.20 and 3.21) and predicted by modelling (Fig. 3.49) support the critical role of δ/γ interfaces. The role of δ-ferrite is evidenced also by the corrosion tests of 316 steel welds which show increasing pitting potential with decreasing δ-ferrite content in order: 316/1 - 316/2 - 316/3, c.f. Fig. 3.27.

The role of σ-phase detected in the 6% Mo steel welds may also be partly responsible for scatter in the CPT-measurements. The FEG-STEM studies of welds 6Mo/1 indicated that the σ/γ interface shown in Fig. 3.23 exhibits a sharp concentration gradient associated with a narrow Cr- and Mo-depleted zone which might be susceptible to pit initiation. The precipitation of σ-phase is, however, located at the interdendritic regions (see Fig. 3.11) where the Cr- and Mo-contents of the surrounding matrix are higher than at the dendrite cores. Therefore, it is probable that in the present case pitting corrosion is easier at the dendrite cores. This is supported by good compatibility between calculated and measured CPT-temperatures, c.f. Figs 4.6 - 4.7. In more severe oxidising environments than used in the present study, σ-phase has been demonstrated to show preferential attack

(Karlsson et al. 1995). For this reason and also due to brittleness, the elimination of σ-phase is important in practical welding work.

4.4 Needs and ways for improving existing models

In the present study the macroscopic WELD3D model was capable of predicting the weld pool shape and solidification parameters with a reasonable accuracy with respect to both the experimental and reference data. The model, however, includes simplifications that were necessary to validate the cases studied. Heat and mass transport rate of a weld pool is one source of uncertainty. In the present simulations this was taken into account by using an enhancement factor (see Appendix 1, Table A1.3) that adjusts the values of thermal conductivity and viscosity of the overheated weld. Although the choice of this factor makes the simulations reasonably accurate for the cases studied, there remains uncertainty about this factor for other simulations. To improve general predictability, further development work concerning heat and mass transport of a weld pool is of importance. On the other hand, it has been demonstrated (Leinonen 1987) that the penetration and width of a single GTA-weld can vary in limits of about ±10 - 15%. This arises mainly from dynamics of the arc column and weld pool flow. This suggests that accurate prediction of weld shape by macroscopic modelling becomes extremely demanding, especially, from an industrial applicability point of view.

The use of proper physical data is another important aspect of modelling. In the present study the accuracy was improved by using temperature dependent values for thermal conductivity, specific heat and viscosity that extended somewhat above the melting temperatures (Appendix 1). There is, however, lack of data concerning even higher temperatures that would be needed in accurate modelling of the weld pool. Physical property data for such high-temperature systems are scarce. The plasma environment especially requires further research in the field of arc physics.

In the present study, the calculation of solidification parameters from the results of macroscopic simulations leads to a further uncertainty. This arises from the assumption that grain growth always takes place in the direction normal to the solidification front. Due to competitive growth this is not the case in real welds. This simplification allows only mean values of solidification rates to be determined, which probably affects the calculation of segregation on the microscopic scale. Development of a more sophisticated model that accounts for competitive growth would, therefore, be of importance. One possibility would be the use of Cellular Automata method (Dress et al. 1994) linked to a macroscopic weld pool flow model such as WELD3D.

Another demand for further development of the macroscopic simulations arises from the need to expand the predictions to higher welding speeds. The role of pool turbulence is one of the most important development needs in new modifications of macroscopic models. Further research would be needed also to develop macroscopic models suitable for keyhole welding. Also the role of all surface

active elements should be included in macroscopic calculations. By this means the combined effect of both sulphur and oxygen can be considered.

The microscopic models applied in the present study require future development in a number of aspects. In the dendrite tip modelling the choice of partition coefficient k is one uncertainty that has a strong effect on the results (see Appendix 2). The k-values in the present investigation were obtained from the Thermocalc™ database. This approach yielded reasonably good correlation with experiments. In a future development, the Thermocalc™ or a corresponding thermodynamic database could be directly linked to the dendrite tip model. This would make the use of the model easier and more reliable.

Of the interdendritic models applied the combined TIP-ID model showed good correlation with experiments. On the contrary, the use of ID modelling applying equilibrium partitioning in the solute redistribution was found less accurate and insensitive to the effect of increasing solidification rate. This suggests that the effect of solute undercooling and resulting pile-up effect should not be ignored from solute redistribution calculations. The TIP-ID model, where the previous is accounted for, can be recommended for further development, especially in the case of high-speed welding applications.

Including solidification morphology into the microscopic models is one of the most important future tasks. The present models do not distinguish between dendritic and cellular solidification which causes inaccuracy when interdendritic or intercellular solidification is considered. This can be taken into account by development of 2-dimensional models that would be capable of calculating the solute redistribution linked to both primary and secondary dendrites.

The main need for microscopic modelling concerns welds showing primary ferritic solidification for which the present tools were found inadequate. This focuses on the need to calculate the post-solidification partitioning of alloying elements between δ-ferrite and austenite. The NSC-model was capable of these calculations. The model could be used for low-speed GTA-welding showing reasonably good compatibility with the experimental data. Since the NSC-model is based on equilibrium partitioning, the effect of increasing welding speed and solidification rate could, however, not be studied. The main need in this respect is to develop the model so as to be suitable also for high-speed welding.

The link between the present segregation models and corrosion behaviour of welds requires further development work. Modelling of the δ/γ interfaces with respect to pitting corrosion resistance would be of particular importance. This is the case especially for welds showing primary ferritic solidification where the role of these factors is essential from a pit initiation and growth point of view (Cieslak 1982). These factors should be taken into account also in primary austenitic welds, as proposed by the present models and experiments. In this case, however, the Cr- and Mo-depleted dendrite cores may have a more dominating role in determination of corrosion resistance.

4.5 Implication of results to industrial practice

4.5.1 Utilisation of modelling

The combined use of different models showing reasonably good agreement with experimental investigations implies that weld pool modelling can be developed into an engineering tool for developing welding procedures and with the goal of achieving desired metallurgical and corrosion properties. It can, therefore, be expected that the use of modelling will be increasingly applied in the future in order to master problems associated with welding phenomena not only in research work but also in industrial practice. A substantial amount of development work is, however, needed to develop the present models into practical engineering tools.

The WELD3D macroscopic model applied in the present investigation proved to be a useful tool in studying the effects of variable weld chemistry on weld penetration and shape. Use of the model in welding engineering may, however, be too demanding. This arises from the long computing times required for the calculations and the required theoretical understanding on weld pool behaviour. The present model can, however, be applied on the laboratory scale to study factors that correlate to weld pool behaviour, shape and resulting penetration. This data can, further, be verified and linked to more simple models that are easier to apply in welding engineering. The WELD3D model is applicable, for example, in developing neural network models that can be directly linked to practical welding application. The development of welding procedure specifications (WPS) to ensure penetration and weldability of modern steel grades is a typical example of this application. This need is the result of the new requirements contained in upcoming standards that set more stringent requirements for impurity contents.

Microscopic models can be similarly applied in materials and welding engineering. In this respect the dendrite tip especially but also the TIP-ID models were demonstrated to be useful tools in studying the effect of welding speed and solidification rate on segregation and pitting corrosion resistance of different stainless steel welds. These modelling tools are relatively simple to apply using a PC-computer. The limitations of these models, e.g., suitability only for primary austenitic solidification, should, however, be kept in mind.

In addition to weld corrosion resistance, the modelling of other metallurgical phenomena such as solidification cracking is of great practical importance. Although manageable in conventional arc welding, solidification cracking may still cause difficulties in high-speed laser processing. This is especially the case with steels that change their solidification mode from primary ferritic to primary austenitic with increasing welding speed. Steel 316/2 studied in the present investigation is a typical example of this behaviour (Fig. 3.9). Modelling of weld solidification may help in avoiding this problem. The CDGMS-model applied in the present study is a useful tool for this purpose as noticed from the results of Fig. 3.44. This kind of analysis may help welding engineers to adjust the composition of steel and weld in order to avoid cracking problems in high-speed laser welding. In other words, weld composition can be adjusted by modelling toward higher Cr_{eq}/Ni_{eq}-ratios than in case of low-speed welding.

4.5.2 Development of welding processes

The results of the present study clearly demonstrated that high-speed welding is useful in decreasing weld inhomogeneity and, hence, in reaching higher pitting corrosion resistance of austenitic stainless steel welds. Due to improved productivity the use of high-speed welding processes is also usually economically justified. Exploitation of high-speed welding is, however, limited by a constant decrease in weld penetration with increasing welding speed. To compensate for decreased penetration, the heat input must be increased which inevitably leads to slower weld cooling rate, higher dendrite arm spacing and more pronounced segregation all of which are harmful to pitting corrosion resistance. Further development of welding procedures in order to maintain maximum welding speed with full penetration are, therefore, of importance.

Reference tests carried out with nitrogen alloyed shielding gas indicate that nitrogen addition can be regarded as an alternative to high-speed welding. Results showed (Fig. 3.28) that the improvement in pitting corrosion resistance is of the same order of magnitude between these two alternatives. From the results it can be assessed that a combined welding process employing both high-speed welding and nitrogen alloyed shielding gas would be worth of further development. The main advantage of the combination would originate from more effective nitrogen uptake in the weld metal, which, due to smaller weld pool, results in a lower nitrogen loss in the molten state. This is expected to enable the use of somewhat higher heat input to eliminate weld penetration typical of high-speed welding. The risk of increased porosity may need further consideration in procedure development. Technically the use of nitrogen in the shielding gas is relatively simple both in GTA- and laser welding. The use of laser welding would, furthermore, eliminate the electrode wear problem faced with GTAW.

The use of high-speed welding should also be promoted in consumable welding. Further development of high-speed welding for filler wire processes would eliminate the use of highly overalloyed Ni-based consumables that are expensive and require skilled welding technique. High-speed welding would enable the use of less overalloyed and, thus, lower priced wires which are also less sensitive to weld parameter variations. Higher welding speed is expected to be advantageous also in decreasing the width of the unmixed zone at the weld fusion line with consequent decrease of corrosion problems typical of welded joints deposited with overalloyed consumables (Hibner et al. 1991, Lundin et al. 1998). Filler wire feeding can be applied not only in arc welding but also in laser welding where the development of high-speed welding procedures is expected to yield even more potential advantages.

4.5.3 Remarks on post-weld treatments

As a further option, high-speed welding may find increasing applications used in combination with post-weld annealing. The advantage of this process combination is due to a constant decrease in dendrite arm spacing and microsegregation with increasing welding speed (Fig. 3.3). Consequently, post-weld annealing used for

homogenisation of the weld microsegregation becomes more effective due to smaller diffusion distances. Arising from this, the annealing time of high-speed laser welds can be substantially decreased to achieve homogenisation and restoration of weld pitting corrosion resistance (Kujanpää & David 1987). This procedure would be directly applicable in automatic welding, especially when annealing time can be reduced to the level that allows its direct connection to production line operations.

As an alternative to high-speed welding, pitting corrosion resistance can be improved also by surface remelting techniques. The results of Fig. 4.5 clearly indicate that surface melting with a high solidification rate in excess of 10 mm/s is effective in this respect. The present results obtained by modelling are in a good agreement with those demonstrated recently by Woollin (1995), Nakao et al. (1993) and Nakao & Nishimoto (1993) who demonstrated a notable improvement in the CPT-temperature of 6% Mo type superaustenitic welds. Studies by Akgun et al. (1995), Kamachi Mudali et al. (1998) and Sakairi & Tsuru (1991) have further demonstrated that laser surface remelting can have a beneficial effect on corrosion resistance not only through homogenisation of microsegregation but also via modification of sulphur based inclusions in the remelted region. Arising from this, the initiation of pitting corrosion becomes difficult. This is supported by a recent study of Kuronen & Kyröläinen (1999) where the use of high-speed laser welding has been demonstrated to result in even better pitting corrosion resistance than predicted by the segregation models of the present study.

Principally high-speed surface remelting can be applied with a laser process capable of high deposition speeds. As an alternative to laser processing the use of GTA-surface remelting should also be considered. Figures 3.17 and 3.18 indicate that remelting speeds of about 1000 mm/min would lead to a considerable removal of microsegregation and, hence, result in improved weld pitting corrosion resistance. GTA-surface remelting of weld surface and root regions is readily applicable in most workshops and should, therefore, obtain special attention in the future. Constant increase of laser facilities in industry makes it possible to achieve even further advantages with the surface remelting technique. Irrespective of the process, the optimisation of remelting parameters to achieve optimal overlapping of side-by-side beads as well as the control of distortions requires further consideration in the application of surface remelting.

5. Concluding remarks

In the present investigation various modelling techniques have been applied and linked together to study the role of weld solidification phenomena and related microsegregation in the welding of austenitic stainless steels. The main objective was to demonstrate the effect of solidification rate, temperature gradient and cooling rate on solute redistribution and resulting pitting corrosion resistance of the welds studied.

The most important findings of the investigation and potential areas for further study are summarised in the following sections.

5.1 Main results

5.1.1 Modelling

The results obtained with the various models applied in the present study can be summarised as follows:

- Macroscopic WELD3D modelling used in the calculation of weld penetration shape showed reasonably good correlation with experimental test welds when applying low-speed GTA-welding. Also the solidification parameters calculated from the WELD3D simulations were in good agreement with the values determined experimentally as well as with data published by other authors.

- Output from the WELD3D model was linked to microscopic dendrite tip and interdendritic models. It was possible to demonstrate the effect of welding speed and weld shape variations on microsegregation of welds showing primary austenitic solidification. The calculated microsegregation was further linked to the prediction of weld pitting corrosion resistance measured in terms of critical pitting temperature (CPT). The calculations showed good compatibility with the experimentally measured segregation patterns and CPT-temperatures.

- On the microscopic scale, the dendrite tip model that was applied as a function of weld solidification rate yielded good agreement with the results obtained from the EPMA line scan analyses. The results indicated that the weld metal inhomogeneity can be substantially decreased with increasing the solidification rate up to 100 mm/s, i.e. the maximum value used in simulations. Correspondingly, the CPT-temperature of the weld or plate surface can be improved to nearly the same value as the base metal via rapid surface remelting.

- Dendrite tip calculations using the CDGMS-model were applied in prediction of the primary phase of solidification. Calculations indicated that primary austenitic solidification becomes favourable with increasing solidification rate. For steel 316/2 used in the present investigation the change from primary

ferritic to primary austenitic solidification observed experimentally could be predicted by the model. Results showed that the model is directly applicable in preliminary selection of weld composition in order to eliminate solidification cracking of high-speed laser welds that cannot be predicted by conventional microstructural diagrams.

- By linking the dendrite tip calculations to interdendritic modelling (TIP-ID modelling) the effect of solidification rate on solute redistribution in the direction normal to dendrite growth could be predicted. At the dendrite core regions, the calculated results showed good agreement with the EPMA line scan analyses. At the interdendritic regions the calculations predicted higher enrichment of alloying elements than was measured. This was arising most probably due to the formation of δ-ferrite not taken into account in the model. These TIP-ID calculations clearly demonstrated the beneficial effect of increasing solidification rate on compositional enrichment at the dendrite cores which results in better pitting corrosion resistance. The TIP-ID model was shown to be a more accurate tool in prediction of solute redistribution than the interdendritic (ID) model which is based on equilibrium calculations.

- Solute redistribution calculations carried out by the NSC-model showed that the solidification mode has a profound effect on microsegregation and partitioning of alloying elements. For welds showing primary austenitic solidification, the dendrite cores are the weakest link with respect to weld pitting corrosion resistance. In primary ferritic solidification the lowest resistance was predicted to be located at the second phase austenite in the vicinity of the δ/γ interfaces. The interfaces exhibited a sharp concentration gradient which indicates that these regions might also be prone to pitting attack.

- The NSC-model could be used in predicting the distribution of nitrogen in the solidified weld metal. During solidification to austenite nitrogen was predicted to segregate to the interdendritic direction which was confirmed by the EPMA line scan analyses. In solidification to ferrite nitrogen enriches to austenite as expected from differences in the solubility of nitrogen between austenite and ferrite.

5.1.2 Experimental investigations

The experimental part of the present study can be summarised as follows:

- Weld cooling rate measured by thermocouples and calculated based both on primary and secondary dendrite arm spacings and thermal conductivity equations were all in good agreement. The solidification rate calculated from the welding speed and direction of solidification agreed with the values reported in other studies. The temperature gradient calculated from the cooling rate and the solidification rate also showed good agreement with published data.

- Optical microscopy of the welds revealed that the solidification mode was in accordance with predictions developed for high-speed welds of austenitic stainless steels. For the nine steels studied, those having $Cr_{eq}/Ni_{eq} \geq 1.74$ showed primary ferritic solidification in low-speed welding but favoured fully ferritic solidification in high-speed laser welds. Steel 316/2 ($Cr_{eq}/Ni_{eq} = 1.62$) solidified in primary ferritic mode during low-speed welding but changed the solidification mode to primary austenitic with welding speeds in excess of 1500 mm/min. The steels with $Cr_{eq}/Ni_{eq} \leq 1.46$ showed primary austenitic solidification with decreasing amount of second phase ferrite with increasing welding speed.

- Scanning (SEM) and transmission (FEG-STEM) electron microscopy studies of the 6% Mo alloyed welds revealed the presence of σ-phase at the interdendritic regions. The amount of σ-phase decreased with increasing welding speed. Small islands of σ-phase were, however, documented even in welds deposited with a speed of 5000 mm/min.

- Line scan analyses carried out using an electron probe microanalyser (EPMA) indicated a constant decrease in weld segregation with increasing welding speed. This was confirmed by the CMA and FEG-STEM analyses. It was concluded that the accuracy of the EPMA line scan analyses is sufficient at the dendrite core regions. This finding was of major importance for reliable comparison between experiments and microscopic modelling of welds showing primary austenitic solidification.

- The distribution of nitrogen analysed from the 6Mo/3 steel welds was analysed by EPMA (SEM-Q). Measurements showed that nitrogen segregates interdendritically during solidification to austenite. This results in nitrogen depletion at the dendrite core regions leading to slightly lower pitting corrosion resistance of welds than predicted when assuming nitrogen to be uniformly distributed. The effect of segregation of nitrogen on pitting corrosion resistance remains, however, reasonably small.

- Corrosion tests carried out on test welds showed that increasing welding speed has a slightly positive effect on weld pitting corrosion resistance. The effect of increasing welding speed from 0.1 to 5 m/min is of the same order of magnitude as the use of 5 - 10% nitrogen addition in the shielding gas. In welds showing primary ferritic solidification, the pits were noticed to nucleate at the δ/γ interfaces and to propagate to austenite leaving δ-ferrite uncorroded. In primary austenitic solidification, the austenitic dendrite cores were the most susceptible sites for pit initiation and growth.

5.2 Suggestions to further studies

The present study created a number of ideas for further investigations. The most important of these are associated with the development of new modelling tools or to achieving more favourable metallurgical properties and corrosion resistance of welds.

For development of macroscopic modelling the following items are regarded to be of importance:

- Development of macroscopic models that are capable of calculating weld pool turbulence effects. This important extension to the present models would make macroscopic modelling suitable for the prediction of weld penetration shape and solidification parameters concerning high-speed welding.

- Model development for keyhole welding such as high-speed laser processing. With the rapid increase of laser welding applications the modelling of keyhole welding is of increasing importance and could also support other keyhole processes such as plasma and electron beam welding.

- Creation and application of models that have better capability to follow weld solidification phenomena. A typical example is modelling of competitive growth during weld solidification that can be handled by cellular automata techniques.

In microscopic modelling the main development needs generated by the present study are:

- Development of modelling of primary ferritic solidification covering not only solidification but also solid state transformations as a function of weld cooling rates. This would make it possible to calculate partitioning of alloying elements between δ and γ as a function of welding parameters and give a basis for more accurate segregation models.

- Extension of corrosion models that pay attention not only to microsegregation but also to pit initiation from non-metallic inclusions, δ/γ interfaces and Cr-carbides and the role of these factors in pitting corrosion resistance.

- Development of microscopic models that account for solidification morphology.

In addition to the development of individual models, a more flexible linking of macroscopic models to microscopic ones requires further development work. By this means it would become possible directly to show the effect of macroscopic parameters on microscopic phenomena such as pitting corrosion resistance and solidification cracking.

In the field of experimental investigations, the present study calls for the following research items:

- Studies on pit initiation, especially for high-speed welds should be introduced. Present segregation models omit pit initiation which may lead to only a partial understanding of the pitting corrosion resistance of welds. Consequently pitting corrosion resistance of high-speed laser welds and surface remelted regions

may be even more effectively improved in practice than is predicted by the segregation models.

- Development of welding procedures for increased pitting corrosion resistance deserves attention. This development work would include combinating the processes used in the present study. The use of high-speed welding with nitrogen alloyed shielding gases or with overalloyed consumables are typical examples.

- The role of post-weld annealing for homogenisation of high-speed laser welds and its effect on pitting corrosion resistance would be of importance in certain applications. Post-weld annealing would offer advantages especially for high-speed welds that exhibit smaller dendrite arm spacing and more rapid and effective homogenisation than do conventional arc welds. This research item would include recommendations on annealing procedures based on modelling and measurements of attained homogenisation as well as possibilities to apply this technology in practise.

- Instead of post-weld annealing, laser surface remelting of the weld surfaces can also be considered. Surface remelting should be thoroughly considered in the production of large and heavy components for which post-weld heat treatment becomes difficult or impossible. Optimisation of process parameters to minimise residual stresses and distortions is one of the main topics in this field.

6. Summary

The present study focuses on the effects of weld solidification and resulting microsegregation on pitting corrosion resistance of austenitic stainless steel welds applying computer aided modelling. Special emphasis is given to the effects of welding speed on solute redistribution and their influence on weld pitting corrosion resistance. The computer models are verified and compared to experimental investigations using autogenous GTA- and laser welding over the welding speed range of 0.1 to 5 m/min for several austenitic stainless steel grades.

Several different analytical and computer aided models were applied and linked together in modelling of the welds. The macroscopic WELD3D model was used to predict weld pool shape and calculate solidification parameters, i.e., cooling rate, solidification rate and temperature gradient. Output from this model was further used as input parameters for microscopic dendrite tip and interdendritic solidification models. An attempt was made to apply the microscopic models to predict microsegregation and the resulting pitting corrosion resistance of the welds. The important role of solidification rate and, hence, welding speed was clearly seen and has been thoroughly discussed.

The macroscopic model was found to predict weld shape and solidification parameters that agreed well with the experimental data. Also the segregation profiles and predicted CPT-temperatures obtained by the macro-micro modelling showed a good correlation with experimental measurements. The macro-micro simulations indicated that the weld metal composition and welding speed are of major importance in determination of segregation and pitting corrosion resistance while the effect of weld shape variations remains negligible.

The microscopic dendrite tip model was applied to welds showing primary austenitic solidification and had a good agreement with the measured segregation profiles analysed by EPMA line scan analyses. By linking the dendrite tip calculations to the interdendritic modelling, the effect of solidification rate on solute redistribution in the direction normal to dendrite growth could be predicted and showed reasonable agreement with the EPMA line scan analyses. Simulations showed that weld inhomogeneity could be substantially decreased with increasing welding speed. This has a direct beneficial effect on the weld pitting corrosion resistance.

The dendrite tip and interdendritic calculations showed that the solidification mode of the welds has a profound effect on microsegregation and partitioning of alloying elements. For welds showing primary austenitic solidification the dendrite cores became the weakest link with respect to weld pitting corrosion resistance. On the other hand, welds showing primary ferritic solidification exhibited the lowest pitting corrosion resistance at the second phase austenite in the vicinity of δ/γ interfaces. Corrosion tests carried out on test welds supported the findings of the modelling.

Interdendritic calculations suggested that, in the case of primary austenitic solidification, nitrogen segregates in the interdendritic direction which was confirmed by the EPMA-analyses. In primary ferritic solidification nitrogen was predicted to enrich in second phase austenite as expected from solubility differences between austenite and ferrite.

Solidification parameters determined from the welding experiments showed good agreement with reference data gathered from other studies. Weld cooling rates measured by thermocouples as well as those calculated from dendrite arm spacings and thermal conductivity equations were all in good agreement. The average solidification rates and temperature gradients determined based on measurements from the solidification structure and cooling rate data correlated well with earlier studies. Solidification parameters were also in agreement with values calculated by the WELD3D model.

Line scan analyses carried out with EPMA showed a constant decrease in weld segregation with increasing the welding speed. This finding was supported by CMA-analyses. Accuracy of EPMA at the dendrite core regions was sufficient to demonstrating the important relationship between welding speed and microsegregation seen in the microscopic models. At the narrow interdendritic regions the accuracy of EPMA becomes, however, insufficient. This was demonstrated by EDS-analyses linked with a FEG-STEM microscope which yielded a considerably better resolution capacity.

References

Akgun, O., Urgen, M. & Cakir, A. F. 1995. The effect of heat treatment on corrosion behaviour of laser surface melted 304L stainless steel. Material Science & Engineering, Vol. A203, pp. 324 - 331.

Allum, C. J. 1992. Nitrogen absorption from welding arcs. In: Nitrogen in Arc Welding - a Review. WRC Bulletin 369. New York: Welding Research Council. Pp. 68 - 84.

Arata, Y., Matsuda, F. & Katayama, S. 1976. Solidification crack susceptibility in weld metals of fully austenitic stainless steels (Report I) - Fundamental investigation on solidification behavior of fully austenitic and duplex microstructures and effect of ferrite on microsegregation. Transactions of JWRI, Vol. 5, No. 2, pp. 35 - 51.

Aziz, M. J. 1982. Model for solute redistribution during rapid solidification. Journal of Applied Physics, Vol. 53, pp. 1158 - 1168.

Bobadilla, M., Lacaze, J. & Lesoult, G. 1996. Effect of cooling rate on the solidification behaviour of austenitic stainless steels. Scandinavian Journal of Metallurgy, Vol. 25, pp. 2 - 10.

Brandis, H. & Kiesheyer, H. 1984. Influence of molybdenum additions on the chloride corrosion resistance of stainless steels. International Conference on Stainless Steels ’84, Gothenburg, Sweden, 3 - 4 September 1984. London: Institute of Metals. ISBN 0-904357-68-6

Brody, H. D. & Flemings, M. C. 1966. Solute redistribution in dendritic solidification. Transactions of the Metallurgical Society of AIME, Vol. 236, pp. 615 - 624.

Brooks, J. A. 1990. Weld microsegregation: modelling and segregation effects on weld performance. Weldability of Materials. Detroit: ASM-International. Pp. 41 - 47.

Brooks, J. A. 1995. Weld solidification and microstructural development. In: Smartt, B., Johnson, A. & David, S. (eds.) Trends in Welding Research. Gatlinburg, Tennessee, USA, 5 - 8 June 1995. Ohio: ASM-International. Pp. 123 - 134. ISBN 0-87170-567-2

Brooks, J. A. & Baskes, M. I. 1986. Weld microsegregation characterization and modeling. In: David, S. A. (ed.) Advances in Welding Science and Technology. Trends in Welding Research, Gatlinburg, Tennessee, USA, 18-22 May 1986. Ohio: ASM-International. Pp. 93 - 99. ISBN 0-87170-245-2

Brooks, J. A. & Thompson, A. W. 1991. Microstructural development and solidification cracking susceptibility of austenitic stainless steel welds. International Materials Reviews, Vol. 36, pp. 16 - 44.

Burgardt, P. & Campbell, R. D. 1992. Chemistry effects on stainless steel weld penetration. Key Engineering Materials, Vols. 69 & 70, pp. 379 - 416.

Campbell, J. 1991. Castings. Oxford: Butterworth-Heinemann Ltd. 288 p.

Choo, R. T. C., Szekely, J. & Westhoff, R. C. 1992. On the calculation of the free surface temperature of gas-tungsten-arc weld pools from first principles, Part I. Modelling the welding arc. Metallurgical Transactions, Vol. 23B, pp. 357 - 369.

Cieslak, W. R., Duquette, D. J. & Savage, W. F. 1981. Pitting corrosion of stainless steel weldments. In: David, S. (ed.) American Society for Metals Conference on Trends in Welding Research in the Unites States. New Orleans, USA, 16 - 18 November 1981. Ohio: AWS. Pp. 361 - 379.

Cieslak, M. J., Ritter, A. M. & Savage, W. F. 1982. Solidification cracking and analytical electron microscopy of austenitic stainless steel weld metals. Welding Journal, Vol. 61, pp. 1 - 8.

Clyne, T. W. & Kurz, W. 1981. Solute redistribution during solidification with rapid solid state diffusion. Metallurgical Transactions, Vol. 12A, pp. 965 - 971.

David, S. A., Vitek, J. M. & Heibble, T. L. 1987. Effect of rapid solidification on stainless steel weld metal microstructures and its implications on the Schaeffler diagram. Welding Journal, Vol. 66, pp. 289 - 300.

David, S. A. & Vitek, J. M. 1989. Correlation between solidification parameters and weld microstructures. International Materials Reviews, Vol. 34, pp. 213 - 245.

David, S. A. & Vitek, J. M. 1991. Analysis of weld metal solidification and microstructures. In: Cerjak, H. & Easterling, K. E. (eds.) Mathematical Modelling of Weld Phenomena 1. The Institute of Materials. Pp. 42 - 59.

David, S. A., DebRoy, T. & Vitek, J. M. 1994. Phenomenological modeling of fusion welding processes. MRS Bulletin, Vol. 19, pp. 29 - 35.

David, S. A., Vitek, J. M., Boatner, L. A. & Rappaz, M. 1995. Application of single crystals to achieve quantitative understanding of weld microstructures. Materials Science and Technology, Vol. 11, pp. 939 - 947.

DebRoy, T. & David, S. A. 1995. Physical processes in fusion welding. Reviews of Modern Physics, Vol. 67, pp. 85 - 112.

DeLong, W. T. 1974. Ferrite in austenitic stainless steel weld metal. Welding Journal, Vol. 53, pp. 273 - 286.

Dowling, N. J. E. 1995. The effect of complex inclusions on pit initiation in 18% chromium - 8% nickel stainless steels. Corrosion, Vol. 51, pp. 343 - 355.

Dress, W. B., Zacharia, T. & Radhakrishnan, B. 1994. Cellular automata modelling of weld solidification structure. International Conference on Modelling and Control of Joining Processes. Orlando, Florida, USA, 8 - 10 December 1993. Ohio: AWS. Pp 321 - 328. ISBN 087171440X

DuPont, J. N. & Marder, A. R. 1995. Thermal efficiency of arc welding processes. Welding Journal, Vol. 74, pp. 406 - 416.

DuPont, J. N. 1996. Solidification of an Alloy 625 weld overlay. Metallurgical and Materials Transactions, Vol. 27A, pp. 3612 - 3620.

Eklund, G. S. 1974. Initiation of pitting at sulphide inclusions in stainless steel. Journal of Electrochemical Society, Vol. 121, pp. 467 - 473.

Elmer, J. W. 1988. The influence of cooling rate on the microstructure of stainless steel alloys. Ph.D. Thesis, Massachusetts Institute of Technology, USA. 387 p.

Elmer, J. W., Allen, S. M. & Eagar, T. W. 1989. The influence of cooling rate on the ferrite content of stainless steel alloys. In: Trends in Welding Research, Gatlingburg, Tennessee, USA, 14 - 18 May 1989. Ohio: ASM International. Pp. 123 - 134. ISBN 0-87170-372-6

Fenn, R., Brown, R., Barnes, N. R., Woolley, R. G. & Newton, C. J. 1985. Corrosion of welded austenitic stainless steels. Journal of Materials for Energy Systems, Vol. 7, pp. 55 - 63.

Fenn, R. & Newton, C. J. 1986. Corrosion of two similar austenitic stainless steels when welded. Material Science and Technology, Vol. 2 , pp. 181 - 188.

Flemings, M. C. 1974. Solidification Processing. McGraw-Hill. 364 p.

Fredriksson, H. 1972. The solidification sequence in an 18-8 stainless steel, investigated by directional solidification. Metallurgical Transactions, Vol. 3, pp. 2989 - 2997.

Fredriksson, H. 1976. Segregation phenomena in iron-base alloys. Scandinavian Journal of Metallurgy, Vol. 5, pp. 27 - 32.

Gagnepain, J.-C., Verneau, M., Bennefois, B., Courdreuse, L. & Charles, J. 1996. UR B66: A new high nitrogen super austenitic stainless steel with improved structure stability and corrosion resistance properties. In: Stainless Steels ’96, Düsseldorf, Germany, 3 - 5 June 1996. Düsseldorf: German Iron and Steel Institute. Pp. 63 - 69. ISBN 3-514-00601-6

Garner, A. 1977. Chloride pitting resistance of ferrite-containing austenitic stainless steel weld metal. Pulp and Paper Industry Corrosion Problems, Vol. 2, pp. 87 - 93.

Garner, A. 1982. Corrosion of high alloy austenitic stainless steel weldments in oxidizing environments. Materials Performance, Vol. 8, pp. 9 - 14.

Garner, A. 1983. Pitting corrosion of high alloy stainless steel weldments in oxidizing environments. Welding Journal, Vol. 62, pp. 27 - 34.

Ginn, B, J. 1992. Effects of welding variables on the pitting resistance of autogenous welds in UNS S31254 high alloy austenitic stainless steel tube. TWI Technology Briefing 462. 4 p.

Giovanola, B. & Kurz, W. 1990. Modeling of microsegregation under rapid solidification conditions. Metallurgical Transactions, Vol. 21A, pp. 260 - 263.

Gooch, T. G. 1996. Corrosion behavior of welded stainless steel. Welding Journal, Vol. 75, pp. 135 - 154.

Grekula, A. I., Kujanpää, V. P. & Karjalainen, L. P. 1984. Effect of solidification mode and impurities on pitting corrosion in AISI 316 GTA welds. Corrosion, Vol. 40, pp. 569 - 572.

Grong, O. 1997. Metallurgical Modelling of Welding. 2nd ed. London: The Institute of Materials. 605 p. ISBN 1-86125-036-3

Hammar, Ö. & Svensson, U. 1979. Influence of steel composition on segregation and microstructure during solidification of austenitic stainless steels. In: Solidification and Casting of Metals. Sheffield, UK, 18 - 21 July 1977. London: The Metals Society. Pp. 401 - 410. ISBN 0-904357-16-3

Heiple, C. R. & Roper, J. R. 1982. Mechanism for minor element effect on GTA-fusion zone geometry. Welding Journal, Vol. 61, pp. 97 - 102.

Hertzman, S. & Wessman, S. 1998. An experimental and theoretical study of nitrogen flux in stainless steel TIG welds. 5th International Conference on High Nitrogen Steels, HNS-98. Espoo, 24 - 26 May and Stockholm, 27 - 28 May 1998. Espoo, Finland: Helsinki University of Technology. 11 p. ISBN 951-22-4093-9

Heubner, U. & Rockel, M. 1986. Entwicklung neuer korrosionbeständiger Werkstoffe für den Chemieapparatenbau. Werkstoffe und Korrosion, Vol. 37, pp. 7 - 12.

Hibner, E. L., Hinshaw E. B. & Lamb, S. 1991. Weld fabrication of a 6% molybdenum alloy to avoid corrosion in bleach plant service. In: TAPPI 1991. Engineering Conference. Nashville, Tennesee, USA, 30 September - 3 October 1991. Atlanta: Tappi Press. Pp. 511 - 527.

Hong, T., Pitscheneder, W. & DebRoy, T. 1998. Quantitative modelling of motion, temperature gyrations and growth of inclusions in weld pool. Science and Technology of Welding and Joining, Vol. 3, pp. 33 - 41.

Hunt, J.D. 1979. Keynote Address: Cellular and primary dendrite spacings. In: Solidification and Casting of Metals. Sheffield, 18 - 21 July 1977. London: The Metals Society. Pp. 3 - 9. ISBN 0 904357 16 3.

Inoue, H., Koseki, T., Ohkita, S. & Tanaka, T. 1995. Effect of solidification on subsequent ferrite-to-austenite massive transformation in an austenitic stainless steel weld metal. ISIJ International, Vol. 35, pp. 1248 - 1257.

Jones, D. A. 1992. Principles and prevention of corrosion. New York: Macmillan Publishing Company. 568 p. ISBN 0-02-361215-0

Kamachi Mudali, U., Pujar, M. G. & Dayal, R. K. 1998. Effects of laser surface melting on the pitting resistance of sensitized nitrogen-bearing type 316L stainless steel. Journal of Materials Engineering and Performance, Vol. 7, pp. 214 - 220.

Karlsson, L., Ryen, L. & Pak, S. 1995. Precipitation of intermetallic phases in 22% Cr duplex stainless steel weld metals. Welding Journal, Vol. 74, pp. 28 - 40.

Katayama, S. & Matsunawa, A. 1984. Solidification microstructure of laser welded stainless steels. 4th International Conference on Lasers and Electro-Optics, Boston, Massachusetts, USA, 12 - 15 November 1984. Ohio: Laser Institute of America. Pp. 60 - 67. ISBN 091 203 5269

Katayama, S., Fujimoto, T. & Matsunawa, A. 1985. Correlation among solidification process, microstructure, microsegregation and solidification cracking susceptibility in stainless steel weld metals. Transactions of JWRI, Vol. 14, pp. 123 - 138.

Kobayashi, S. 1988. Mathematical analysis of solute redistribution during solidification based on a columnar dendritic model. Transactions of ISIJ, Vol. 28, pp. 728 - 735.

Koseki, T., Matsumiya, T., Yamada, W. & Ogawa, T. 1994. Numerical modelling of solidification and subsequent transformation of Fe-Cr-Ni alloys. Metallurgical and Materials Transactions, Vol. 25A, pp. 1309 - 1321.

Koseki, T., Inoue, H., Morimoto, H. & Ohkita, S. 1995. Prediction of solidification and phase transformation of stainless steel weld metals. Nippon Steel Technical Report 65. Pp. 33 - 40.

Kotecki, D. J. & Siewert, T. A. 1992. WRC-1992 constitution diagram for stainless steel weld metals: a modification of the WRC-1988 diagram. Welding Journal, Vol. 72, pp. 171 - 178.

Kou, S. & Lee, Y. 1982. The effect of quenching on the solidification structure and transformation behavior of stainless steel welds. Metallurgical Transactions, Vol. 13A, pp. 1141 - 1152.

Kou, S. & Wang, Y. H. 1986. Weld pool convection and its effect. Welding Journal, Vol. 65, pp. 63 - 70.

Kujanpää, V. 1984. Studies on weld defects in austenitics stainless steels. Oulu, Finland: University of Oulu. 39 p. + App. (Acta Universitatis Ouluensis, Series C, Technica No. 28). ISBN 951-42-1760-8

Kujanpää, V. & David, S. A. 1987. Microsegregation in high-molybdenum austenitic stainless steel laser beam and gas tungsten arc welds. In: The Changing Frontiers of Laser Materials Processing, Arlington, Virginia, USA, 10 - 13, 1986. Pp. 63 - 69.

Kujanpää, V., Karjalainen, L. P. & Sikanen, H. 1987. Weld discontinuities in austenitic stainless steel sheets - role of steel type. Welding Journal, Vol. 66, pp. 155 - 161.

Kuronen, M. & Kyröläinen, A. 1999. Pitting corrosion resistance of TIG-, HF- and laser welds. Hitsaustekniikka, Vol. 48, pp. 23 - 26. (In Finnish).

Kurz, W., Giovala, B. & Trivedi, R. 1986. Theory of microstructural development during rapid solidification. Acta Metallurgica, Vol. 34, pp. 823 - 830.

Kurz, W. & Fisher, D. J. 1992. Fundamentals of Solidification. 3rd ed. Switzerland: Trans Tech Publications. 305 p. ISBN 0-87849-522-3

Kurz, W. 1995. Dendrite growth in welding. In: Cerjak, H. (ed.) Mathematical Modelling of Weld Phenomena 2. London: The Institute of Materials. Pp. 40 - 53. ISBN 0-901716-63-4

Kyröläinen, A. 1984. Initiation of pitting at inclusions in calcium treated stainless steel. International Conference on Stainless Steels ‘84, Gothenburg, Sweden, 3 - 4 September 1984. London: Institute of Materials. Pp. 173 - 180. ISBN 0-904357-68-6

Lefebvre, J. 1993. Guidance on specifications of ferrite in stainless steel weld metal. Welding in the World, Vol. 31, pp. 390 - 406.

Leinonen, J. 1987. Cast-to-cast variations in weld penetration in austenitic stainless steels. Oulu, Finland: University of Oulu. 94 p. (Acta Universitatis Ouluensis, Series C, Technica No. 39). ISBN 951-42-2383-7

Leinonen, J., Järvenpää, S. & Karjalainen, P. 1991. Pitting corrosion properties of autogenous TIG and laser welds. In: Stainless Steels ’91. Chiba, Japan, 10 - 13 June 1991. Tokyo: The Iron and Steel Institute of Japan. Pp. 373 - 378.

Liljas, M., Stenvall, B., Holmberg, B. & Jonsson, O. 1992. Welding of a nitrogen enhanced superaustenitic stainless steel. Proceedings of International Conference on Application of Stainless Steel ‘92. Stockholm, Sweden: Jernkontoret. Pp. 971 - 980. ISBN 91-971474-5-1

Lippold, J. C. 1985. Centerline cracking in deep penetration electron beam welds in type 304L stainless steel. Welding Journal, Vol. 64, pp. 127 - 136.

Lippold, J. C. 1994. Solidification behavior and cracking susceptibility of pulsed-laser welds in austenitic stainless steels. Welding Journal, Vol. 73, pp. 129 -139.

Lyman, C. E., Manning, P. E. Duquette, D. J. & Hall, E. 1978. STEM microanalysis of duplex stainless steel weld metal. In: Johari, Om (ed.) Scanning Electron Microscopy, Chicago, Illinois, USA. Pp. 213 - 220. ISBN 0-931288-01-0

Lundin, C. D., Liu, W., Zhou, G. & Qiao, C. Y. 1998. Unmixed zones in arc welds: significance on corrosion resistance of high molybdenum stainless steels. Welding Research Council, Bulletin 428, New York, 98 p.

Manning, P. E., Duquette, D. J. & Savage, W. F. 1980a. The role of sulphide inclusion morphology in pit initiation of several type 300 series stainless steels. Corrosion, Vol. 36, pp. 313 - 319.

Manning, P. E., Duquette, D. J. & Savage, W. F. 1980b. Technical note: The effect of retained ferrite on localised corrosion in 304L stainless steel. Welding Journal, Vol. 59, pp. 260 - 262.

Marshall, P. I. & Gooch, T. G. 1993. Effect of composition on corrosion resistance of high-alloy austenitic stainless steel weld metals. Corrosion, Vol. 49, pp. 514 - 526.

Matsuda, F., Nakagawa, H. & Lee, J.-B. 1991. Numerical analysis on microsegregation during weld solidification - weld crack susceptibility of duplex stainless steels. Report IV. Quarterly Journal of Japan Welding Society, Vol. 9, pp. 85 - 92.

Matsunawa, A., Yokoya, S. & Asako, Y. 1987. Convection in weld pool and its effect on penetration shape in stationary arc welds. Transactions of Japan Welding Research Institute, Vol. 16, pp. 1 - 8.

McNallan, M. J. & DebRoy, T. 1991. Effect of temperature and composition on surface tension in Fe-Ni-Cr alloys containing sulfur. Metallurgical Transactions B, Vol. 22B, August, pp. 557 - 560.

Miettinen, J. 1992. Mathematical simulation of interdendritic solidification of low-alloyed and stainless steels. Helsinki: Finnish Academy of Technology. 81 p. (Acta Polytechnica Scandinavica, Chemical Technology and Metallurgy Series, No. 207). ISBN 951-666-367-2

Miettinen, J. 1995a. Calculation of thermophysical properties for special stainless steels. Helsinki University of Technology, Laboratory of Metallurgy. Report TKK-V-B106. 12 p.

Miettinen, J. 1995b. Thermodynamic and diffusion data for modeling of solidification of steels. Espoo: Helsinki University of Technology, Laboratory of Metallurgy. Report TKK-V-B112. 65 p.

Miettinen, J. 1995c. Solidification related thermophysical data for low-alloyed and stainless steels. Espoo: Helsinki University of Technology, Laboratory of Metallurgy. Report TKK-V-B113. 44 p.

Miettinen, J. 1998. Private communication, November.

Mills, K. C. & Keene, B. J. 1990. Factors affecting variable weld penetration. International Materials Reviews, Vol. 35, pp. 185 - 216.

Mitrovic-Scepanovic, V. & Brigham, R. J. 1996. Effect of manganese on pitting properties of type 301L stainless steel. Corrosion, Vol. 52, pp. 23 - 27.

Mundra, K., Debroy, T. & Kelkar, K. M. 1996. Numerical prediction of fluid flow and heat transfer in welding with a moving heat source. Numerical Heat Transfer, Part A, Vol. 29, pp. 115 - 129.

Mundra, K., DebRoy, T., Babu, S. S. & David, S. A. 1997a. Weld metal microstructure calculations from fundamentals of transport phenomena in the arc welding of low alloy steels. Welding Journal, Vol. 76, pp. 163 - 171.

Mundra, K., Blackburn, J. M. & DebRoy, T. 1997b. Absorption and transport of hydrogen during gas metal arc welding of low alloy steel. Science and Technology of Welding and Joining, Vol. 2, pp. 174 - 184.

Nakao, Y., Nishimoto, K. & Zhang, W-P. 1988. Effects of rapid solidification by laser surface melting on solidification modes and microstructures of stainless steels. Transactions of JWRI, Vol. 19, pp. 20 - 26.

Nakao, Y. & Nishimoto, K. 1993. Effects of laser surface melting on corrosion resistance of stainless steel and nickel-base alloy clad layers in cast bi-metallic pipes. ISIJ International, Vol. 33, pp. 934 - 940.

Nakao, Y., Nishimoto K. & Zhang, W-P. 1993. Effects of laser surface melting on corrosion resistance in weld metals of Mo-containing austenitic stainless steels. Transactions of the Japan Welding Society, Vol. 24, pp. 57 - 62.

Nenonen, P., Tapper, U. & Vilpas, M. 1998. Microsegregation of high-alloy austenitic stainless steel weld metal studied by field emission TEM microscope. In: Punnonen, E.-L. & Heikinheimo, E. (eds.) 50th Annual Meeting of the Scandinavian Society for Electron Microscopy, SCANDEM. Espoo and Helsinki, 7 - 10 June 1998. Pp. 169 - 170. ISBN 951-22-4023-8

Niles, R. & Jackson, C. E. 1975. Weld thermal efficiency of the GTAW process. Welding Journal, Vol. 54, pp. 26 - 32.

Nishimoto, K. 1995. Private communication, April.

Ogawa, T., Aoki, S., Sakamoto, T. & Zaizen, T. 1982. The weldability of nitrogen-containing austenitic steel: Part I - chloride pitting corrosion resistance. Welding Journal, Vol. 61, pp. 139 - 148.

Ogawa, T. & Koseki, T. 1988. Weldability of newly developed austenitic alloys for cryocenig service: Part II - high nitrogen stainless steel weld metal. Welding Journal, Vol. 67, pp. 8 - 17.

Ohnaka, I. 1986. Mathematical analysis of solute redistribution during solidification with diffusion in solid state. Transactions of ISIJ, Vol. 26, pp. 1045 - 1051.

Pitscheneder, W., DebRoy, T., Mundra, K. & Ebner, R. 1996. Role of sulfur and processing variables on the temporal evolution of weld pool geometry during multikilowatt laser beam welding of steels. Welding Journal, Vol. 75, pp. 71 - 80.

Quarfort, R. & Alfonsson, E. 1989. An improved cell for electrochemical pitting corrosion testing. 11th Scandinavian Corrosion Congress, NKM 11. Ullandhaug, Stavanger, Norway, 19 - 21 June 1989. 4 p.

Rappaz, M., David, S. A., Vitek, J. M. & Boatner, L. A. 1989. Development of microstructures in Fe-15Ni-15Cr single crystal electron beam welds. Metallurgical Transactions, Vol. 20A, pp. 1125 - 1138.

Rappaz, M., David, S. A., Vitek, J. M. & Boatner, L. A. 1990. Analysis of Solidification Microstructures in Fe-Ni-Cr Single-Crystal Welds. Metallurgical Transactions, Vol. 21A, pp. 1767 - 1782.

Renner, M., Heubner, U., Rockel, M. B. & Wallis, E. 1986. Temperature as a pitting and crevice corrosion criterion in the $FeCl_3$ test. Werkstoffe und Korrosion, Vol. 37, pp. 183 - 190.

Rockel, M. B., Herda, W. & Brill, U. 1991. Two new austenitic stainless steels with high molybdenum content and nitrogen additions. In: Stainless Steels ’91. Chiba, Japan, 10 - 13 June 1991. Tokyo: The Iron and Steel Institute of Japan. Pp. 78 - 85.

Rondelli, G., Vicentini, B. & Cigada, A. 1995. Influence of nitrogen and manganese on localized corrosion behaviour of stainless steels in chlorine environments. Materials and Corrosion, Vol. 46, pp. 628 - 632.

Runnsjö, G. 1981. Carbon and nitrogen in steel. Determination of content and distribution by electron probe microanalysis (EPMA). Uppsala, Sweden: University of Uppsala. 49 p. (Acta Universitatis Upsaliensis, Abstracts of Uppsala Dissertations from the Faculty of Science). ISBN 91-554-1145-2

Sahm, P. R. & Schubert, F. 1979. Keynote address: Solidification phenomena and properties of cast and welded microstructures. In: Solidification and Casting of Metals. Sheffield, UK, 18 - 21 July 1977. London: Metals Society. Pp. 389 - 400. ISBN 0-904357-16-3

Sakairi, M. & Tsuru, T. 1991. Stochastic characteristics of pit embryos on stainless steels. In: Stainless Steels ’91. Chiba, Japan, 10 - 13 June 1991. Tokyo: The Iron and Steel Institute of Japan. Pp. 71 - 77.

Sarreal, J. A. & Abbaschian, G. J. 1986. The effect of solidification rate on microsegregation. Metallurgical Transactions, Vol. 17A, pp. 2063 - 2073.

Scheil, E. 1942. Bemerkungen zur Schichtkristallbildung. Zeitschrift für Metallkunde, Vol. 34, pp. 70 - 72.

Scheller, P. R., Brooks, R. F. & Mills, K. C. 1995. Influence of sulfur and welding conditions on penetration in thin strip stainless steels. Welding Journal, Vol. 75, pp. 69 - 75.

Sedriks, A. J. 1979. Corrosion of stainless steels. New York, USA: The Electrochemical Society. John Wiley. 282 p. ISBN 0-471-05011-3

Sedriks, A. J. 1983. Role of inclusions in pitting and crevice corrosion of stainless steels. International Material Reviews, Vol. 28, pp. 295 - 307.

Small, W. M. & Pehlke, R. D. 1968. The effect of alloying elements on the solubility of nitrogen in liquid iron - chromium - nickel alloys. Transactions of AIME, Vol. 242, pp. 2501 - 2505.

Smartt, H. B. 1990. Arc welding processes. In: Olson, D. L., Dixon, R. & Liby, A. L. (eds.) Welding: Theory and Practice. Elsevier Science Publishers. Pp. 175 - 208.

Suutala, N. 1980. Koostumuksen ja jähmettymisolosuhteiden vaikutus austeniittisen ruostumattoman teräksen jähmettymiseen (Effects of composition and solidification conditions on solidification in austenitic stainless steels). Lic.Tech. Thesis. Oulu: University of Oulu. 94 p. + App. (In Finnish).

Suutala. N. 1981. Effect of manganese and nitrogen on solidification mode in austenitic stainless steel welds. Metallurgical Transactions, Vol. 13A, pp. 2121 - 2130.

Suutala, N. 1983. Effect of solidification conditions on the solidification mode in austenitic stainless steels. Metallurgical Transactions, Vol. 14, pp. 191 - 197.

Suutala, N. & Moisio, T. 1980. The use of chromium and nickel equivalents in considering solidification phenomena in austenitic stainless steels. International Conference on Solidification Technology in the Foundry and Casthouse, University of Warwick, Coventry, 15 - 17 September 1980. Pp. 310 - 314.

Suutala, N. & Kurkela, M. 1984. Localized corrosion resistance of high alloy austenitic stainless steels and welds. International Stainless Steels '84, Gothenburg, Sweden, 3 - 4 September 1984. London: Institute of Metals. Pp. 240 - 247. ISBN 0-904357-68-6

Suutala, N., Takalo, T. & Moisio, T. 1979. Single phase ferritic solidification mode in austenitic-ferritic stainless steel welds. Metallurgical Transactions, Vol. 10A, pp. 1183 - 1190.

Suutala, N., Takalo, T. & Moisio, T. 1980. Ferritic-austenitic solidification mode in austenitic stainless steel welds. Metallurgical Transactions, Vol. 11A, pp. 717 - 725.

Suutala, N., Takalo, T. & Moisio, T. 1981. Technical Note: Comment on the transformation $\delta \rightarrow \gamma$ by a massive mechanism in austenitic stainless steel. Welding Journal, Vol. 60, pp. 92 - 93.

Szklarska-Smialovska, Z. 1960. Review of literature on pitting corrosion published since 1960. Corrosion, Vol. 27, pp. 223 - 233.

Takalo, T., Suutala, N. & Moisio, T. 1976. Influence of ferrite content on its morphology in some austenitic weld metals. Metallurgical Transactions, Vol. 7A, pp. 1591 - 1592.

Takalo, T., Suutala, N. & Moisio, T. 1979. Austenitic solidification mode in austenitic stainless steel welds. Metallurgical Transactions, Vol. 10A, pp. 1173 - 1181.

Vilpas, M. & Hänninen, H. 1998. The role of nitrogen in improving pitting corrosion resistance of high-alloy austenitic and duplex stainless steel welds. 5th International Conference on High Nitrogen Steels, HNS-98. Espoo, 24 - 26 May and Stockholm, 27 - 28 May 1998. Espoo: Helsinki University of Technology. 6 p. ISBN 951-22-4093-9

Winkler, C., Amberg, G., Inoue, H. & Koseki, T. 1997. A numerical and experimental investigation of qualitatively different weld pool shapes. 4th

International Seminar on Numerical Analysis of Weldability, Graz-Seggau, Austria. 39 p.

Woollin, P. 1995. Laser beam surface melting of high alloy austenitic stainless steel. In: Smartt, B., Johnson, A. & David, S. (eds.) Trends in Welding Research. Galtingburg, Tennessee, USA, 5 - 8 June 1995. ASM-International. Pp. 455 - 459. ISBN 0-87170-567-2

Wranglen, G. 1974. Electrochemical properties of sulfides in steel and the role of sulfides in the initiation of corrosion. ASM International Symposium on Sulfide Inclusions in Steel. Port Chester, New York, USA, 7 - 8 November 1974. Ohio: ASM. Pp. 361 - 379.

Yang, Z. & DebRoy, T. 1998. Modeling macro- and microstructures of gas-metal-arc welded HSLA100 steel. Accepted for publication in Metallurgical and Materials Transactions B. 21 p. + App.

Zacharia, T., David, S. A., Vitek, J. M. & DebRoy, T. 1989a. Heat transfer during Nd:YAG pulsed laser welding and its effect on solidification structure of austenitic stainless steels. Metallurgical Transactions, Vol. 20A, pp. 957 - 967.

Zacharia, T., David, S. A., Vitek, J. M. & DebRoy, T. 1989b. Weld pool development during GTA and laser beam welding of type 304 stainless steel. Part I - Theoretical analysis. Welding Journal, Vol. 68, pp. 499 - 509.

Zacharia, T., David, S. A., Vitek, J. M. & DebRoy, T. 1989c. Weld pool development during GTA and laser beam welding of type 304 stainless steel. Part II - Experimental correlation. Welding Journal, Vol. 68, pp. 510 - 519.

Zacharia, T., David, S. A., Vitek, J. M. & Kraus, H. G. 1991. Computational modeling of stationary gas tungsten arc weld pools and comparison to stainless steel 304 experimental results. Metallurgical Transactions, Vol. 22B, pp. 243 - 257.

Zacharia, T., Vitek, J. M., Goldak, J. A., DebRoy, T. A., Rappaz, M. & Bhadeshia, H. 1995. Modelling of fundamental phenomena in welds. Modelling and Simulation in Materials Science and Engineering, Vol. 3, pp. 1 - 22.

Macroscopic WELD3D simulations

The WELD3D program is based on control-volume computation method of Patankar (1980). Calculations include the effect of surface tension, electromagnetic and buoyancy forces on weld pool convection. The plasma drag force and the effect of weld pool surface deformation is not considered by the calculations.

The program calculates weld pool convection and heat flow using equations that are based conservation of mass, momentum and energy. The governing equations described by Mundra et al. (1996) were represented in a finite difference form and solved iteratively on a line-by-line basis, utilising a Tri-Diagonal Matrix Algorithm (TDMA). Discreatisation of the equations was implemented by he SIMPLE-algorithm (Semi Implicit Method for Pressure-Linked Equations).

Calculations were performed for three-dimensional incompressible steady state flow describing solidification of autogenous GTA-welds. The plate thickness studied was 5 mm. Because of joint symmetry only one half of the butt-welded plate is modelled. The welding parameters used in the experiments are given in Table A.1.1. The simulation was carried out using boundary conditions presented in Table A.1.2. The material constants of Table A.1.3 were used. Surface tension was modelled by using data presented in Table A.1.4. Figures A.1.1 - A.1.3, further, show the values of thermal conductivity, specific heat and viscosity used as a function of temperature.

Table A.1.1. Process parameters.

	Verification runs with steel 304/2		Weld shape simulation runs	
	Run 1	Run 2	S = 20/150 [1]	S = 20/150 [1]
Current (A)	150	150	150	150
Voltage (V)	9.8	11.8	11.5	11.5
Weld travel speed (mm/min)	100	200	100	400
Arc radius (mm)	2.6	2.6	2.6	2.6
Shielding gas (l/min) [2]	12	12	12	12
Backing gas (l/min) [2]	6	6	6	6

1) runs with varying the S-content of the steel (20 and 150 ppm)
2) Ar 99.998%

Table A.1.2. Boundary conditions describing the heat transfer.

Arc efficiency factor	0.75
Heat transfer coefficient on the bottom surface of the sheet (cal/cm^2 s K)	0.0070
Heat transfer coefficient on the side surfaces of the sheet (cal/cm^2 s K)	0.0010

Table A.1.3. Material properties.

Liquidus temperature (°C)	1445
Density of liquid metal (g/cm^3)	6.8
Enthalpy of solid at melting point (cal/g)	219
Enthalpy of liquid at melting point (cal/g)	277
Viscosity & liquid conduction enhancement factor	6
Coefficient of thermal expansion (1/°C)	$0.5 \cdot 10^{-4}$
Solidus temperature (°C)	1387

Table A.1.4. Data used for the computation of temperature coefficient of surface tension for Fe-S system (Sahoo et al. 1988).

Temperature coefficient of surface tension for pure iron (N/mK)	$-5.0 \cdot 10^{-4}$
Enthalpy of segregation (kJ/kg mole)	$-1.66 \cdot 10^{5}$
Surface excess at saturation (kg mole/m^2)	$1.3 \cdot 10^{-8}$
Entropy factor	$3.18 \cdot 10^{-3}$

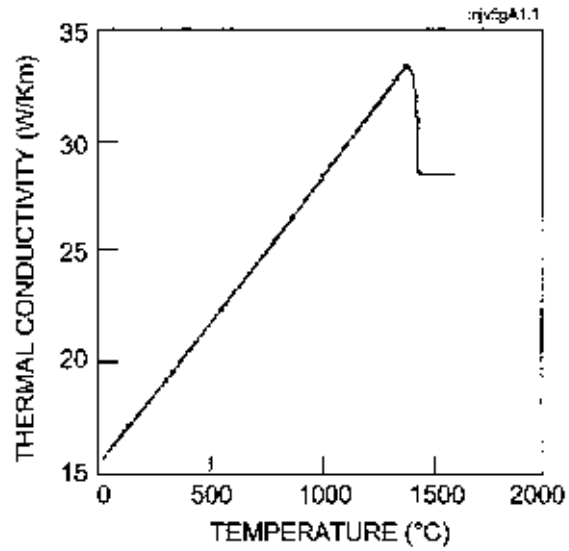

Figure A.1.1. Thermal conductivity as a function of temperature (Miettinen 1992, 1995a-c).

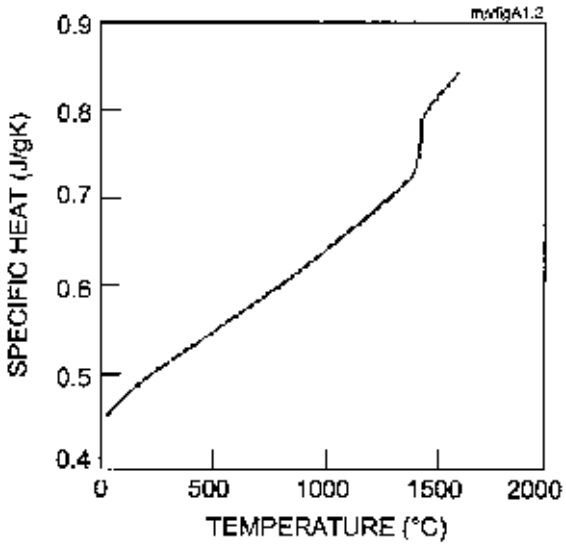

Figure A.1.2. Specific heat as a function of temperature (Miettinen 1992, 1995a-c).

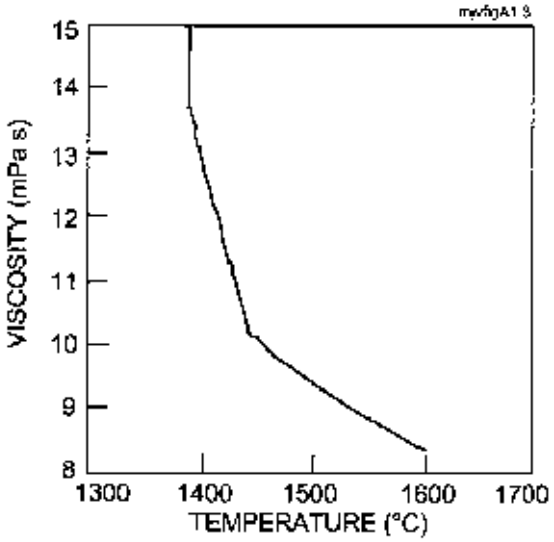

Figure A.1.3. Viscosity as a function of temperature (Zacharia et al. 1995, Miettinen 1992, 1995 a-c).

References

Miettinen, J. 1992. Mathematical simulation of interdendritic solidification of low-alloyed and stainless steels. Helsinki: Finnish Academy of Technology. 81 p. (Acta Polytechnica Scandinavica, Chemical Technology and Metallurgy Series, No. 207). ISBN 951-666-367-2

Miettinen, J. 1995a. Calculation of thermophysical properties for special stainless steels. Helsinki University of Technology, Laboratory of Metallurgy. Report TKK-V-B106. 12p.

Miettinen, J. 1995b. Thermodynamic and diffusion data for modeling of solidification of steels. Helsinki University of Technology, Laboratory of Metallurgy. Report TKK-V-B112. 65 p.

Miettinen, J. 1995c. Solidification related thermophysical data for low-alloyed and stainless steels. Helsinki University of Technology, Laboratory of Metallurgy Report TKK-V-B113. 44 p.

Mundra, K., Debroy, T. & Kelkar, K. M. 1996. Numerical prediction of fluid flow and heat transfer in welding with a moving heat source. Numerical Heat Transfer, Part A, Vol. 29, pp. 115 - 129.

Patankar, S. V. 1980. Numerical heat transfer and fluid flow. New York: McGraw-Hill. 197 p. ISBN 0-07-048740-5

Sahoo, P., DebRoy, T. & McNallan, M. J. 1988. Surface tension of binary metal - Surface active solute systems under conditions relevant to welding metallurgy. Metallurgical Transactions, Vol. 19B, pp. 483 - 491.

Zacharia, T., Vitek, J. M., Goldak, J. A., DebRoy, T. A., Rappaz, M. & Bhadeshia, H. 1995. Modeling of fundamental phenomena in welds. Modelling and Simulation in Materials Science and Engineering, Vol. 3, pp. 1 - 22.

APPENDIX 2

Dendrite tip modelling

Composition at the dendrite tip was calculated based on the KGT-model (Kurz et al. 1986) that was available as a computer programme (Nishimoto 1995). In the model the composition at the dendrite tip (C_s) and the tip radius (r_t) can be solved as a function of solidification rate (R) according to the following approach (Kurz & Fisher 1992, Nakao & Nishimoto 1993).

For constrained dendritic growth the tip radius can be solved as a function of solidification rate from the following group of equations:

$$AR^2 + BR + C = 0 \tag{A2.1}$$

$$Iv(P) = Pexp(P)\, E_1(P) \tag{A2.2}$$

$$E_1(P) \cong -0.577 - \ln(P) + 4P/(P+4) \tag{A2.3}$$

$$P = \frac{r_t R}{2D} \tag{A2.4}$$

$$C_s = \frac{kC_0}{[1-(1-k)Iv(P)]} \tag{A2.5}$$

In Equation (A2.1):

$$A = \frac{\pi^2 \Gamma}{(PD)^2} \tag{A2.6}$$

$$B = \frac{mC_0(1-k)\,\zeta_c}{\{D[1-(1-k)Iv(P)]\}} \tag{A2.7}$$

$$C = G \tag{A2.8}$$

In Equation (A2.7):

$$\zeta_c = 1 - 2k\left[\sqrt{1+(2\pi/P)^2} - 1 + 2k\right] \text{ when } P < \pi^2/\sqrt{k} \tag{A2.9}$$

$$\zeta_c = \frac{\pi^2}{(kP^2)} \text{ when } P > \pi^2/\sqrt{k} \tag{A2.10}$$

In the previous equations Iv(P) is Ivantsov's solution to paraboloid dendrite growth, exp(P) is exponential integral, P is solute Peclet number, D is diffusion

coefficient in liquid state, Γ is Gibbs-Thomson parameter, m is slope of liquidus line, k is equilibrium partition coefficient and C_0 initial liquid composition.

Values used for slope of the liquidus line (m) and the partition coefficient (k) is based on Fe-Cr-Ni ternary alloy system (Nakao & Nishimoto 1993). The Gibbs-Thomson parameter (Γ) is calculated from thermodynamic data of Chuang & Chang (1987).

The KGT-model is applicable for binary alloys. Therefore, the calculations were conducted by assuming the alloy to be binary alloy of type Fe-X, where X refers to alloying element such as Cr or Mo.

As a result of the calculation the dendrite tip composition (C_s) is obtained from Equation (A2.5) as a function of solidification rate.

For high solidification rates the velocity dependent partition coefficient k´ defined by Aziz (1982) was used:

$$k' = \frac{k + (a_0 R / D)}{1 + (a_0 R / D)} \qquad \text{(A2.11)}$$

where k refers to equilibrium partition ratio, R is solidification rate, D is the solute diffusion coefficient in the solid-liquid interface and a_0 is a length scale related to interatomic distance, which is between 0.5 and 5 nm for metals.

References

Aziz, M. J. 1982. Model for solute redistribution during rapid solidification. Journal of Applied Physics, Vol. 53, pp. 1158 - 1168.

Chuang, Y.-Y. & Chang, A. 1987. A thermodynamical analysis and calculation of the Fe-Ni-Cr phase diagram. Metallurgical Transactions, Vol. 18A, pp. 733 - 745.

Kurz, W., Giovanola, B. & Trivedi, R. 1986. Theory of microstructural development during rapid solidification. Acta Metallurgica, Vol. 34, pp. 823 - 830.

Kurz, W. & Fisher, D. J. 1992. Fundamentals of Solidification. 3rd ed. Switzerland: Trans Tech Publications. 305 p. ISBN 0-87849-522-3

Nakao, Y. & Nishimoto, K. 1993. Effects of laser surface melting on corrosion resistance of stainless steel and nickel-base alloy clad layers in cast bi-metallic pipes. ISIJ International, Vol. 33, pp. 934 - 940.

Nishimoto, K. 1995. Private communication, April.

CDGMS-model

During dendritic growth, solute pile-up will be formed ahead of the dendrite tip which causes the liquid phase to become undercooled. Under steady state conditions, the solutal supersaturation indicating the relative height of the pile-up can be described as follows (Kurz & Fisher 1992):

$$\Omega_i = (C_L - C_0) / (C_L - C_s) \quad \text{(A3.1)}$$

For a paraboloid dendrite tip Ω_i is defined as:

$$\Omega_i = P \exp(P) E_1(P) \quad \text{(A3.2)}$$

where $E_1(P)$ is the exponential integral and P solutal Peclet number:

$$P = r_t R / 2D_{iL} \quad \text{(A3.3)}$$

In these equations, C_0 is the nominal composition, C_L and C_s are the liquid and the solid compositions at the dendrite tip, P is solutal Peclet number, R is the growth rate of the D_{iL} is the diffusion coefficient of the solute i in liquid and r_t is the dendrite tip radius.

In order to calculate the undercooling in multicomponent alloys, a model designated to CDGMS (Constrained Dendrite Growth of Multicomponent Steels) was used (Miettinen 1992, 1998). In this model, Ω_i is solved together with chemical-potential-equality equations for solutes i = 2,..,n:

$$\mu_i^S(T_S, C_{S\ tip\ i}, \ldots, C_{S\ tip\ n}) = \mu_i^L(T_L, C_{L\ tip\ i}, \ldots, C_{L\ tip\ n}), \quad i = 1,\ldots, n \quad \text{(A3.4)}$$

These equations are used to calculate the temperature of the undercooled liquid T^S and the dendrite tip compositions, $C_{S\ tip\ i}$ and $C_{L\ tip\ i}$ (i = 2,..,n) either in ferritic (S = δ) or austenitic (S = γ) mode. The precise description of the chemical potential terms, $\mu_i^{S,L}$ in Eq. (A3.4) depends on the solution model to be used. In the CDGMS model, the classical substitutional solution model was chosen (Miettinen 1992).

The solution of the group of Equations (A3.1 - A3.4) implies the determination of the solutal supersaturations $\Omega_i = f(R, r_t, D_{iL})$ via Eqs (A3.2) and (A3.3). To evaluate the tip radius in a multicomponent alloy, the method of Bobadilla et al. (1996) was applied.

In the previous treatment, it was assumed that thermodynamic equilibrium is reached at the S/L interterface. At high growth rates, however, the local equilibrium may be lost due to the effects of interface friction, capillarity and

solute-drag effects, resulting from finite solute diffusion inside the interface. Following the treatment of Jönsson and Ågren (1988), these effects were included in the CDGMS model by modifying Eq. (A3.4) as follows:

$$\mu_i^S + \Delta G_f + \Delta G_\delta + \mu_i^* = \mu_i^L \qquad \text{(A3.5)}$$

where ΔG_f refers to the effect of interface friction, ΔG_δ describes the effect of capillarity, and μ_i^* is the effect of solute-drag.

References

Bobadilla, M., Lacaze, J. & Lesoult, G. 1996. Effect of cooling rate on the solidification behaviour of austenitic stainless steels. Scandinavian Journal of Metallurgy, Vol. 25, pp. 2 - 10.

Jönsson, B. & Ågren, J. 1988. Thermodynamic and kinetic aspects of crystallization of supercooled Ag-Cu liquids. Journal of the Less-Common Metals, Vol. 145, pp. 153 - 166.

Kurz, W. & Fisher, D. J. 1992. Fundamentals of Solidification. 3rd ed. Switzerland: Trans Tech Publications. 305 p. ISBN 0-87849-522-3

Miettinen, J. 1992. Mathematical simulation of interdendritic solidification of low-alloyed and stainless steels. Helsinki: Finnish Academy of Technology. 81 p. (Acta Polytechnica Scandinavica, Chemical Technology and Metallurgy Series, No. 207). ISBN 951-666-367-2

Miettinen, J. 1998. Private communication, November.

Interdendritic solidification modelling

The solute redistribution in interdendritic direction was calculated by a PC-programme (Nishimoto 1995) based on the following models:

(A) Brody & Flemings model, modified by Clyne & Kurz (1981)

The composition of solid (C_s) as a function of solidified metal (f_s) can be solved from the following equation:

$$C_s = kC_0 \, [1- f_s \, (1-2 \, \Omega k) \,]^{(k-1)/(1-2\Omega)} \qquad \text{(A4.1)}$$

where Ω refers to back diffusion parameter describing the magnitude of homogenising diffusion:

$$\Omega = \alpha\left[1-\exp\left(-\frac{1}{\alpha}\right)\right]-1/2\exp\left(-\frac{1}{2\alpha}\right) \qquad \text{(A4.2)}$$

In equation (A4.2) $\alpha = D_s \, t_f \, / \, (d/2)^2$ where D_s is diffusion coefficient in solid state, t_f local solidification time and d/2 length of volume element, i.e., half of dendrite spacing.

(B) Ohnaka model (Ohnaka, 1986)

$$C_s = kC_0\left[1-\Gamma f_s\right]^{\frac{(k-1)}{\Gamma}} \qquad \text{(A4.3)}$$

Here $\Gamma = \dfrac{1-\beta k}{(1+\beta)}$ and $\beta = 4\alpha$ for columnar growth and α as decribed above.

(C) Giovanola-Kurz model (Giovanola & Kurz, 1990)

The model applies a two phase approach as follows:

- for $f_s = 0 - f_x$: $f_s = a_1 C_s^{\,2} + a_2 C_s + a_3$ (A4.4)
- for $f_s = f_x - 1$: $f_s = 1 + (f_x - 1)(C_s / C_x)^{\frac{1}{k-1}}$ (A4.5)

Equation (A4.4) describes compositional transients of alloying elements in the beginning and during solidification where incomplete mixing of the liquid is typical. Consequently, equation (A4.5) considers final stages of solidification where the composition of the remaining liquid can be assumed to be completely

mixed. The values for f_x and C_x as well as the constants a_1, a_2 and a_3 are determined as described by Giovanola & Kurz (1990).

In the previous models (A-C) the dendrite tip composition C_s obtained from the tip model (App. 2) was used as input data in the ID-models (designated to TIP-ID model). The use of models A and B included also comparative calculations which were carried out by calculating the composition of the first solid based on equilibrium partitioning (ID-model).

References

Clyne, T. W. & Kurz, W. 1981. Solute redistribution during solidification with rapid solid state diffusion. Metallurgical Transactions, Vol. 12A, pp. 965 - 971.

Giovanola, B. & Kurz, W. 1990. Modeling of microsegregation under rapid solidification conditions. Metallurgical Transactions, Vol. 21A, pp. 260 - 263.

Nishimoto, K. 1995. Private communication, April.

Ohnaka, I. 1986. Mathematical analysis of solute redistribution during solidification with diffusion in solid state. Transactions of ISIJ, Vol. 26, pp. 1045 - 1051.

APPENDIX 5

Calculation routine of the NSC-model

In the NSC-model (Koseki et al. 1994) a single cell with a hexagonal cross-section is assumed to grow into melt, c.f. Fig. A5.1. The heat conduction is assumed to be one-dimensional and parallel to the longitudinal direction of the cell. Solid state diffusion is assumed to be in the radial direction. The calculation regime shown is divided into FDM segments in such a way that the segment boundaries are perpendicular to the radial direction.

The flow chart of the model is shown in Fig. A5.2. Temperature decrease, ΔT, within a given time increment, Δt, is determined by the following equation, taking into consideration external heat extraction rate (q) and latent heat of solidification (ΔH_f):

$$q\Delta t = \rho c_\rho \Delta T + \rho \Delta H_f \Delta f_s \qquad \text{(A5.1)}$$

where ρ is density, c is specific heat and Δf_s is an increase in fraction of solid. Once a set of ΔT and Δf_s is obtained for a given Δt, the solute redistribution is determined with the advance of the solid-liquid interface. Then solid state diffusion of solutes is calculated using FDM. Finally, the stability of ferrite is checked in each FDM segment and transformation to austenite is calculated if necessary. This procedure is repeated until the temperature is decreased down to a fixed lower limit. Every stage of calculation is linked to Thermocalc™ so as to get every necessary thermodynamic information of multi-component alloys.

During calculation of the solid state diffusion of solutes, the distribution of nitrogen is determined according to Equation (A5.2):

$$\mu_1 = \mu_2 = \mu_3 = \ \ldots \ = \mu_N = \ \ldots \ = \mu_{NE} \qquad \text{(A5.2)}$$

where μ_N is the chemical potential of nitrogen in the N-th FDM segment ($1 \leq N \leq$ max. 20); nitrogen content of each FDM segment is determined by Thermocalc™ so as to satisfy the above assumption.

The basic variables used in the calculations were as follows:

- energy input 1580 J/s
- solidification rate 1 mm/s
- primary dendrite arm spacing 20 μm
- number of FDM cells 10

Reference

Koseki, T., Matsumiya, T., Yamada, W. & Ogawa, T. 1994. Numerical modelling of solidification and subsequent transformation of Fe-Cr-Ni alloys. Metallurgical and Materials Transactions, Vol. 25A, pp. 1309 - 1321.

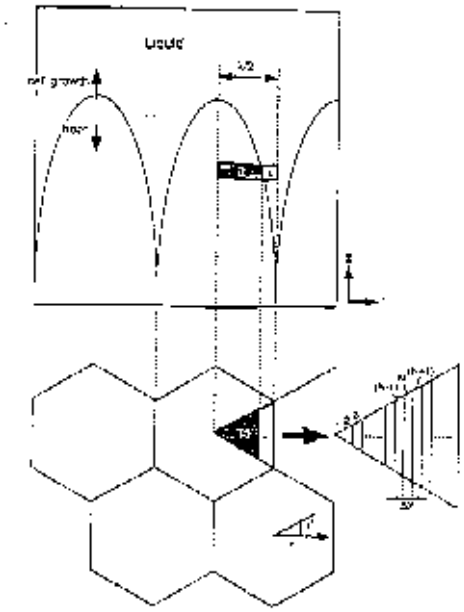

Fig. A5.1. Longitudinal and transverse section of a cell considered in the NSC-model, and calculation regime for FDM-analysis of solidification and solid state diffusion.

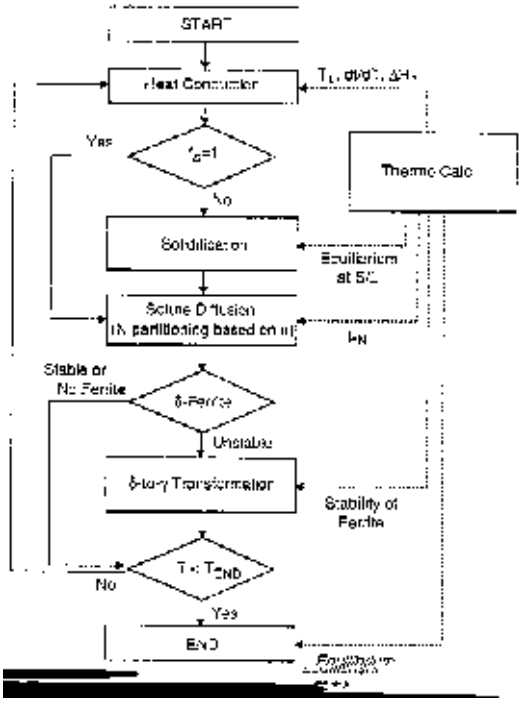

Figure A5.2. Flow chart of the model.

Calculation of weld cooling rates from heat conduction equations

The cooling rates at the weld centerline, caused by a point heat source can be calculated from the following equations (Rosenthal 1946, Radaj 1992):

- 2-dimensional cooling (thin plate solution)

$$\frac{dT}{dt} = 2\pi\lambda \frac{(T - T_0)^2}{Q} \qquad \text{(A6.1)}$$

- 3-dimensional cooling (thick plate solution)

$$\frac{dT}{dt} = 2\pi\lambda c\rho \frac{(T - T_0)^3}{(Q / d)^2} \qquad \text{(A6.2)}$$

where:

λ = thermal conductivity [W/mK]
ρ = density [kg/m^3]
c = specific heat [J/kgK]
T = temperature of interest [K]
T_0 = initial temperature [K]
Q = heat input = ηUI/v [J/m] where
η = thermal efficiency of the welding process
d = plate thickness [m]

In the present study the following values were used (ASM 1994):

λ = 14.6 W/mK
ρ = 7800 kg/m^3
c = 500 J/kgK

The thermal efficiency η was chosen to 0.75 (Smartt 1990).

For 3-dimensional cooling also the semiempirical formula of Svensson et al. (1986) was used:

$$\frac{dT}{dt} = \frac{C_1 (T - T_0)^{C_2}}{\eta Q} \qquad \text{(A6.3)}$$

In this equation C_1 = 1325 and C_2 = 1.6 and the other parameters as defined above.

References

ASM 1994. Speciality Handbook: Stainless Steels. Davis, J. R. (ed.) Ohio: ASM International. 577 p. ISBN 0-87170-503-6

Radaj, D. 1992. Heat Effects of Welding. New York: Springer-Verlag. 348 p. ISBN 3-540-54820-3

Rosenthal, D. 1946. The theory of moving sources of heat and its applications to metal treatments. Transactions of the ASME, Vol. 68, pp. 849 - 866.

Smartt, H. B. 1990. Arc welding processes. In: Olson, D. L., Dixon, R. & Liby, A. L. (eds.) Welding: Theory and Practice. Elsevier Science Publishers. Pp. 175 - 208.

Svensson, L.-E., Gretoft, B. & Bhadeshia, H. K. D. H. 1986. An analysis of cooling curves from the fusion zone of steel weld deposits. Scandinavian Journal of Metallurgy, Vol. 15, pp. 97 - 103.

Results of EPMA line scan analyses

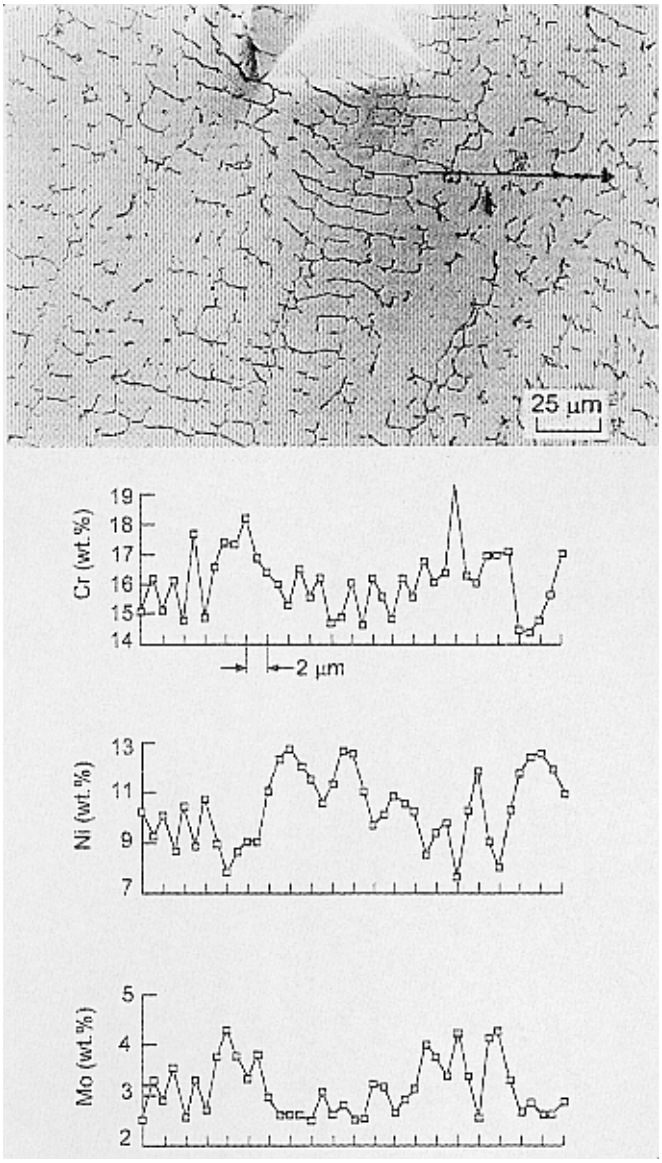

Fig. A7.1. EPMA line scan analyses for low-speed GTA-weld (100 mm/min) of steel 316/1. The measurements are taken from the weld centerline region.

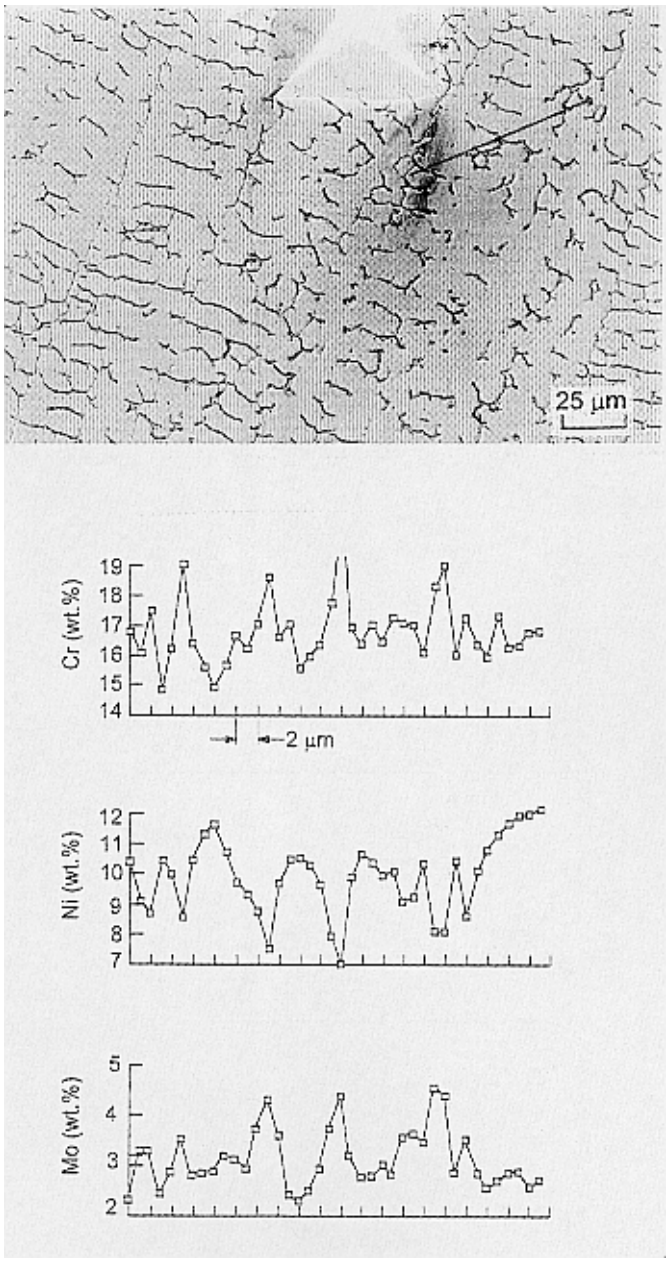

Fig. A7.2. EPMA line scan analyses for low-speed GTA-weld (100 mm/min) of steel 316/1. The measurements are taken from midway between weld centerline and fusion line.

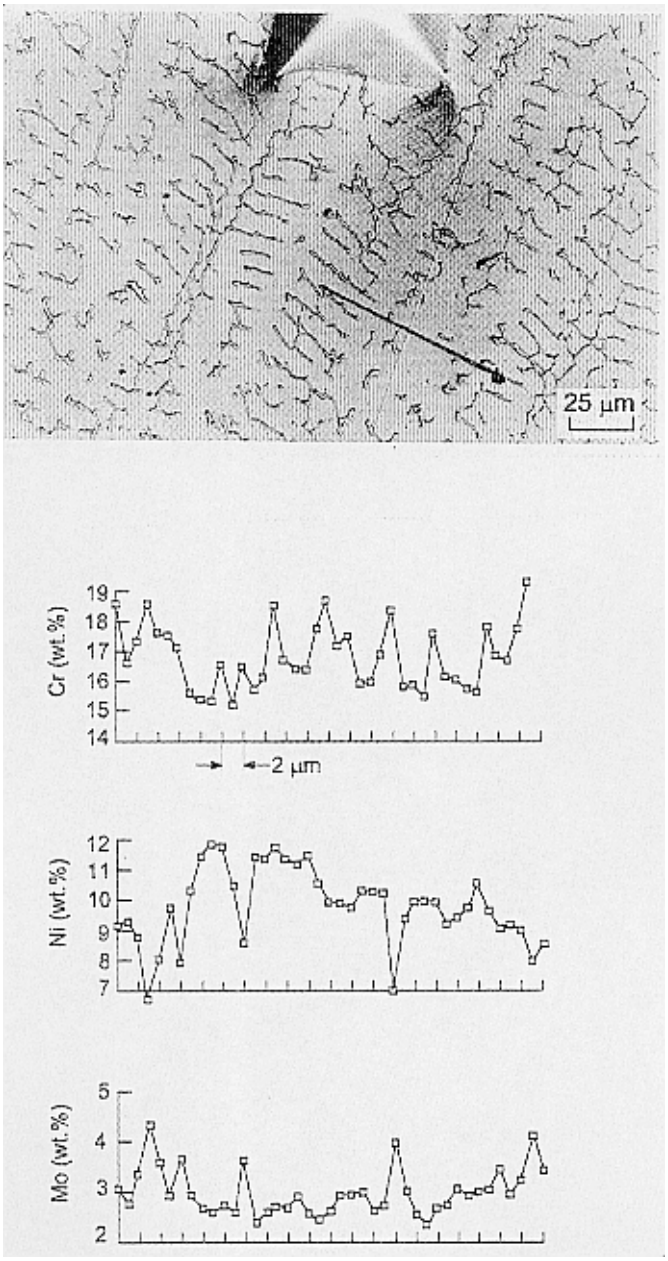

Fig. A7.3. EPMA line scan analyses for low-speed GTA-weld (100 mm/min) of steel 316/1. The measurements are taken from weld metal close to the weld fusion line.

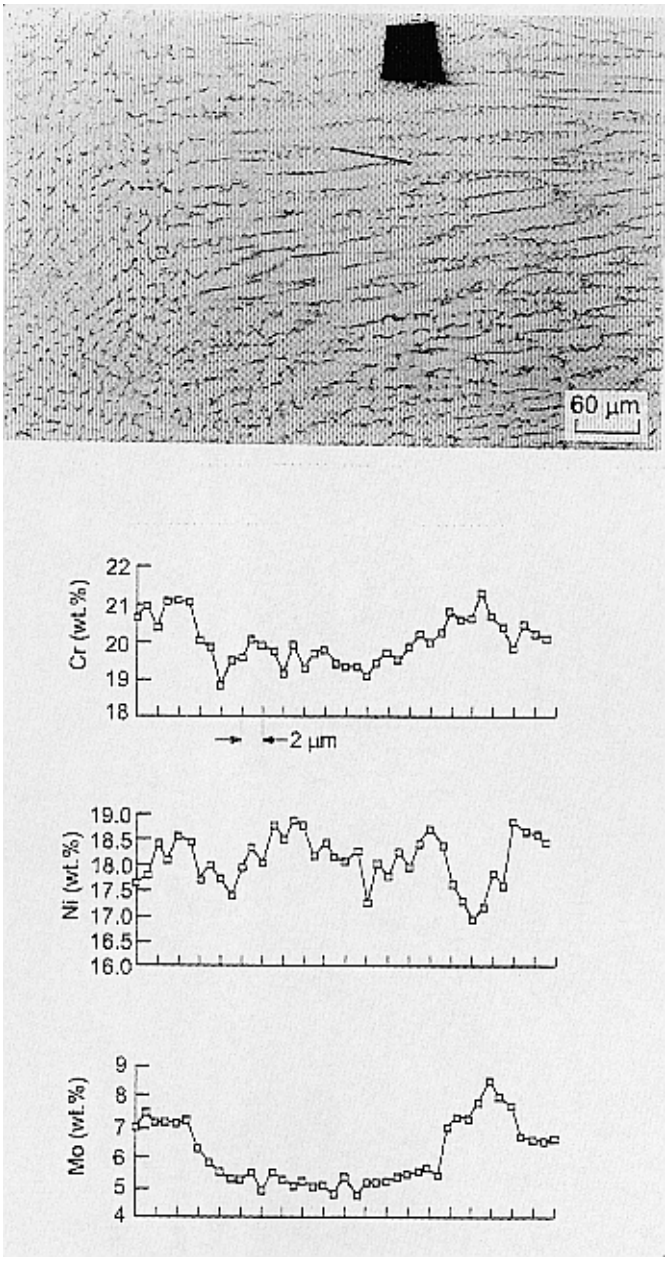

Fig. A7.4. EPMA line scan analyses for low-speed GTA-weld (100 mm/min) of steel 6Mo/1. The measurements are taken from the weld centerline region.

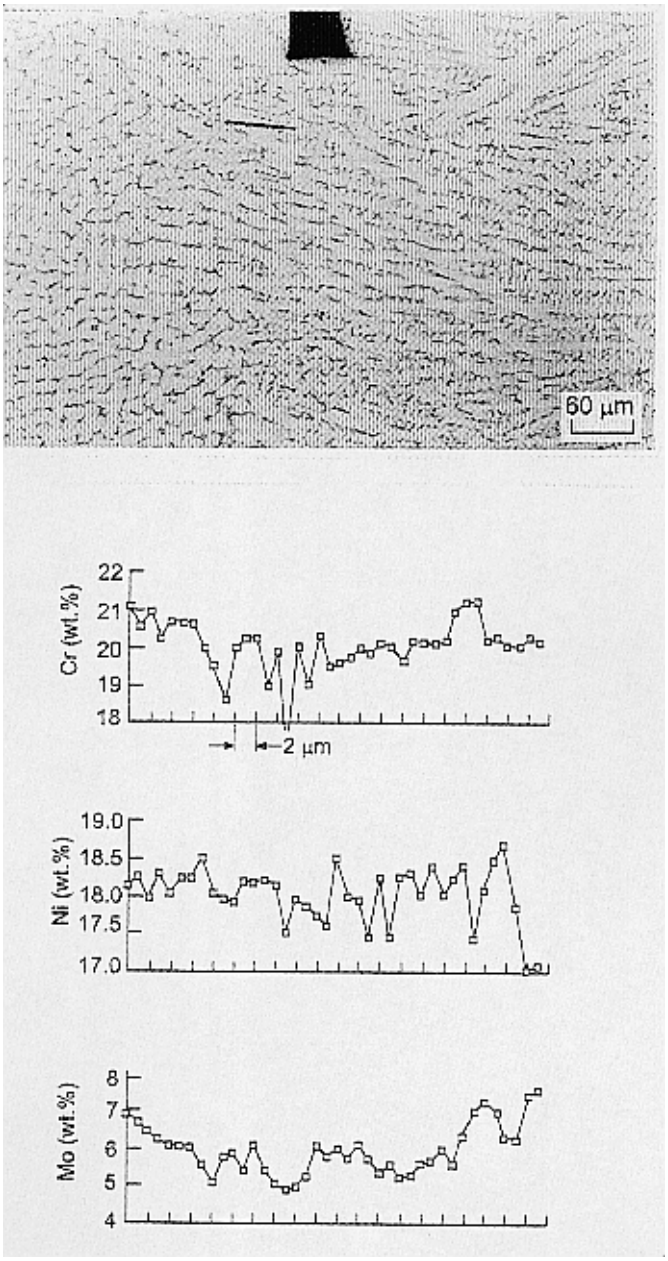

Fig. A7.5. EPMA line scan analyses for low-speed GTA-weld (100 mm/min) of steel 6Mo/1. The measurements are taken from midway between weld centerline and fusion line.

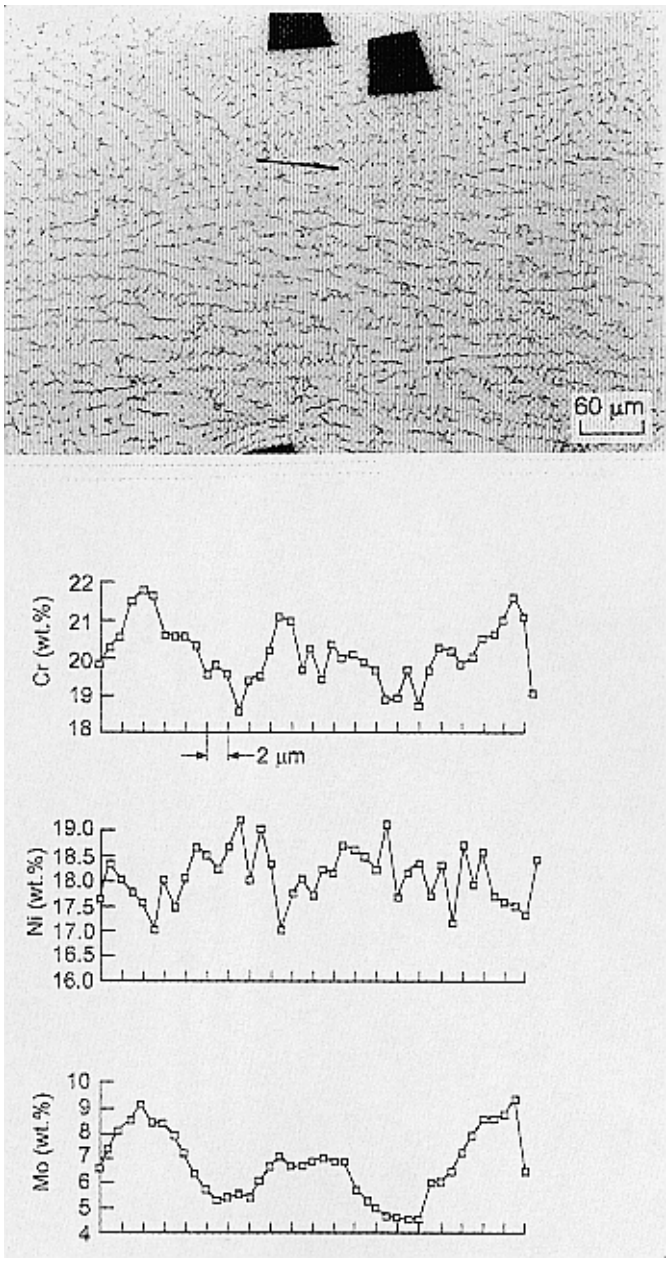

Fig. A7.6. EPMA line scan analyses for low-speed GTA-weld (100 mm/min) of steel 6Mo/1. The measurements are taken from weld metal close to weld fusion line.

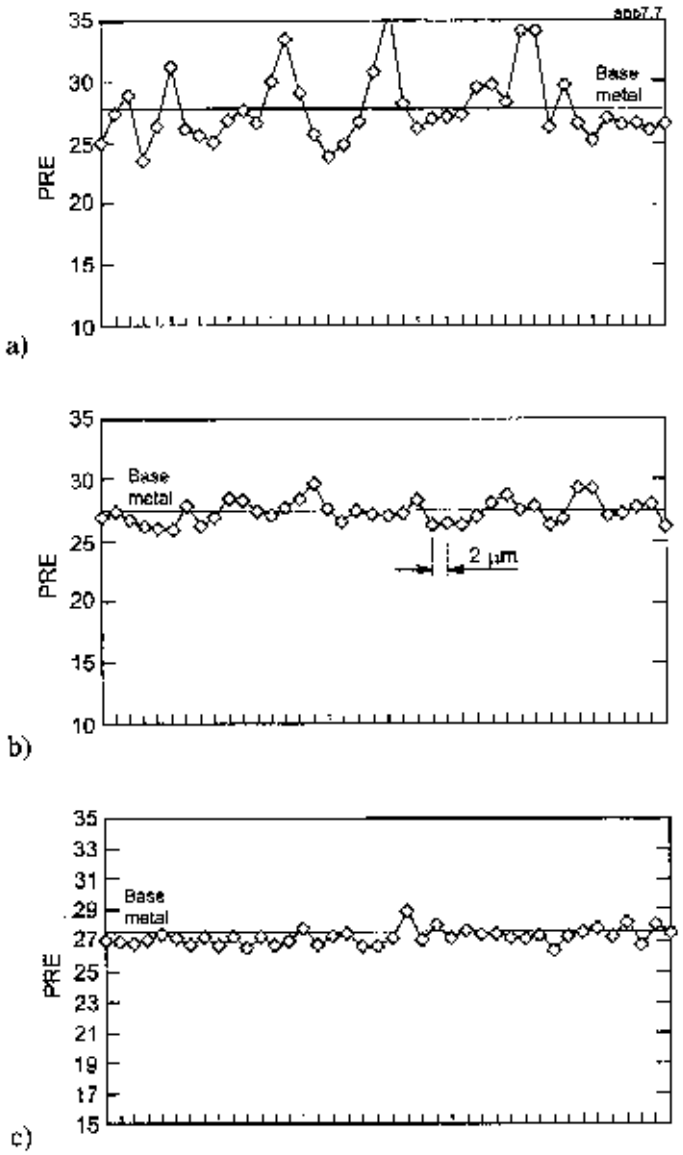

Fig. A7.7. PRE-patterns calculated from the EPMA line scan analyses for welds of 316/1 steel. Welding speed: 100 mm/min (a), 1000 mm/min (b) and 5000 mm/min (c). PRE = Cr + 3.3 Mo + 13N (nitrogen content is assumed to be constant).

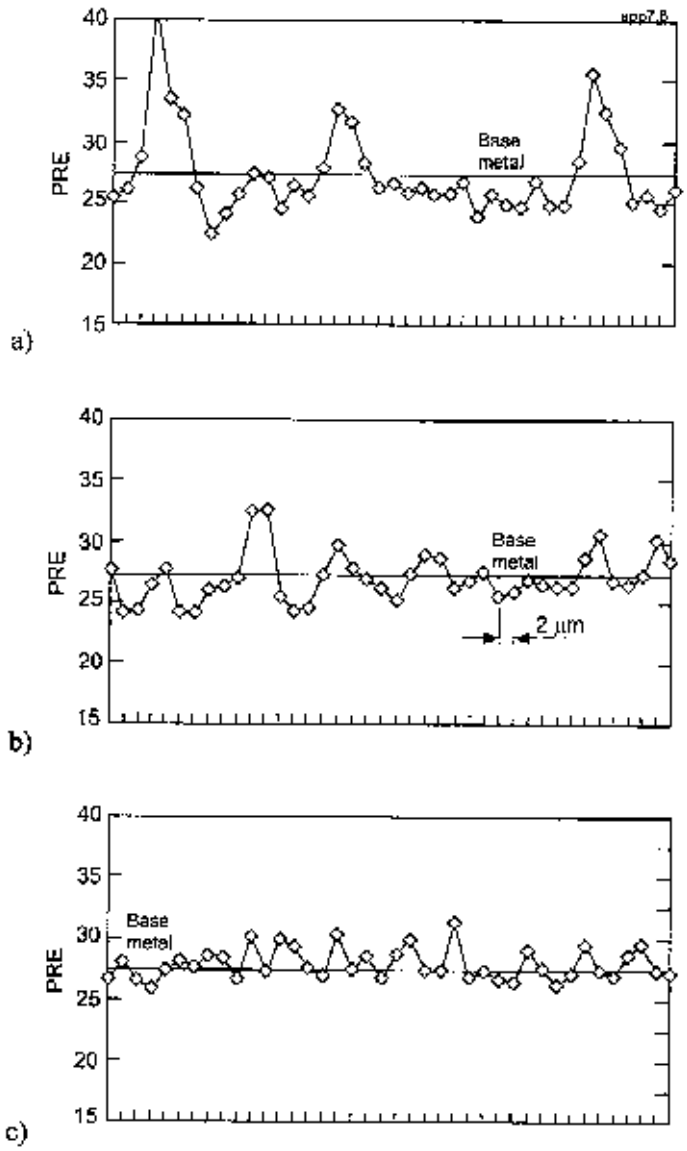

Fig. A7.8. PRE-patterns calculated from the EPMA line scan analyses for welds of 316/2 steel. Welding speed: 100 mm/min (a), 1000 mm/min (b) and 5000 mm/min (c). PRE = Cr + 3.3 Mo + 13N (nitrogen content is assumed to be constant).

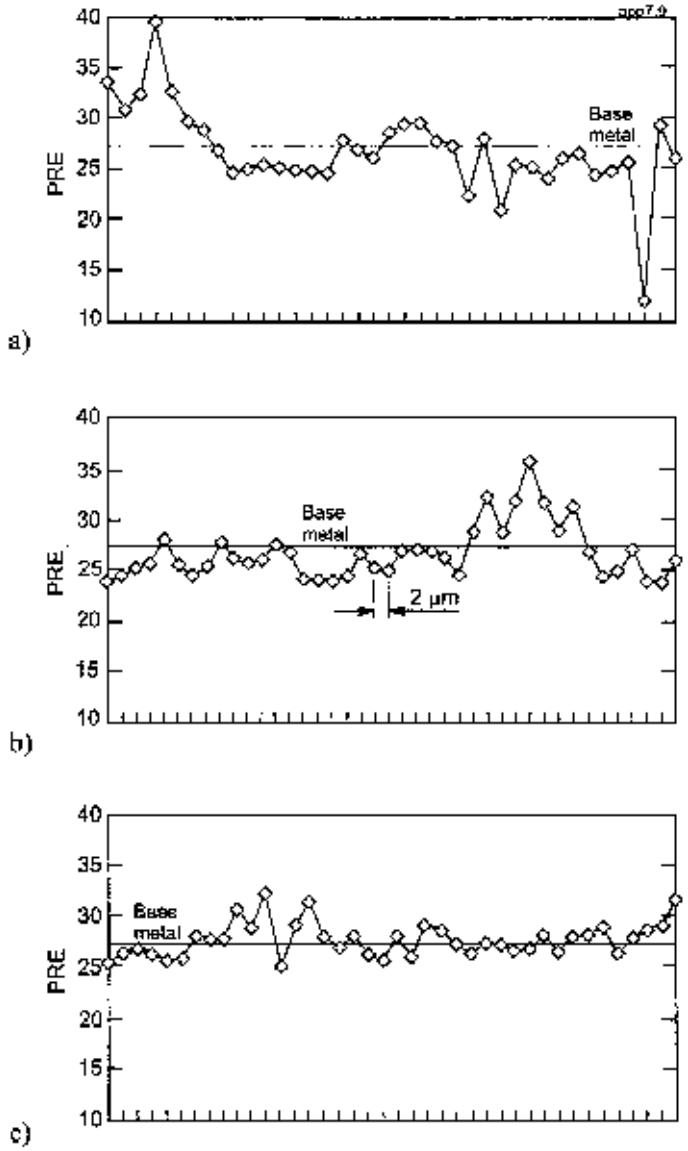

Fig. A7.9. PRE-patterns calculated from the EPMA line scan analyses for welds of 316/3 steel. Welding speed: 100 mm/min (a), 1000 mm/min (b) and 5000 mm/min (c). PRE = Cr + 3.3 Mo + 13N (nitrogen content is assumed to be constant).

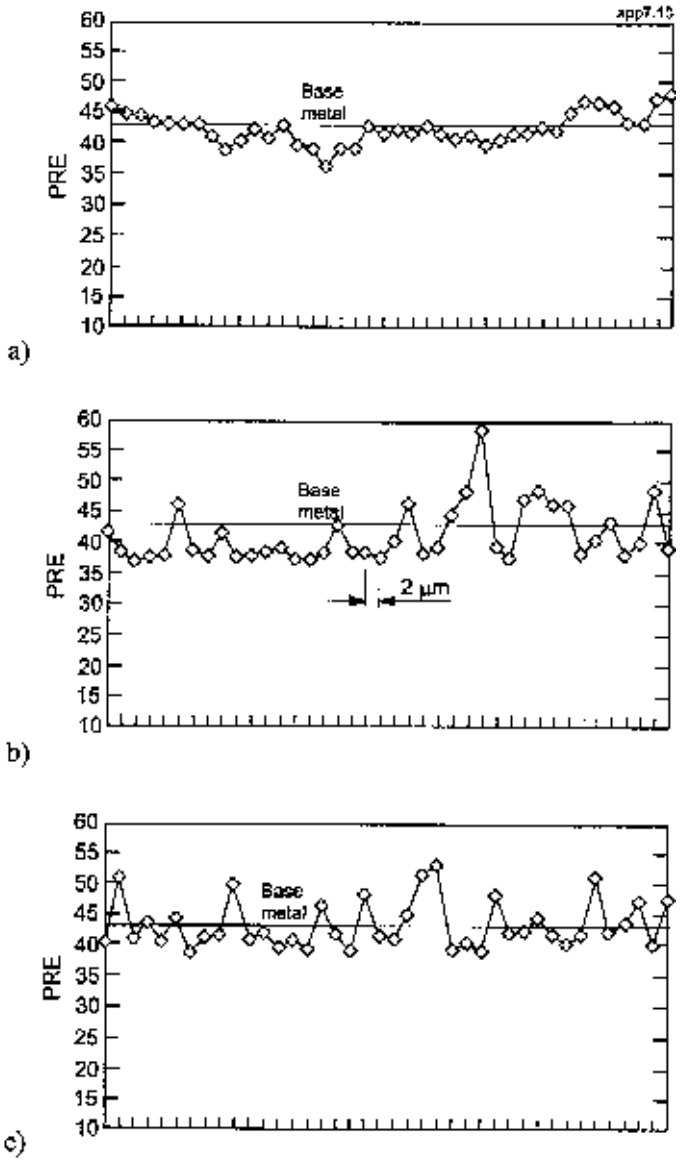

Fig. A7.10. PRE-patterns calculated from the EPMA line scan analyses for welds of 6Mo/1 steel. Welding speed: 100 mm/min (a), 1000 mm/min (b) and 5000 mm/min (c). PRE = Cr + 3.3 Mo + 13N (nitrogen content is assumed to be constant).

APPENDIX 8

Results of CMA-analyses

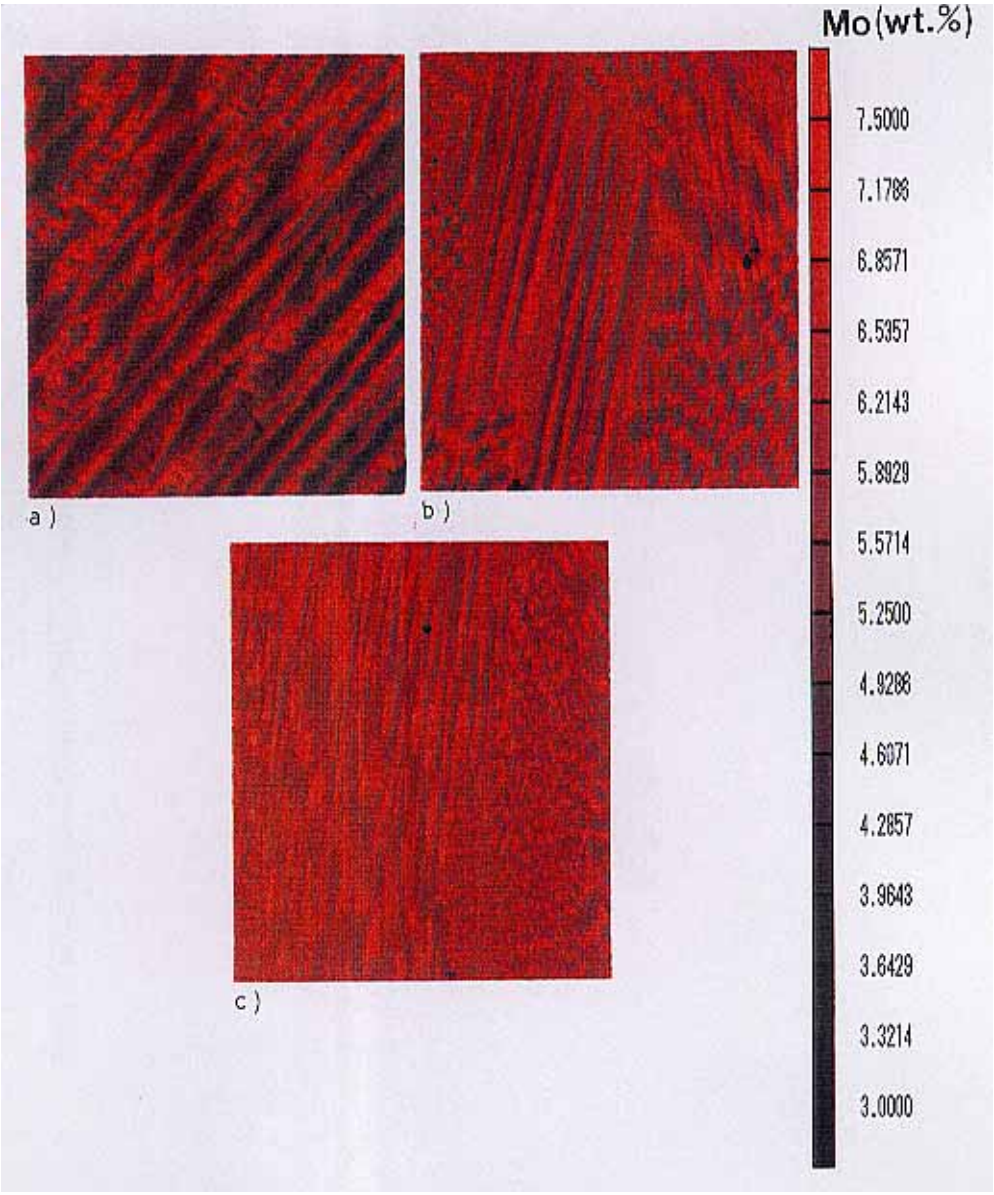

Fig. A8.1. Distribution of Mo measured by CMA-analysis for GTA-weld with 100 mm/min (a), and laser welds with 1500 mm/min (b) and 5000 mm/min (c).

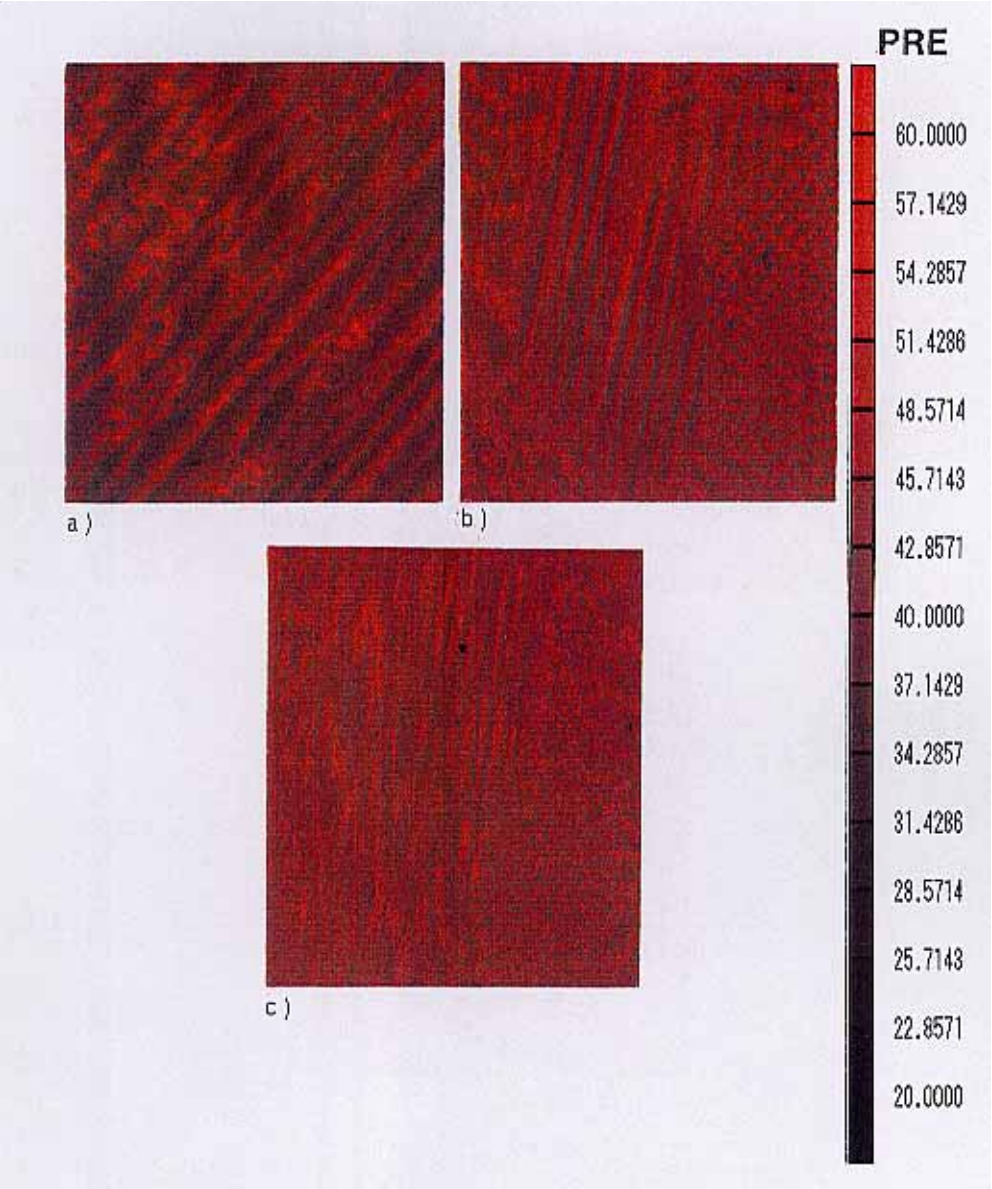

Fig. A8.2. Distribution of PRE calculated from the CMA-analysis for GTA-weld with 100 mm/min (a) as well as laser welds with 1500 mm/min (b) and 5000 mm/min (c).